The legacy of megafloods in the eastern Himalaya: from erosion to deposition

Susannah Marie Morey

A dissertation

submitted in partial fulfillment of the

requirements for the degree of

Doctor of Philosophy

University of Washington

2023

Reading Committee:

Katharine W. Huntington, Chair

Alison R. Duvall

David R. Montgomery

Program Authorized to Offer Degree:

Earth and Space Sciences

University of Washington

Abstract

The legacy of megafloods in the eastern Himalaya:
from erosion to deposition

Susannah Marie Morey

Chair of the Supervisory Committee:
Katharine W. Huntington
Earth and Space Science

Glacial lake outburst megafloods are infrequent, high magnitude (discharge $\geq 10^6$ m^3/s) events that are uniquely efficient agents of landscape change, despite being short lived. Much of our understanding of megaflood hydraulics and their subsequent erosion and deposition comes from the study of megafloods in low relief systems. However, recent research suggests that outburst floods will behave differently in steep, mountainous terrain than they would in relatively flat landscapes. The Yarlung-Siang River (YSR) in the eastern Himalaya provides an excellent case study to examine the impact of megaflooding in high-relief topography because of its history of megafloods throughout the Quaternary. In this dissertation, I investigate outstanding questions regarding the legacy of eastern Himalayan megafloods using interdisciplinary methodologies. Hydraulic simulations of an ancient megaflood sourced from the Tibetan Plateau show that megaflood erosional patterns will differ from those of the modern river due to dynamic interactions between flood hydraulics and the rugged mountain landscape which is far above the inundation of the modern or paleo YSR river channel, even in extreme meteoric flooding. If megafloods are a

significant contributor to erosion in this region, as many have suggested in prior studies, then simply using annual stream power estimates of erosion is insufficient to capture the impact of megaflooding. Beyond erosion, these simulations revealed an extensive potential for deposition of sediment, both fine-grained (sand and silt) and coarse-grained (decameter scale boulders). Additionally, hydraulic simulations predict that the Siyom River, a large tributary of the YSR, experienced up to 60 km of with megaflood backflooding. Remote topographic analysis and field geomorphology, sedimentology, and geochronology in fluvial terraces in the valley reveal evidence of extensive deep stagnant and turbulent water, which I interpret as megaflood backflooding deposits. Radiocarbon geochronology reveals megaflood deposit ages ~9-11 ka in the Siyom River valley, which coincide with the timing of a paleolake on the Tibetan Plateau thought to be a source of megaflooding down the YSR. The inundation of a tributary during a megaflood introduces complexities not typically considered in predictive models of river evolution in mountain landscapes. Finally, hydraulic simulations indicate potential for the deposition of ≥4m diameter boulders in boulder bars in the YSR channel during a megaflood, a finding that is consistent with field and remote sensing observations. Using a 1D landscape evolution model that incorporates the impact of immobile boulders on channel evolution, I determined that megaflood-deposited boulders create hundreds of meter-scale knickpoints which can persist for tens of thousands of years along the longitudinal profile of a river that experiences a megaflood. If that river experiences a sequence of megafloods, as is likely at the end of a glacial cycle, then those knickpoints will be refreshed and the change to the channel will compound, leading to a stepped longitudinal river profile—a potential signature of megaflooding in the landscape. Altogether, this dissertation advances understanding of how megafloods function in steep mountain landscapes and outlines the complex legacy of these immense floods, which includes both extensive erosion and deposition.

TABLE OF CONTENTS

LIST OF FIGURES

LIST OF TABLES

ACKNOWLEDGEMENTS

There are too many people to list who have meaningfully supported me throughout my time performing this research. My committee and advisor have worked closely with me to make sure this dissertation got finished, in spite of migraines, concussions, COVID, plumbing fiascos, sting ray attacks, and an injured cat. I'm excited to be your peer and continue to work with you on the ever-expanding research about eastern Himalayan megafloods. I would also like to thank my family and friends, but particularly my partner Mike for making me coffee every morning. I am excited that we will get to sit in rivers and cook dinner together for the rest of our lives.

DEDICATION

This work is dedicated to Zorro.

0. INTRODUCTION

The relative role of high-magnitude, low-frequency, geologically instantaneous or short-lived events in surface processes compared to that of typical fluvial processes has remained a long-standing question in geomorphology (Bretz, 1925; Baker & Kale, 1998; Garcia-Castellanos et al., 2009; Gupta; 2007; Wagner et al. 2013; Baynes et al., 2015; Stucky de Quay, 2019). In particular, outburst floods sourced from valley-blocking ice, glacial debris, or landslide dams can have peak discharge several orders of magnitude larger than that of meteoric floods—with the potential to rapidly shape downstream channel and valley morphologies both on Earth and Mars (e.g. Baynes et al., 2015; Carrivick & Rushmer, 2006; Cenderelli & Wohl, 2001; Cook et al., 2018; Lamb & Fonstad, 2010; Miller, 1995; O'Connor et al., 2013). The largest of these outburst floods, called megafloods (discharge $>10^6$ m^3/s) are thought to be responsible for carving canyons like the Channeled Scablands in Washington State (Baker, 2013; Baker and Kale, 1998) or on the Ceberus Plains on Mars (Burr et al., 2002; Lapotre et al., 2016). In fact, megaflood research is relevant to >40 landscapes on Earth and Mars (e.g., Baker, 2013; Carling, 2013; Baker, 2009; Burr et al., 2009; Rice and Edgett, 1997). In the eastern Himalaya, megafloods sourced potentially aid in rapidly exporting mass from the Himalayan orogen through the Ganges-Brahmaputra source-to-sink system (Lee et al., 2019). Yet a detailed understanding of the processes and geomorphic legacy of megafloods in steep mountain landscapes is lacking, leaving a gap in our understanding a key component of the source-to-sink system with potential implications for interpreting sedimentary archives.

There is ample evidence for glacial impoundments and subsequent megafloods throughout the Quaternary in the eastern Himalaya (**Figure 0.1**; H. P. Hu et al., 2018; S. Y. Huang et al., 2014; Kong et al., 2009; Korup et al., 2010; Korup & Montgomery, 2008; Song et al., 2013; H. Wang et al., 2021; Zhu et al., 2012). These megafloods have been proposed as agents of massive geomorphic change along the Yarlung-Siang River (YSR; Lang et al., 2013; Montgomery et al., 2004). For example, their dams and accompanying lake deposition are hypothesized to stabilize a knickpoint at the edge of the Tibetan Plateau (Korup and Montgomery, 2008), and erosion associated with megafloods has been invoked as a major contributor to the rapid incision of the Yarlung Tsangpo gorge (e.g., Lang et al., 2013; Turzewski et al., 2020)—one of the highest relief

landscapes in the world (e.g., Finnegan et al., 2008). However, a detailed analysis of megaflood erosion and deposition in the eastern Himalaya remains unexplored. Before we can assess the geomorphic change of an eastern Himalayan megaflood, we must first understand their hydraulics. Much of our understanding of megaflood hydraulics comes from the study of megafloods in low relief systems, like the Missoula Floods which traveled through the Channeled Scabland of Washington state (Carling et al., 2009; Denlinger and O'Connell, 2010; O'Connor et al., 2020; Lehnigk and Larsen, 2022). A recent study found that the hydraulics of a lower magnitude historic landslide lake outburst flood (LLOF) through the eastern Himalaya are strongly controlled by the high relief valley topography of the YSR (Turzewski et al. 2019). Because megafloods routed through the YSR have an order of magnitude higher discharge than historic outburst floods, their erosional and depositional patterns are hypothesized to differ from that of the modern river, modern outburst floods, and megafloods that flow through lower relief topography.

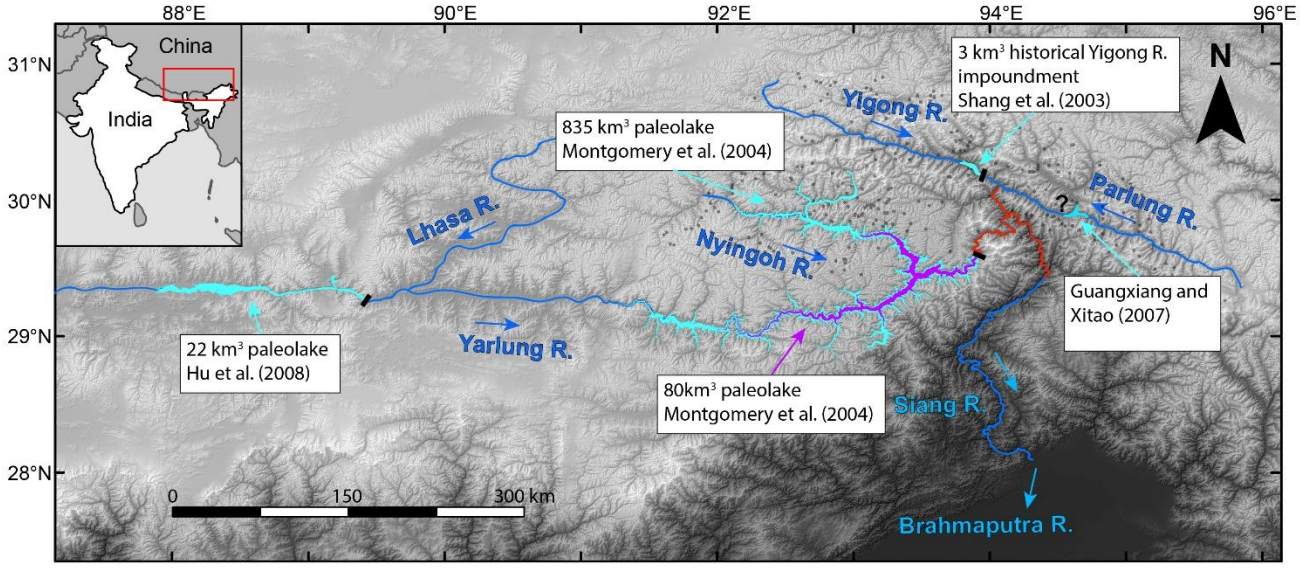

Figure 0.1. Regional map with major relevant rivers and paleolakes.

Locations of impoundments in the eastern Himalaya from Turzewski et al. (2020). The Yarlung River (blue) flows into the Yarlung Tsangpo Gorge (red). As the river enters India, it becomes the Siang River.

This dissertation addresses outstanding questions concerning eastern Himalayan megafloods and their geomorphic impact, with the ultimate goal of advancing understanding the processes and legacy of high-magnitude, geologically short-lived events in mountain river evolution. The first chapter presents a two-dimensional hydraulic simulation of a megaflood over three-dimensional topography in the eastern Himalaya. It addresses questions about the

relationship between the high relief landscape and flood hydraulics, the erosive potential of megafloods compared to modern stream power and the lower magnitude historical LLOF, and the depositional potential of megafloods in terms of sand and boulders. This work was published in April 2022 in the *Journal of Geophysical Research* (Morey et al., 2022). The second chapter explores the sedimentology, geochronology, and sedimentary provenance of potential megaflood backflow deposits in a tributary along the main flood pathway. This work will be submitted to the *Geological Society of America Bulletin* (Morey et al. *in prep*). The third chapter presents results from numerical modeling of bedrock river response to the deposition of ≥4m diameter megaflood-deposited boulders in large boulder bars. This study was submitted in June 2023 to *Geophysical Research Letters* and is currently under review (Morey et al., *in review*). Finally, the fourth chapter presents a summary of the conclusions of this work, highlighting the complexities of erosional and depositional patterns of megafloods in steep mountain landscapes.

1. **Chapter 1**: The erosional and depositional potential of Holocene Tibetan megafloods through the Yarlung Tsangpo Gorge, eastern Himalaya: insights from 2D hydraulic simulations

Published as: Morey, S. M., Huntington, K. W., Turzewski, M. D., Mangipudi, M., & Montgomery, D. R. (2022). *The erosional and depositional potential of Holocene Tibetan megafloods through the Yarlung Tsangpo Gorge, eastern Himalaya: Insights from 2D hydraulic simulations*. Journal of Geophysical Research: Earth Surface, 127, e2021JF006498. https://doi.org/10.1029/2021JF006498

Profound effects of episodic megafloods ($\geq 10^6$ m^3/s) have been observed on Earth and Mars. Quaternary megafloods sourced from valley-blocking glaciers on the Tibetan Plateau likely play an important role in the geomorphic evolution of the Yarlung-Tsangpo Gorge and mountain landscape of the eastern Himalaya. We use the first 2D numerical simulation of a megaflood sourced from a reconstructed 81 km^3 Tibetan lake to analyze flood hydraulics and examine the erosional and depositional potential of megafloods in mountain landscapes. The simulated flood has a duration >60 hours and a peak discharge of 3.1 x 10^6 m^3/s. We find that the extent of inundated features like terraces, narrow valley sections, tight meander bends, and overtopped ridges influence locations of observed maximum depth (370 m), speed (76 m/s), and bed shear stress (>10 kPa), creating dynamic patterns of erosive potential. Consequently, it is difficult to predict local (≤ 1 km) patterns of megaflood erosional potential from either unit stream power or flood power from smaller magnitude outburst floods. However, both are useful when predicting regional (≥25 km) order-of-magnitude shifts in megaflood flood power. Portions of the flood domain downstream of the Gorge experience lower bed shear stresses and flood power <5 kW/m^2, indicating potential for significant deposition. We suggest widespread deposition of boulders within the modern channel and fine-grained particles on hillslopes during a megaflood likely impedes subsequent erosion and affect channel width and longitudinal form throughout the flood. Our findings show the legacy of megaflooding in mountainous terrain includes both extensive erosion and deposition.

1.1 INTRODUCTION

Many outstanding questions in geomorphology concern the relative role that high-magnitude, low-frequency events play in shaping landscapes on Earth and other Solar System bodies (e.g., Baynes et al., 2015; Bretz, 1925; Carrivick et al., 2011; Gilbert, 1890; Scherler et al., 2017; Stucky de Quay et al., 2019; Wohl, 2010; Lapotre et al., 2016). On Earth, modern glacial lake outburst floods (GLOFs) and landslide lake outburst floods (LLOFs) (discharges up to ~10^5 m^3/s) are known to carve canyons (e.g., Lamb and Fonstad, 2010), mobilize large boulders (e.g., Cook et al., 2018; Huber et al., 2020), and initiate landslides on adjacent hillslopes (e.g., Cenderelli & Wohl, 2003; Larsen and Montgomery, 2012). Exceptionally large prehistoric megaflood GLOFs (discharge ≥10^6 m^3/s; referred to as "megafloods" hereafter) are believed to have caused such geomorphic changes, but on a much larger scale (Lamb et al., 2008; Lang et al., 2013; Larsen and Lamb, 2016; Cook et al., 2018; Huber et al., 2020; Benito and Thorndycraft, 2020; Lehnigk and Larsen, 2022). However, the specifics of megaflood hydraulics and how flood hydraulics scale between different magnitude outburst floods remain unclear, particularly in high-relief mountainous landscapes.

Megafloods sourced from glacial lakes on the Tibetan Plateau have been proposed as agents of massive geomorphic change along the Yarlung-Siang River (YSR) in the high-relief eastern Himalaya (Delaney & Evans, 2015; Hu et al., 2018; Huang et al., 2014; Korup et al., 2010; Korup & Montgomery, 2008; Lang et al., 2013; Montgomery et al., 2004; Song et al., 2013). Over 300 ancient and historic landslide and glacial dams have been identified in the region (**Figure 1.1**; e.g., Hu et al., 2018; Huang et al., 2014; Kaiser et al., 2010; Korup & Montgomery, 2008; Liu et al., 2015, 2018; Montgomery et al., 2004; Song et al., 2013; Zhu et al., 2012; G. Hu et al., 2020; H. Hu et al., 2018; Huang et al., 2014; W. Liu et al., 2015; Y. Liu et al., 2006; Xu et al., 2020; Zhu et al., 20z12). These observations along with depositional evidence of catastrophic downstream flooding from dam failure (e.g., Borgohain et al., 2020; Lang et al., 2013; Montgomery et al., 2004; Turzewski et al., 2019; Zhu et al., 2012) show outburst floods of different magnitudes have influenced this mountain landscape throughout the Quaternary, with effects extending beyond the Himalayan range through the Bengal Basin (Pickering et al., 2018) and >2000 km offshore in the Bay of Bengal (Lee et al., 2019). Recent work explored potential peak discharges and bed shear stress of prehistoric megafloods through mountain landscape of the YSR using one-dimensional

(1D) step-backwater hydraulic models that satisfy depositional constraints on paleoflood depth (Borgohain et al., 2020). However, two-dimensional (2D) hydraulic simulations of a historical LLOF in the region suggest valley topography influences outburst flood hydraulics in ways not captured by 1D models (Turzewski et al., 2019). It is unknown how megaflood flow conditions and resulting patterns of erosion and deposition vary dynamically as a function of inundated topography in this steep terrane.

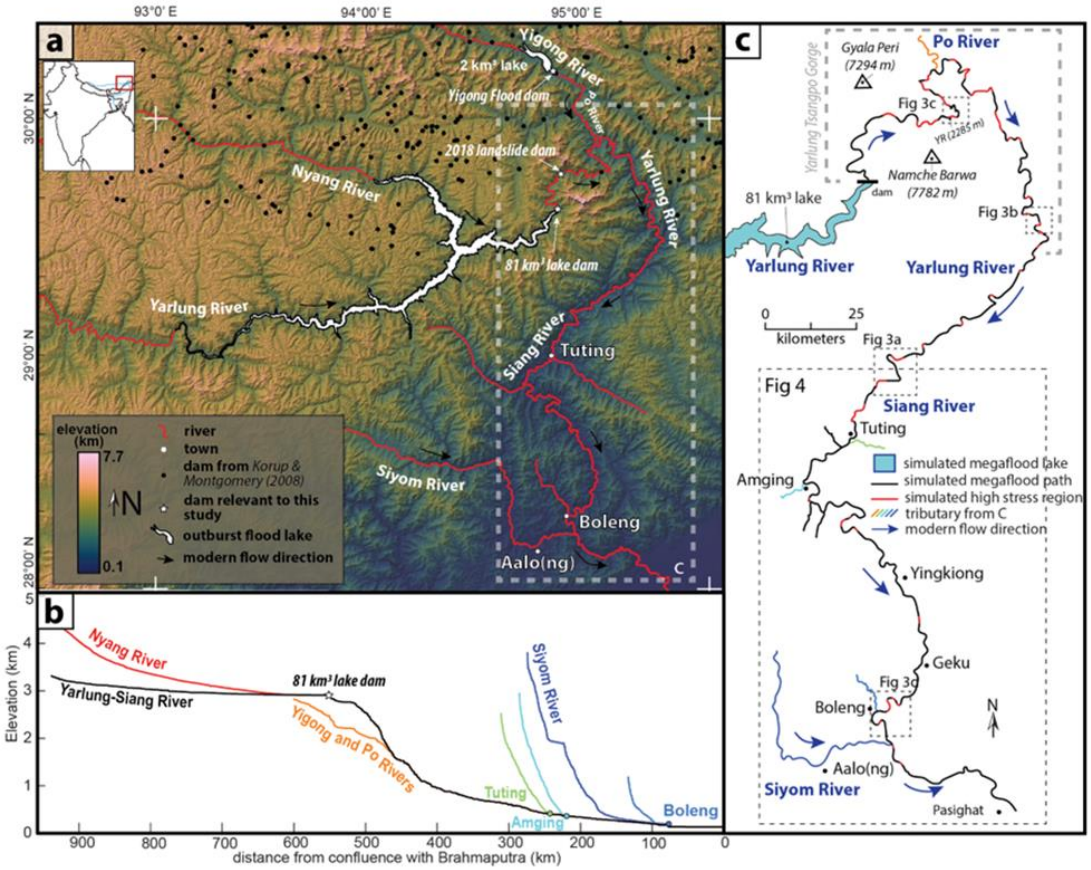

Figure 1.1. Regional map of the eastern Himalaya with major relevant rivers.

a) Lakes from the simulated megaflood and historical LLOF (2000 Yigong Flood, YF) are shown. The extent of the model domain is shown by the white crosses (30° N, 93° E; 28° N, 96° 36' E). **b)** Longitudinal profiles of rivers from **a**. **c)** Simulated extent of megaflood inundation along YSR river and tributaries that were inundated by > 5 km of backflow.

Here we present the first 2D simulation of a megaflood over 3D mountain topography of the YSR. The simulated flood results from instantaneous failure of an 81 km^3 lake impounded immediately upstream of the Yarlung-Tsangpo Gorge ("Gorge" hereafter; **Figure 1.1**). At this location, previous workers have documented repeated blockage of the Yarlung River by glacial advances between ~50 and 1 ka and reconstructed impounded lake volumes of 81-835 km^3 (Y. Liu

et al., 2006; Montgomery et al., 2004; Xu et al., 2020). We initiate the simulated megaflood using the youngest (lowest) reconstructed dam and lake level at this location, and focus analysis on general relations between flood hydraulics, landscape features, and sand and boulder deposits from multiple past flood events to build intuition for the behavior of outburst floods and megafloods in high-relief landscapes. The comparison is aided by analysis of simulation results for this megaflood and for a historical LLOF in the YSR drainage using empirical and theoretical relationships between flow hydraulics and sedimentary dynamics. We discuss implications for the legacy of outburst megafloods in mountain landscapes, particularly:

(1) the erosive potential of a megaflood compared to the modern river and that of a historical LLOF and any scaling relationships between the three magnitude flows, and
(2) the location and magnitude of megaflood deposition of both sand and boulders and any potential role this deposition might play on subsequent erosional processes.

1.2 BACKGROUND

The Yarlung River flows westward ~1,300 km through Tibet, parallel to the Himalayan orogen and Indus-Yarlung Suture Zone (IYSZ) before it abruptly turns south, dropping ~2 km elevation through the narrow 200-km-long Gorge (**Figure 1.1**). Named the Siang in India, this river contributes the majority of discharge observed in the Brahmaputra River, which ultimately drains into the Bay of Bengal. In Tibet, the river flows through predominantly Tethyan metasedimentary units within the IYSZ and Gangdese plutons comprised of both granodiorite and metasediments (Zeitler et al., 2014). In the Gorge, the YSR cuts through the Greater Himalayan sequence predominantly composed of gneiss before it returns to metasedimentary units near the confluence with the Po River (e.g., Booth et al., 2004). As the river enters India, it follows the axis of the Siang Window, an antiform comprised of Lesser Himalayan rocks that are predominantly metasedimentary, quartzite and Abor volcanic lithologies (Liebke et al., 2011; Singh et al., 2012). The Gorge region is among Earth's steepest and most rapidly eroding natural landscapes on both contemporary and million-year timescales (Burg et al., 1998; Booth et al., 2004; Finlayson et al., 2002; Finnegan et al., 2008; Larsen and Montgomery, 2012; Seward & Burg, 2008; Zeitler et al. 2014). Material eroded from the Gorge region dominates modern river sediment where the YSR exits the Himalayan rangefront (Enkelmann et al. 2011; Lang et al., 2013; Stewart et al. 2008) and appears in the deep-sea Bengal Fan (Blum et al., 2018; Copeland & Harrison, 1990; Corrigan &

Crowley, 1990; Najman et al., 2008). YSR erosion is aided by high annual discharge from Asian monsoon precipitation, which causes the Siang discharge to increase over 300% at Tuting Village (**Figure 1.1**, Central Water Commission Guwahati, 2019). In the last 70 years, the YSR has also experienced high discharge events from at least 10 LLOFs (Chen et al., 2020). Notably, one of the largest historical outburst floods, the Yigong Flood (YF; discharge 1.2 x 10^5 m^3/s), occurred in 2000 and left almost 100 dead in its wake, triggering landslides (Larsen and Montgomery, 2012) and depositing sand on hillslopes flanking the modern channel (Lang et al., 2013; Turzewski et al., 2019). Order-of-magnitude higher discharges from Quaternary megaflooding likely caused massive geomorphic change in the Himalaya (e.g., Montgomery et al. 2004; Lang et al., 2013) and Brahmaputra River valley (Pickering et al., 2018), and may have aided in erosion and transport of organic carbon from the YSR headwaters to the Fan, where its burial draws down CO_2 on geologic timescales (Galy et al., 2007; Lee et al., 2019).

Extensive depositional evidence of outburst flooding exists in the YSR drainage. This includes hundreds of mapped glacial and landslide-dam impoundments constraining potential flood sources in the YSR headwaters (**Figure 1.1**). Flood deposits in the Siang River valley include sand and boulders associated with historical LLOFs (e.g., Lang et al., 2013; Turzewski et al., 2019) and 51 megaflood slackwater sand deposits observed between 13 and 290 m above the modern channel (**Figure 1.2**; see Table A1 for details of published observations) (Borgohain et al., 2020; Lang et al., 2013; Panda et al., 2020; Srivastava et al., 2017; Srivastava & Misra, 2012; Turzewski et al., 2020). Slackwater sand deposit elevations document minimum paleoflood water levels (e.g., Borgohain et al., 2020), while provenance studies of the detrital zircons they contain constrain impounded lake sources (Turzewski et al., 2020) and megaflood erosion patterns (Lang et al., 2013; Turzewski et al., 2020). These previous provenance studies found that megaflood slackwater sands have a disproportionately high amount of Gorge-derived zircons compared to deposits from modern YSR and historical LLOF slackwater deposits. This result suggests that megafloods are a primary contributor to erosion of the Gorge region, supporting the hypothesis that both the magnitude—and spatial pattern—of erosion associated with extremely large GLOFs differ from those of smaller LLOFs and annual flows. However, past studies of megafloods in this region have relied on coarse estimates of megaflood discharge and bed shear stress from simplified channel geometries and 1D calculations of depth and velocity, or of pluckable or transportable block size, as a proxy for erosional potential (Montgomery et al., 2004; Lang et al., 2013; Borgohain et al.,

2020). A detailed study of megaflood hydraulics is needed to account for the potentially complex interactions between the megaflood waters and the topography of the YSR and more fully understand how different magnitude flows shape this rugged, mountainous landscape.

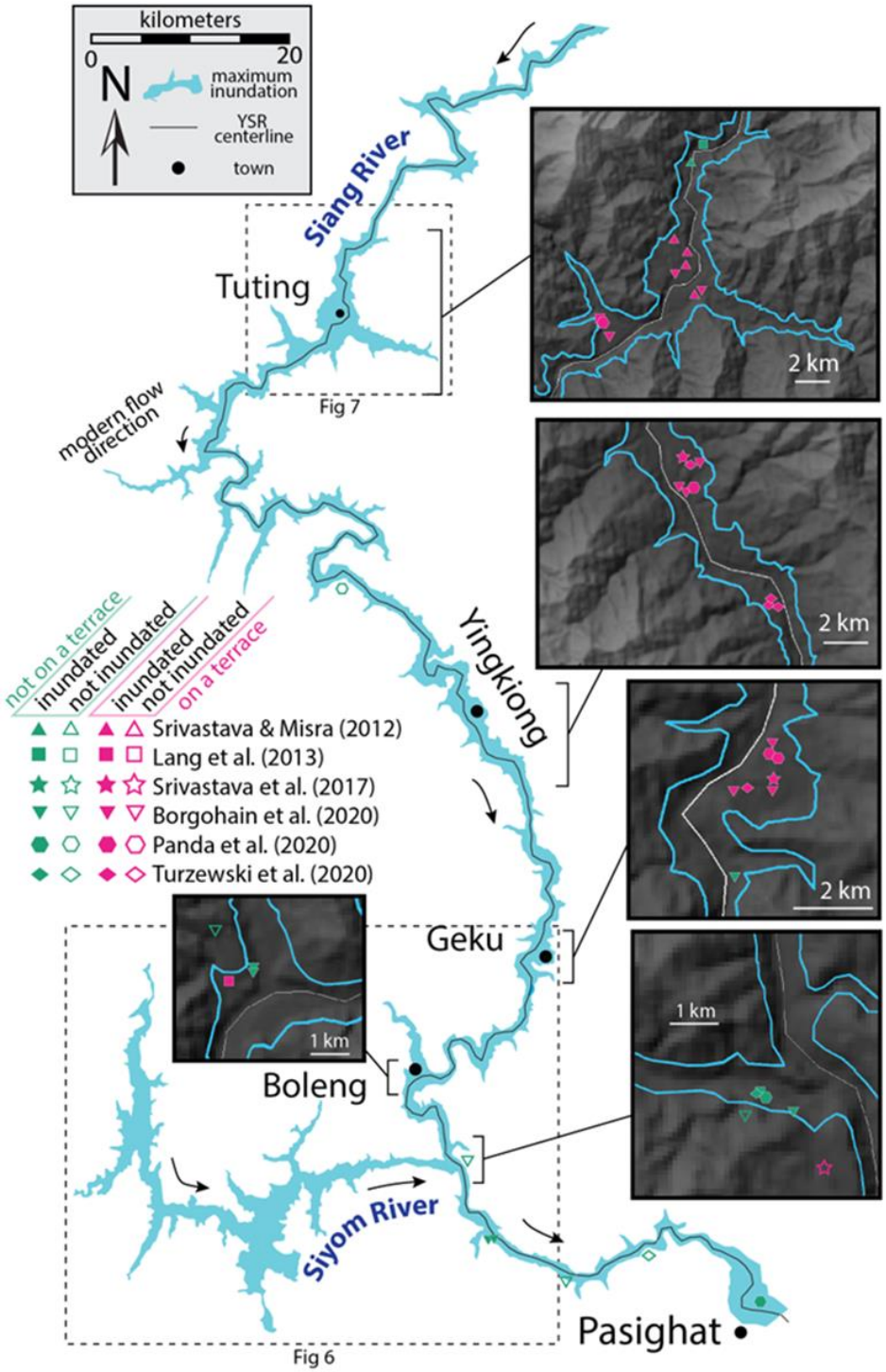

Figure 1.2. Maximum extent of inundation of Siang River during simulated megaflood.

All deposits previously identified as megaflood deposits are shown with their locations in reference to maximum megaflood inundation extent. A filled symbol represents an inundated deposit, while an unfilled symbol represents a deposit that was not inundated in the megaflood simulation. Deposits found on terraces are in pink, while deposits found elsewhere are in teal. Specifics about deposits can be found in Data Set S1 (https://doi.org/10.5281/zenodo.6301292).

Two-dimensional hydraulic modeling of the YF provides context for investigating megaflood hydraulics and their potential for erosion and deposition along the YSR. YF simulations by Turzewski et al. (2019) reveal that LLOFs routed through the YSR produce hydraulic patterns that differ from meteoric flooding. The predicted magnitude and spatial pattern of bed shear stresses from these simulations could explain YF slackwater sand deposition and the positions of some boulder bars with particle sizes that could not be moved by annual flows, for example, where inundation of valley topography (ridges) produces local zones of high bed shear stress predicted to pluck large blocks and shear stress gradients expected to cause block deposition downstream. The simulated YF interactions with landscape features and predicted erosional and depositional patterns along the YSR raise the question of how hydraulics, erosion, and deposition scale with flood magnitude from a LLOF to a megaflood.

1.3 METHODS

1.3.1 *Numerical modeling with GeoClaw*

We simulated the lake drainage and flood over 3D topography with 2D shallow-water equations implemented using GeoClaw (version 5.5) open source software (Berger et al., 2011; LeVeque et al., 2011). GeoClaw has been used to simulate drainage of Pleistocene glacial lakes (Bohorquez et al., 2016; Denlinger et al., 2021), as well as the YF through our study area (Turzewski et al., 2019). The maximum level of the 81 km^3 paleolake was determined from the presence of lacustrine and alluvial terraces at 3,088 m above sea level (Table A2; Montgomery et al., 2004). We use the prominent moraines on the flank of the Namche Barwa massif in the valley currently occupied by the Zelunglung Glacier as the location of our dam (**Figure 1.1**), which results in a dam 246 m tall and 1.3 km wide (Table A2). The computational domain encompasses the entire lake area, YSR, and adjacent hillslopes between the dam and the Siang-Brahmaputra River confluence (**Figure 1.1**). Additionally, we re-simulated the YF using parameters from Turzewski et al. (2019), sampling the model output at the same scale as our megaflood simulation to allow direct comparison of results.

Both outburst flood simulations use assumptions of clear water, a fixed bed, and instantaneous dam failure consistent with previous megaflood simulations (Bohorquez et al., 2016; Denlinger & O'Connell, 2010). Glacial moraine dams that cross valleys tend to fail mechanically via overtopping and incision, which leads to rapid (<1 hr) dam failure (Clague and Evans, 2000; Walder and Costa, 1996). For a long-lived flood lasting 10's of hours to days, a dam failure of <1 hour is relatively instantaneous. Turzewski et al. (2019) found that ignoring baseflow had a relatively small effect on inundation of high-water marks for a simulated YF. Thus, we assume that baseflow is negligible compared to the depths of megaflood inundation. Nevertheless, because of these assumptions, our results likely overestimate peak discharge and hydraulic parameters.

1.3.2 *Hydraulic calculations*

GeoClaw outputs include depth and momentum in two dimensions, which we use to calculate hydraulic parameters associated with erosion and deposition. We determined input parameters (Table A2) following the methodology of Turzewski et al. (2019). This includes choosing a mesh that refines up to 30 m for GeoClaw's adaptive mesh refinement (AMR) algorithm, to fit the resolution of our topographic data (combined SRTM 1 arc-second and 3-arc second DEM from Turzewski et al., 2019). Roughness (Manning's roughness parameter n) will likely vary spatially and temporally during a flood, but is set to a uniform value of 0.04 following previous LLOF and outburst megaflood studies (Carling et al., 2010; Turzewski et al., 2019). Bed shear stress τ_b is calculated:

$$\tau_b = \rho \left(\frac{gn^2}{h^{1/3}}\right) u^2 \qquad \text{(Equation 1.1)}$$

where ρ is the density of water, g is acceleration due to gravity, h is the flow depth, and u is the velocity of the flow (Larsen & Lamb, 2016). Peak bed shear stress is calculated every kilometer downstream of the dam location. To facilitate interpretation, we translate bed shear stress to movable grain size, D, using the critical Shields stress τ_{*c} :

$$D = \frac{\tau_b}{\tau_{*c}(\rho_s - \rho)g} \qquad \text{(Equation 1.2)}$$

where ρ_s is the density of sediment and the empirically derived relationship between critical shields stress and local channel slope measured at the reach scale, S_r, is (Lamb et al., 2008):

$$\tau_{*c} = 0.015{S_r}^{0.25} \qquad \text{(Equation 1.3)}$$

We calculate the unit stream power, ω_{sp}, at points along the YSR as:

$$\omega_{sp} = \rho g Q S_l / W \quad \text{(Equation 1.4)}$$

where Q is mean annual river discharge, S_l is the local channel gradient measured by averaging channel slope every kilometer downstream, and W is channel width. Mean annual river discharge was calculated after Finnegan et al. (2008) using TRMM (Tropical Rainfall Measuring Mission) data averaged between 2000 and 2007. We used the 3 arc-second WWF SRTM DEM and isolated cells with the highest discharge that formed a river profile. This is similar in method to that of Finnegan et al. (2008) but done at a higher resolution. Discharge was then calculated in kilometer intervals along the channel axis. Channel width was measured at each point where ω_{sp} was calculated using high-water marks from annual monsoon flooding observed in Google Earth imagery.

We calculate flood power per unit area, ω_{fp}, as:

$$\omega_{fp} = \tau_b u \quad \text{(Equation 1.5)}$$

(Denlinger & O'Connell, 2010). Throughout the study, "flood power" refers to this calculated flood power per unit area. Measurements of flood power were made from GeoClaw results of depth averaged velocity and calculated bed shear stress at a single cell within the flood domain and modern channel boundaries. Flood power values are plotted using a 5-minute moving average to account for the fact that peak values are often instantaneous and not representative of the sustained peak flood power experienced at a given inundated location.

1.4 RESULTS

1.4.1 *Overview of megaflood simulation results*

We simulated 63 hours of the megaflood, by which point the flood waters receded to flow depths and speeds similar in magnitude to the YF throughout the flood pathway with <1% of the original lake volume remaining. Simulated flood waters routed 507 km downstream of the breach along the YSR main stem to its confluence with the Brahmaputra, inundating hillslopes and tributaries along this pathway (the "flood pathway" hereafter). Peak discharge at the breach (3.1×10^6 m^3/s) was reached within an hour of dam failure (Figure A1), a value that is more than three times as large as the predicted discharge based on dam breach geometry and lake volume:

1.0 x10^6 m^3/s (Montgomery et al., 2004). Maximum inundation was 370 m in the Gorge. Simulation results, including videos of simulations, are available in Supplemental Information, which is linked in Appendix A.

1.4.2 *Inundation of megaflood slackwater deposits*

The simulated megaflood inundates the locations of most previously identified megaflood slackwater deposits, which record inundation levels from multiple prehistoric GLOFs of different magnitudes (**Figure 1.2**; Table A1; Data Set S1). 44 out of 51 (86%) of reported deposit locations are inundated, 34 of which are located on low-gradient terraces above the modern Siang River (Borgohain et al., 2020; Lang et al., 2013; Panda et al., 2020; Srivastava et al., 2017; Srivastava & Misra, 2012; Turzewski et al., 2020) (**Figure 1.2**). All megaflood deposits around the towns of Tuting, Yingkiong, and Geku are inundated at some point during the flood and most experience >20 hours of inundation. The 7 deposits that were not inundated are the highest deposits, located between 146 m and 406 m above the modern river (Table A1) and >350 km downstream of the dam, in the lowest gradient part of the flood domain (**Figure 1.3**).

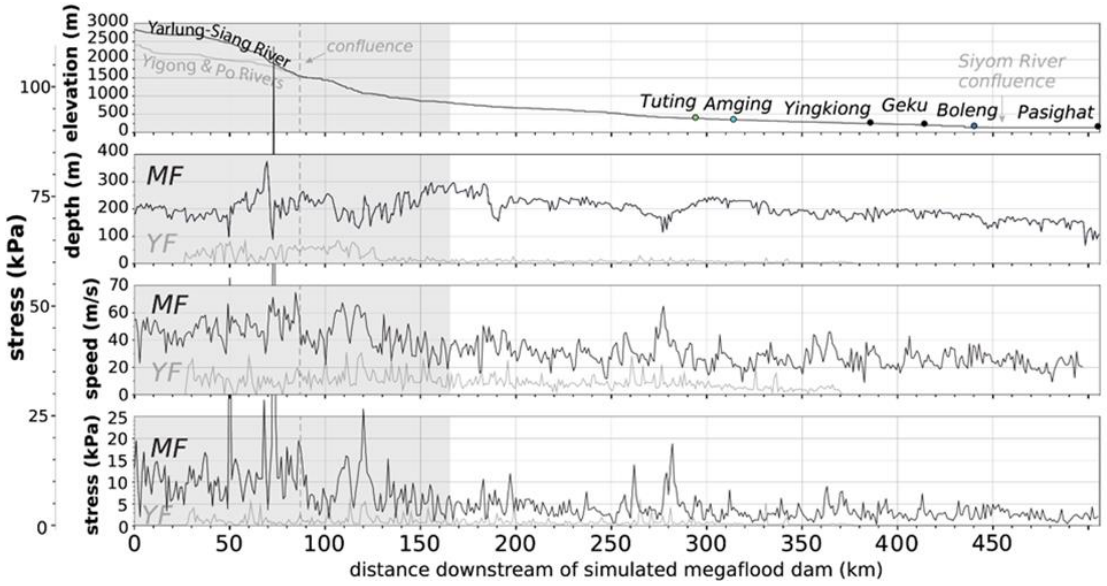

Figure 1.3. Model results from the simulated megaflood and 2000 Yigong Flood along the longitudinal profile of the YSR.

YSR channel elevation, and maximum simulated flood depth, speed, and bed shear stress along the flood pathway for the simulated megaflood (MF) and 2000 Yigong Flood (YF). Plotted vs. distance downstream of the simulated megaflood dam location to account for the slightly different paths the two floods take before entering the Gorge (i.e., Tuting is 289 km downstream of the MF dam and 254 km downstream of the YF dam). Measurements are taken

every minute and then averaged using a 5 minute moving average. Values are measured every 1 km downstream of the dam along the centerline of the modern YSR. The confluence of the Po River and YSR is the location at which the megaflood and YF pathways meet. Everywhere downstream of that location, measurements are taken from the exact same location. All three variables through time at every kilometer downstream of the simulated megaflood dam can be found in Data Set S2 (https://doi.org/10.5281/zenodo.6301292).

1.4.3 *Maximum flood depth, speed and bed shear stress*

Figure 1.3 shows simulated maximum depth, speed, and bed shear stress for the megaflood and YF simulations. Values are taken from the same geographic position along the centerline of the YSR channel to enable comparison despite the different inundation levels of the two floods, and the slightly different paths the two floods take before both course through the Gorge. The frontal wave velocity of the simulated megaflood is consistently at least twice as fast as that of the YF (Figure A2), reaching a maximum of 42 m/s during the first 13 minutes after the dam breach (compared to YF 21.0 m/s at t=16 minutes). Due to the velocity difference the simulated megaflood takes 4 hours to reach Tuting (X=289 km downstream of its dam) and ~9 hours to reach Pasighat, whereas the simulated YF takes 10 hours to reach Tuting (X=254 km downstream of its dam) and ~29 hours to reach Pasighat.

Maximum megaflood and YF depth, speed, and bed shear stress occur in the first 185 km of the flood pathway within the Gorge and generally decrease systematically downstream. On average, simulated megaflood flow is 20 m deeper, 18 m/s faster, and produces bed shear stresses 6.8 kPa and flood power 270 kW/m^2 greater in the Gorge than downstream of it, while the YF flow is 25 m deeper, 5 m/s faster, and produces bed shear stress 0.66 kPa and flood power 16 kW/m^2 greater in the Gorge than downstream of it (**Figure 1.3**). Exceptions to these patterns of maximum depth, speed and bed shear stress decreasing from the Gorge to downstream reaches do occur. A dip in megaflood maximum depth where the valley widens near Tuting (~x = 220-289 km downstream of the simulated megaflood dam) coincides with local highs in maximum megaflood bed shear stress that are similar to values observed in the Gorge (**Figure 1.3**). Several peaks in maximum YF depth, speed, and bed shear stress occur nearby on the downstream half of tight meanders (x = 265-331 km; **Figure 1.3**).

Maximum megaflood depth (370 m, at t=2.3 hrs after breach) occurs in the upper Gorge at a tight double meander x = 70 km downstream of the dam (**Figure 1.3**, **Figure 1.4**C). Here, water pools behind two high-relief ridges that obstruct flow as the floodwaters encounter them up to 370 m above the modern channel. Immediately downstream of this tight double meander, at x = 87 km,

maximum simulated speed (76 m/s, t=2.0 hrs) and bed shear stress ($1.1x10^5$ Pa, t=4.9 hrs) are observed, respectively. This feature is upstream of the Yarlung-Po River confluence and is not on the YF path; however, our simulation reproduces the result of Turzewski et al. (2019) showing similar valley features such as tight meanders and inundated ridges relevant to lower flood stage cause similar pooling of YF flood waters. Maximum depth in the YF is 84 m, at t = 3.5 hrs after breach, x = 107 m downstream of the simulated megaflood dam. Maximum megaflood bed shear stresses occur within an hour of the frontal flood wave arrival for 58% of the flood pathway and 90% experiences it within 6 hours (Figure A3).

1.4.4 *Topographic controls on megaflood hydraulic patterns*

Valley topography exerts direct control over hydraulic patterns of the simulated megaflood both in the Gorge and throughout the flood pathway. We observe locations where a valley-scale constriction changes the width of the flood path, causing water to deepen and slow upstream of the constriction (**Figure 1.4**). Such constrictions may occur anywhere the valley narrows significantly (**Figure 1.4**a), where the modern channel makes a sharp turn with a high-relief ridge protruding into the valley (**Figure 1.4**b), or where multiple tight valley meander bends occur (**Figure 1.4**c). Megaflood hydraulics can be non-locally controlled—i.e., some topographic features up- or downstream of a location might control the flow depth and speed at any given location, which will influence the patterns of bed shear stress and flood power that develop (**Figure 1.4**a, b, c, d).

While megaflood waters are always deepest within the modern channel, there are locations where the inundated topographic features cause water to pool, deepen, and slow unexpectedly. Often, water pools up to 1-5 km upstream of valley-scale constrictions. Immediately downstream (0.5-1 km) of valley-scale constrictions, simulated flow becomes shallower and faster as it reaches a critical state (Froude number = 1). Which topographic features exert primary control on megaflood flow depth and speed changes with time as different features are inundated as a function of evolving flood stage (**Figure 1.4** and associated movies).

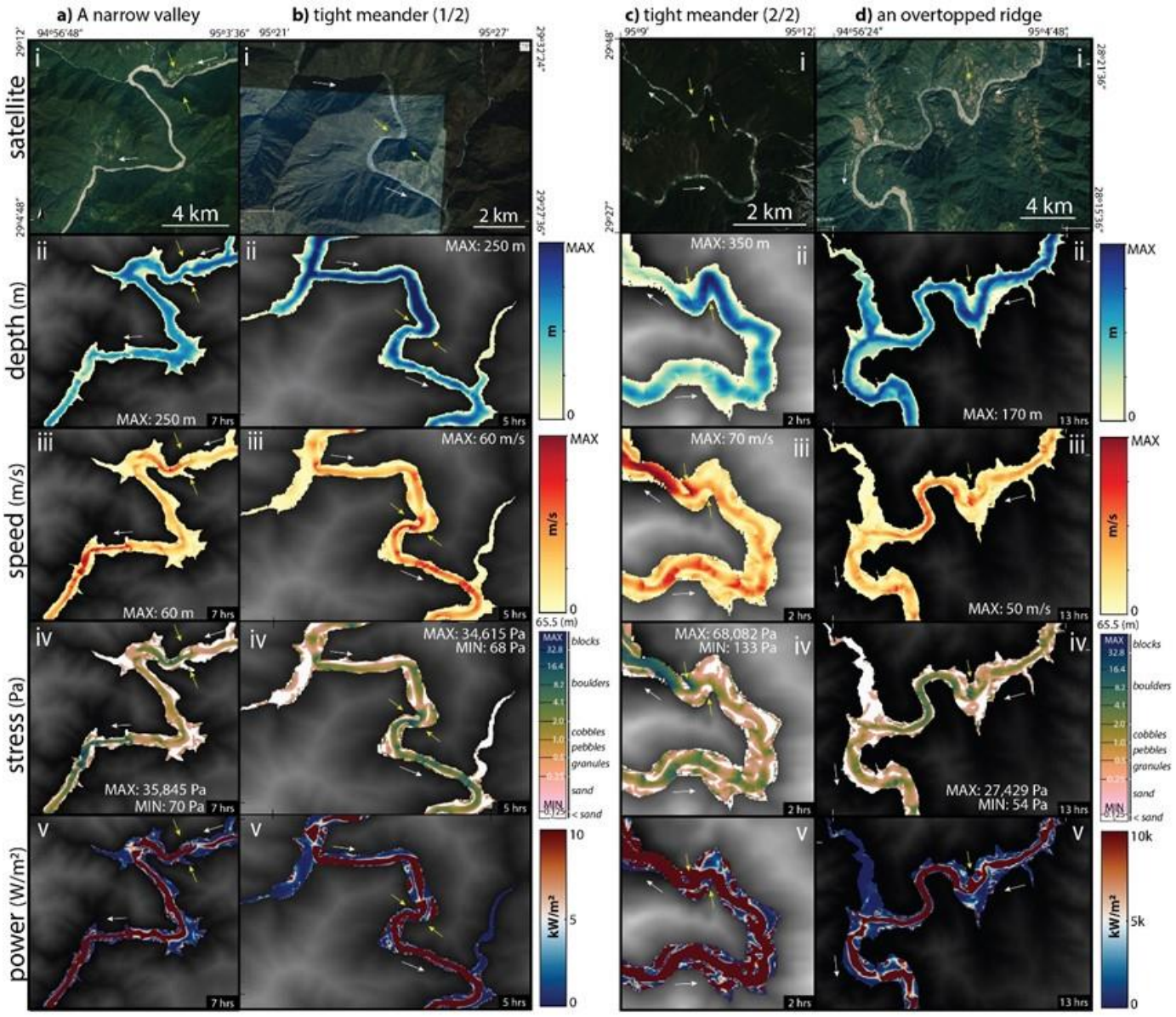

Figure 1.4. Different hydraulic patterns at a) a narrow valley, b) a tight meander, c) two tight, meanders, and d) an overtopped ridge.

Hydraulic variables shown are i) depth, ii) speed, iii) bed shear stress, and iv) flood power. Yellow arrows indicate the relevant topographic feature on the map and white arrows indicate flow direction. Maximum (and minimum, where relevant) values for variables are indicated for each location. All except bed shear stress have linear color bars; the color bar for bed shear stress (iii) is scaled to the stress required to move particles of a certain size on the local slope. Corresponding movies for depth, speed, bed shear stress, and flood power for: a = Movies S1, S2, S3, S4; b = Movies S5, S6, S7, S8; c = Movies S9, S10, S11, S12; d = S13, S14, S15, S16.

1.4.5 *Megaflood speed and bed shear stress*

The narrower the valley, the higher and more spatially uniform the maximum speeds tend to be. Maximum megaflood speed is almost always directly within the modern channel in the Gorge; however, zones of locally high flow speed often extend onto the adjacent, inundated hillslopes. Where the valley is narrow, high flood speeds can occupy the entire extent of inundation, extending well onto the hillslopes (**Figure 1.3**, Movies S1-16). This occurs in the Gorge channel and adjacent hillslopes, where the highest speeds during the simulated megaflood are observed (>20 m/s). In places where the valley is wide and low-relief terraces frequently flank the modern channel, the pathway of maximum speed often meanders and sweeps variably across the valley (**Figure 1.3**). This occurs in the domain downstream of the Gorge, where relatively high flow speeds are often found outside of the modern channel.

Patterns of high (>10 kPa) bed shear stress are variable in time and space during the simulated megaflood. There are 37 distinct, sustained (>5 hr) zones of high bed shear stress within the first 20 hr of the flood (**Figure 1.1**c), 23 of which occur immediately downstream of a valley constriction (**Figure 1.4**). The 14 zones of sustained high bed shear stress that are not related to valley constrictions do not necessarily occur within the main channel, and tend to be larger and longer-lived within the Gorge than downstream of it. In the Gorge, the zones of high bed shear stress tend to be on the downstream half of meanders, but not every meander experiences sustained high bed shear stress and some zones occur in relatively straight sections (**Figure 1.1**c). Downstream of the Gorge, these zones can be directly related to the morphology of inundated topography, like a high bed shear stress zone that develops as high relief topography is inundated around a 90° turn of the YSR (**Figure 1.4**biii) or one that develops immediately downstream of an overtopped ridge (**Figure 1.4**diii). As the extent of inundated topography changes, so do the patterns of bed shear stress (Movies S1-16).

1.4.6 *Megaflood and YF flood power and YSR unit stream power*

For most of the megaflood simulation, flood power is high (>10 kW/m^2) in the Gorge but tends to be <5 kW/m^2 downstream. In the Gorge, flood power exceeds 10 kW/m^2 everywhere until t = 15 hrs. From t = 15 hrs to t = 40 hrs, ~40% of the Gorge remains >10 kW/m^2 (Movie S17). Downstream of the Gorge, most of the flood pathway experiences high flood power during the 5

hr following the frontal flood wave's arrival (**Figure 1.4**a, d). After ~10 hr, the zones of high flood power become more isolated, with much of the flood pathway experiencing flood power <5 kW/m^2 (Movie S17). Later (t > 15 hrs), the downstream reaches have much more varied spatial patterns of flood power—which may change from time step to time step as different inundated features influence flow depth and speed (Movies S1-16).

These trends for megaflood flood power are compared to YF flood power and YSR unit stream power in **Figure 1.5**, calculated at the same points along the YSR channel axis. We plot the maximum flood power values for both the simulated megaflood and YF (see Figure A4 for 90th percentile values). As predicted by spatial patterns of YF depth and speed (**Figure 1.4**), the highest values of YF flood power are within the Gorge region with the exception of 4 places downstream of the Gorge (x = 265 km, 271 km, 281 km, and 331 km downstream of the simulated megaflood dam), all of which are in the same locations as high maximum stresses (**Figure 1.5**). Average YF flood power in the Gorge is 12 kW/m^2, while it is only 4.5 kW/m^2 on average downstream of the Gorge. Areas of high flood power (>10 kW/m^2) during the YF, while large with respect to the modern channel, are small compared to the areas of high flood power in the simulated megaflood and are not sustained for as long.

In the Gorge, average peak megaflood flood power (3.5 x 10^5 W/m^2) is >70 times greater than average unit stream power (4.8 x 10^3 W/m^2; **Figure 1.5**a), and average YF flood power (2.0 x 10^4 W/m^2) is ~4 times greater than average unit stream power. This difference between megaflood flood power and YSR unit stream power grows with distance from the dam (**Figure 1.5**c), while the difference between YF flood power and YSR unit stream power diminishes downstream (**Figure 1.5**c).

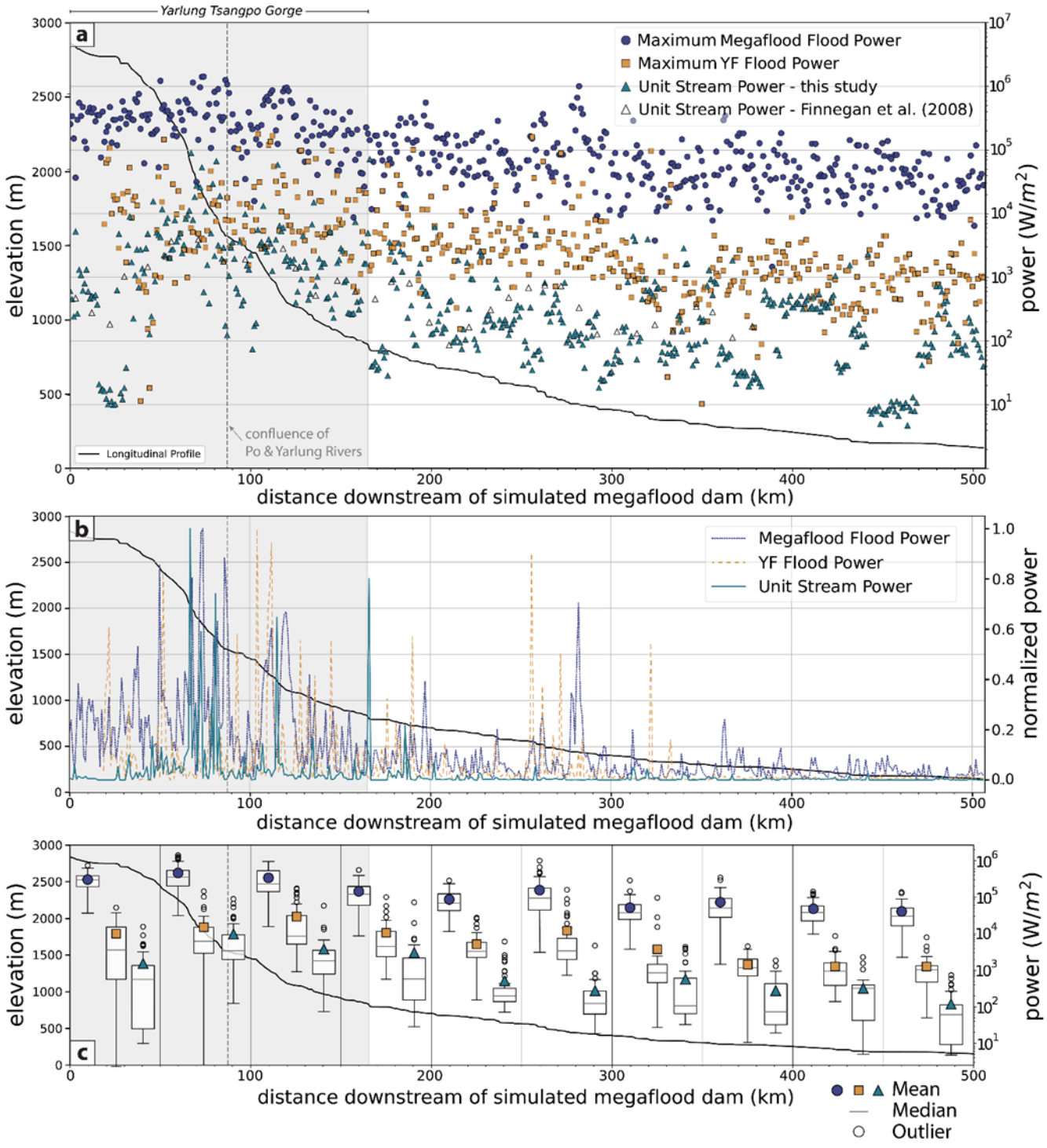

Figure 1.5. Unit stream power and maximum flood power per unit area (W/m^2) for the simulated megaflood and YF along the longitudinal profile of the YSR.

All plotted on a log scale vs. distance downstream of the simulated megaflood. The Gorge region is shaded. Blue circles and yellow squares are maximum values (over a 5-minute moving window) megaflood and YF flood power, respectively, calculated from GeoClaw outputs measured at a point along the YSR channel axis. The same plot (a,b)

with the 90th percentile values for GeoClaw outputs can be found in the Supplement as Figure A4. Teal triangles are unit stream power of the YSR at those same points in this study. Unfilled triangles are measurements of unit stream power averaged every 10 km from Finnegan et al. (2008). See **Error! Reference source not found.** for 10 km averaged megaflood and YF flood power values. **b)** The same maximum megaflood flood power and YF flood power, and unit stream power (from this study) from **(a)** but normalized to the maximum values of each dataset to compare spatial patterns more easily. **c)** Same data as in (b) binned in 50 km reaches along the flood pathway to show how these values shift with increasing distance from the dam. Box-and-whisker plots show means, medians, 25th and 75th percentile, and outliers for maximum megaflood flood power (blue circles) and YF flood power (yellow squares), and YSR unit stream power (teal triangles).

1.4.7 *Backflow inundation*

Most major tributaries experience 8-13 km of backflow during the flood (**Figure 1.1**; Table A3), but the Siyom River (the Siang's largest tributary) experiences up to 60 km of backflow up to 100 m deep (**Figure 1.6**; Movie S18). Tributaries of the Siyom are inundated up to 9 km, and water begins to recede at t = 23 hr. Speeds reach up to 30 m/s before t = 15 hr, although most regions experience maximum speeds of only 5 m/s. Bed shear stresses along the Siyom are lower than along the main flood pathway; nevertheless, they reach up to ~3.8 kPa between t = 9 and t = 16 hs (**Figure 1.6**). As the Siyom is initially inundated, zones of higher bed shear stress form km-scale eddy-like patterns. Flood power is ≥10 kW/m^2 within the frontal wave of inundation. Subsequently, flood power decreases to ≤5 kW/m^2 for the remainder of the flood, except where the Siyom valley is narrow and flood power in a few locations of the channel increases to ≥10 kW/m^2 (Movie S21).

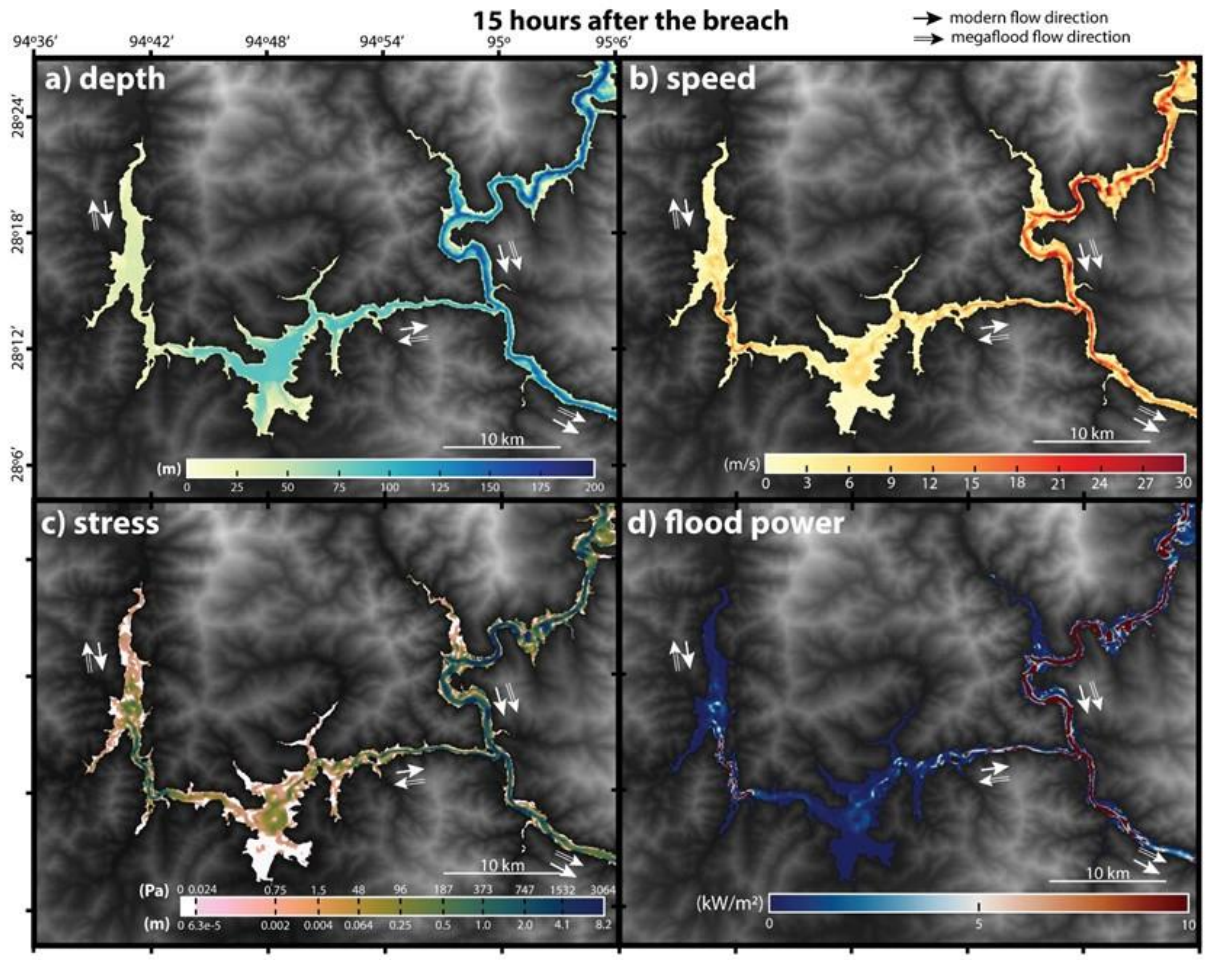

Figure 1.6. Simulated a) depth, b) speed, c) bed shear stress, and d) megaflood flood power along the backflow inundated Siyom River 15 hrs after the breach.

Corresponding movies for: a = Movie S18; b = Movie S19; c = Movie S20; d = Movie S21.

1.5 DISCUSSION

This study represents the first 2D numerical simulation of megaflood hydraulics over 3D topography along the YSR, which we use to build intuition for erosional and depositional patterns of a megaflood through steep topography of the eastern Himalaya. We find that megafloods not only produce far higher flood power than smaller magnitude floods, they also produce different local, kilometer scale patterns of flood power and, therefore, erosional and depositional potential. Large-scale valley constrictions and features like meander bend ridges and terraces that are inundated in a megaflood but not in smaller flows will directly influence megaflood hydraulics and the resulting patterns of bed shear stress and flood power. Patterns of high bed shear stress and

flood power in a megaflood, and the erosional potential they imply, do not scale in a straightforward way with patterns of unit stream power, but do have regional relationships with flood power from smaller magnitude floods. This suggests a potentially important role of large outburst floods in spatial patterns of erosion in mountain landscapes. Furthermore, megaflood inundation and bed shear stresses are capable of depositing sand to boulder-sized sediment in topographic settings where slackwater sand deposits and boulder bars interpreted to have been deposited by megafloods are observed along the Siang valley. We propose megaflood deposition of such sediment impacts river incision and hillslope processes, suggesting a long term (>10^3 yr) legacy of megaflood deposition for mountain landscape morphology.

1.5.1 *Patterns of megaflood inundation*

Modeling of lower magnitude LLOFs along the YSR indicates that inundated features are important for controlling flood hydraulics relevant for erosion and deposition, but prior megaflood simulation in this region has been limited to 1D models (Borgohain et al., 2020), which may not capture the complexities of the interactions between megaflood hydraulics and the high relief YSR valley. Our 2D hydraulic simulation over 3D topography does produce a peak discharge (3.1 x 10^6 m^3/s) at the breach that is three times as large as (a) discharge predicted based on dam breach geometry and lake volume (1 x 10^6 m^3/s: Montgomery et al., 2004 predicted using Cenderelli, 2000; 1.1 x 10^6 m^3/s: O'Connor & Beebee, 2009) and (b) minimum discharges used in 1D models of megafloods in this landscape (1.3 x 10^6 m^3/s: Borgohain et al., 2020). The simulated megaflood inundates the YSR valley to elevations >100 m above the channel over nearly the entire flood pathway (**Figure 1.2**, **Figure 1.3**b, and **Figure 1.4**), flooding hillslopes >1-2 km away from the channel axis in many locations (**Figure 1.2**, **Figure 1.4**, and **Figure 1.6**). Inundation and backflow extend far up tributary valleys, reaching up to >60 km up the Siang River's largest tributary the Siyom (**Figure 1.6**). Extensive megaflood inundation of YSR hillslopes persists for up to 40 hr after initial inundation (**Figure 1.7** and associated movies), while the most extreme inundation of the Siyom River valley lasts for ~50 hr (**Figure 1.6** and associated movies). Even without explicit consideration of flow speed and bed shear stress, such extreme inundation of channels and hillslopes is expected to significantly impact hillslope and river processes.

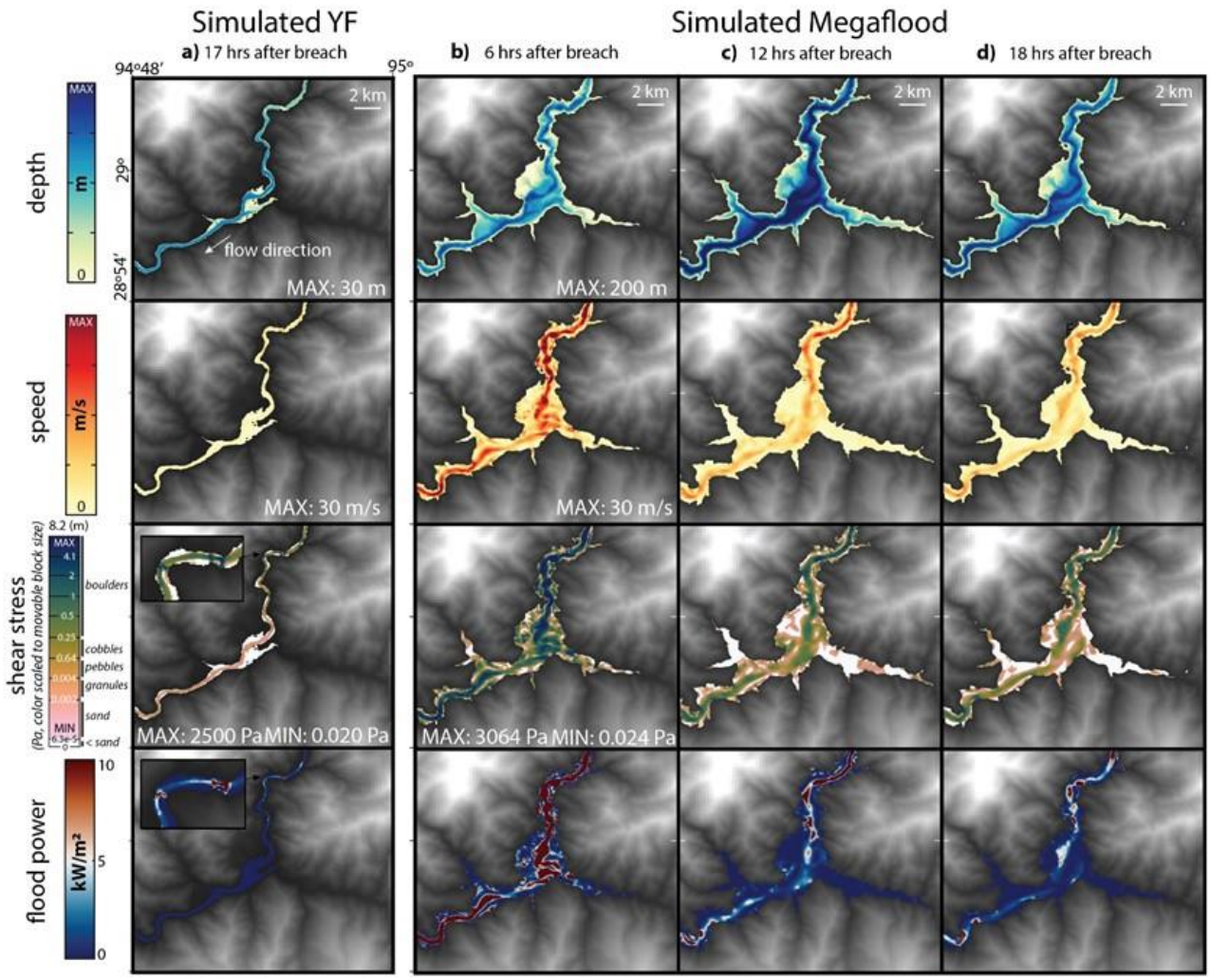

Figure 1.7. Snapshots of flow depth, speed, bed shear stress, and flood power around Tuting for the simulated YF and megaflood.

(a) the Yigong Flood at t=17 hr and (b,c,d) the megaflood at t=6, 12, and 18 hrs into the simulation. Flow direction is marked in the first panel. Note that color bars have different maximum values for each flood. The color bar for bed shear stress is coded to movable block size given the local channel gradient (see Methods), with a maximum of 8.1 m. Corresponding movies for the simulated megaflood: depth = Movie S22; speed = Movie S23; stress = Movie S24; flood power = Movie S25.

Indeed, effects should be particularly significant on hillslopes, which make up 86% of the maximum extent of megaflood inundated topography (**Figure 1.2**, **Figure 1.4**, and **Figure 1.6**). While previous workers have mostly focused on the bedrock channel erosion that occurs during a megaflood in the eastern Himalaya (Finnegan et al., 2008; Lang et al., 2013), our results indicate that the hillslopes along the flood pathway not only have important features that will exert a control on patterns of megaflood hydraulics (**Figure 1.4**, **Figure 1.6**, and **Figure 1.7**), they are also likely

a much larger source of sediment than the bedrock channel during a megaflood. As many of the hillslope features important for megaflood hydraulics are not inundated during lower magnitude floods, local (i.e., <1 km reach) patterns of bed shear stress and flood power during a megaflood will not mimic those of the smaller magnitude flood. The YF is known to have triggered landslides throughout the flood pathway, particularly within the Gorge region (e.g., Delaney and Evans, 2015), where hillslopes are near threshold angles (Larsen and Montgomery, 2012). Megaflood inundation remains elevated throughout the mountainous flood pathway; in contrast, YF maximum flow depth decreases dramatically from maximum depths of >50 m above the channel in the upper Gorge to maximum depths of ~10 m nearly 50 km before exiting the Gorge, then decreases systematically downstream (**Figure 1.3**). Our simulations suggest effects on hillslope processes should be expected to extend not only higher and more broadly across mountain valleys in a megaflood than in a smaller magnitude LLOF, but also to significant heights farther downstream than in a smaller LLOFs. The following sections discuss flood hydraulics, flood power and bed shear stress to examine erosional and depositional implications of megaflood inundation in more detail.

1.5.2 *Patterns of megaflood and YF flood power and bed shear stress*

Insights into topographic controls on flood hydraulics and patterns of flood power from our simulations are useful for investigating the potential role of different magnitude outburst floods in the evolution of mountain landscapes. The extent of inundation of features like terraces and overtopped ridges dynamically influences locations of high bed shear stress and flood power. Depending on outburst flood size, these features may be inundated and directly cause locally increased speed, bed shear stress, and flood power. The YF simulations gave insight into how an outburst flood interacts with specific landscape features (Turzewski et al., 2019). While we find that the same types of landscape features are important during the simulated megaflood (i.e., overtopped ridges), the greater extent of megaflood inundation means that different individual features are responsible for local increases in both flood power and bed shear stress. Near Tuting, for example, we observe effects on both megaflood and YF hydraulics at the transition from a channel confined by a narrow valley to a channel flanked on either side by terraces and a wide valley where tributaries meet the main Siang River (**Figure 1.7**; Turzewski et al., 2019). In the simulated megaflood, flood power is high (>8 kW/m^2) in the narrower, confined valley north of

Tuting and lower (<4 kW/m^2) near the wide, terrace-filled valley surrounding Tuting (**Figure 1.7**). The YF shows a similar transition from higher (>8 kW/m^2) to lower (<4 kW/m^2) flood power in this area, however this change is directly related to a small valley constriction north of Tuting (**Figure 1.7**; Turzewski et al., 2019). This observation highlights how different inundation levels of different magnitude floods will influence local (<1 km reach) hydraulic patterns and, therefore, depositional and erosional potential.

In both floods, individual landscape features control hydraulic patterns, and measurements of flood power directly reflect the importance of these features as a function of changing inundation levels through time (**Figure 1.7**). Interesting hydraulic patterns develop well after the initial frontal flood wave passes. For example, in the YF a zone of high bed shear stress and flood power near the constriction north of Tuting developed in the waning stage of the flood and persisted for 12 hours (**Figure 1.7**; Turzewski et al., 2019). Similar waning-stage features develop during the simulated megaflood. Three percent of the locations for which we extracted data from GeoClaw (at regularly spaced locations along channel axis) do not experience their highest bed shear stress until the waning stage of the flood (locally variable, but generally >15 hr after breach). Many of the sampled locations that are characterized by high waning-stage bed shear stress are within the Gorge (Figure A5). For example, the one at x = 66 km, experiences a sharp increase from <0.1 kPa (<5 kW/m^2) to >8 kPa (>30 kW/m^2) t = 17 hr after the breach (Figure A5). At this location water pools behind a tight double meander valley-constriction in the Gorge (**Figure 1.6**). When flood inundation decreases enough so that this feature no longer constricts the flow, depth decreases while speed, bed shear stress, and flood power increase. Other locations experience late surges that are not near peak values, but that might be important for transporting sediment during a megaflood. These observations highlight the importance of valley topography on hydraulics of outburst floods through mountain landscapes, both as a function of flood magnitude and evolving flood stage during a given flood event.

1.5.3 *Insights into megaflood erosion and deposition*

For this investigation, we consider bed shear stress, flood power per unit area, and unit stream power as proxies for relative potential for erosion (i.e., bedload motion or rock detachment from channel or from the hillslopes) and deposition in different magnitude flows. This approach is advantageous because the eastern Himalaya preserves no known megaflood erosional features,

likely due to the high exhumation and landslide erosion rates (e.g., Larsen and Montgomery, 2012; Zeitler et al., 2014), making it challenging to link simulated hydraulics to erosional landforms that may indicate specific erosion processes. The rate of bedrock river incision via a variety of processes is commonly taken to depend on local bed shear stress (e.g., Whipple et al., 2000) and to scale with unit stream power (e.g., Scherler et al., 2017; Stock and Montgomery, 1999). Bed shear stress can be used to predict movable particle sizes to link hydraulic simulations to deposit location and grain size or to gain intuition for the scale of potential bedload motion relevant to sediment erosion and deposition (e.g., Bohorquez and Darby, 2008; Cenderelli and Wohl, 2003; Lehnigk and Larsen, 2022; Turzewski et al., 2019). Previous megaflood studies find that high flood power per unit area (>10 kW/m^2) is associated with observed erosional areas, while lower flood power (<5 kW/m^2) is associated with observed depositional areas (Denlinger & O'Connell, 2010). Thus, we suggest that high flood power and bed shear stress may be useful proxies for erosional potential during a megaflood and low flood power and bed shear stress may be useful proxies for depositional potential during a megaflood.

In the following sections, we use our hydraulic simulations to explore general erosional patterns that an eastern Himalayan megaflood might produce. We consider the extent to which megaflood power can be predicted from the modern landscape, namely using unit stream power as a proxy for maximum megaflood power. We also discuss the extent to which there is a scaling relationship between patterns of maximum flood power of the simulated YF and the simulated megaflood, as well as predicted patterns of erosion and deposition during these floods. This exercise focuses on peak flood power in order to highlight spatial trends, which combined with our broader discussion of spatio-temporal trends in flood hydraulics allows us to build intuition for the erosional and depositional potential of these high-magnitude, low-frequency floods.

1.5.3.1 Patterns of megaflood erosional potential

The dynamic nature of the simulated megaflood makes it difficult to define a systematic pattern for megaflood erosional potential. Erosional potential is generally highest at the beginning of the flood and decreases with time, but many locations throughout the flood pathway experience short bursts of higher erosional potential in the waning stage of the flood (Figure A5). Additionally, erosional potential is typically highest in the Gorge and decreases with distance downstream, but there are many downstream locations ($X \geq 250$ km) that experience sustained high erosional

potential for the entire duration of the simulation (**Figure 1.4**d; Movie S16). In fact, in the narrow part of the flood pathway near Tuting, we would expect there to be sustained high erosional potential on the same order of magnitude as in the Gorge for much of the flood (**Figure 1.7**).

Additionally, while a narrower river valley usually results in higher erosional potential, we would not predict high erosional potential everywhere the river valley is narrow. For example, the valley constriction in the Gorge that causes water to pool ~2 km upstream of it (**Figure 1.4**c) has high erosional potential immediately downstream of the constriction and decreased erosional potential upstream of it after t = 20 hr (Movie A12). Often, the portion of the flood pathway directly above the modern channel has the highest erosional potential (**Figure 1.4**), but local increases in erosional potential are also observed elsewhere when relatively high relief features are inundated on the hillslopes (**Figure 1.6** and **Figure 1.7**). Relatively high relief features can be a ridge protruding into a relatively straight part of the channel or high elevation portions of an inundated terrace (**Figure 1.4** and **Figure 1.7**). Features like these will cause local changes in erosional potential that are dynamic depending on the distribution of inundation. This means that erosional patterns will likely be related to the inundated features. In other steep, mountainous landscapes that experience high magnitude outburst floods, we would expect comparable features to have similar effects.

1.5.3.2 To what extent is unit stream power predictive of megaflood flood power in the eastern Himalaya?

While stream power is commonly used as a proxy for erosion patterns for annual flows, we find it does not accurately predict km-scale patterns of where maximum megaflood power is highest. Previous studies have used stream power to estimate the relative power of different megafloods around the world (Benito, 1997; Montgomery et al., 2004; O'Connor, 1993; O'Connor and Waitt, 1995). In the eastern Himalaya, these calculations used coarse scales of channel width and local slope combined with discharge (**Equation 1.4**) to estimate erosional patterns (Montgomery et al., 2004; Lang et al., 2013). However, our results suggest that km-scale erosional patterns from a megaflood do not match these previous estimates based on stream power, but rather reflect the interactions between the rugged eastern Himalayan landscape and megaflood hydraulics. Maximum megaflood flood power and YSR unit stream power are correlated to some extent, as both are higher in the steeper, Gorge region and decrease downstream. Direct correlation, however, is weak when measured at the kilometer scale (**Figure 1.8**a) because valley topographic

features that influence megaflood hydraulics have little effect on modern river flows and channel-forming processes. During annual monsoon flooding, which we suggest represents the channel forming discharge (e.g., Henck et al., 2010), these features are well above maximum inundation, do not influence local channel width, and therefore, do not directly influence patterns of unit stream power. As the length of the reach in question grows (≥10 km), the two values converge to a stronger power-law relationship (**Figure 1.8**a). However, there are complex relationships that depend on the location along flood pathway. For instance, the relationship between stream power and maximum megaflood flood power in the first 100 km of the flood pathway show a different trend than those of the next 100 km (**Figure 1.8**a).

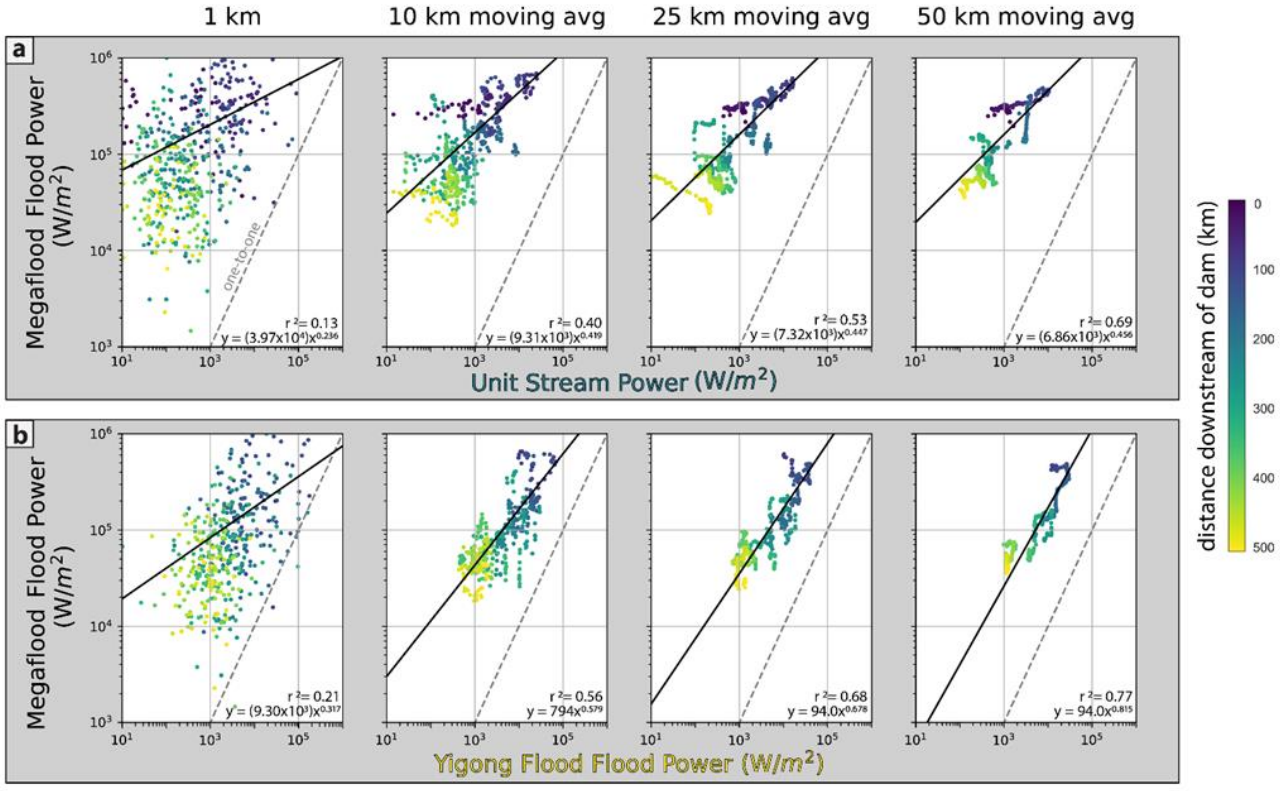

Figure 1.8. Comparison of stream power and maximum flood power, both in Watts per square meter (W/m^2).

Color is coded to distance downstream of dam. The dashed line plotted is one-to-one, while the solid lines represents the best fit line in a least squares sense. Equations for significant power-law regression relationships with r-squared value are shown. An identical plot with the 90th percentile values, instead of maximum values, of flood power can be found in the Supplement (Figure A7).

Our results suggest the differences in inundated valley width and topography are responsible for these relationships. In the Gorge, both the modern channel width and the megaflood inundated width are narrow and result in high unit stream power and maximum megaflood flood power. Further downstream, however, the difference in inundated width for the two flows is large (Figure A6). As discussed above, megaflood inundated valley features like terraces and ridges directly influence patterns of maximum megaflood flood power and bed shear stress. Such valley topographic features influence outburst flood hydraulics but have little effect on modern river flows and channel-forming processes. Therefore, unit stream power and maximum megaflood flood power will have complex scaling relationships that depend on the scale of the valley features inundated in the megaflood. One cannot use local measurements of unit stream power to predict trends in megaflood flood power. However, if interested in general, regional trends in megaflood flood power (≥25 km), unit stream power can serve as a useful predictor of the relative order of magnitude changes in maximum megaflood flood power. This regional relationship between unit stream power and megaflood power is not a uniform powerlaw relationship—there are reach-specific structures to these relationships that begin to develop when averaging >25 km (**Figure 1.8**). The same pattern appears when comparing the 90th percentile megaflood flood power to unit stream power and is even more pronounced (Figure A7), highlighting the importance of reach-specific topographic effects on predicted megaflood erosional patterns. Our analysis suggests that unit stream power measurements can predict order of magnitude shifts in megaflood flood power in steep, mountainous terrain, but will likely miss the effects of reach-specific topography on megaflood hydraulics and, thus, can only serve as a proxy at large spatial scales.

1.5.3.3 Is there a scaling relationship between erosional patterns of lower magnitude outburst floods and megafloods?

Our calculations of maximum megaflood and YF unit flood power can help us determine the extent to which smaller magnitude outburst floods along the YSR can be used as proxies for erosional patterns of megafloods. Like with unit stream power, at the local, kilometer scale, there is a very weak correlation in maximum unit flood power between the two floods (**Figure 1.8**b). As the scale at which flood power is averaged grows, the correlation becomes stronger than that between unit stream power and megaflood flood power for the same averaging distances (**Figure 1.8**b). Whereas the relationship between unit stream power and megaflood flood power data is complex (**Figure 1.8**a), the flood-to-flood power relationship is generally well described by a

power law function (**Figure 1.8**b) beginning at a 25-km moving window. Between x = 250 km and x =~300 km (**Figure 1.8**b), however, a single YF flood power value can have multiple different predicted megaflood flood power values, spanning at least two orders of magnitude. This includes the area surrounding Tuting, where the inundation extents for the two floods are extremely different (**Figure 1.7**). Results further downstream (the yellow data in **Figure 1.8**b), has a similar relationship. This is likely a product of the difference in inundation and the features that are relevant for each flood. While the YF flood power values are closely controlled by the modern channel morphology, the megaflood flood power values are controlled by features on the hillslopes, like inundated ridges or terraces. This difference causes local increases in megaflood flood power in the modern channel where we would not expect it solely based on patterns of YF flood power. Our results suggest that patterns of erosion from a smaller magnitude outburst flood in the eastern Himalaya would be a better proxy for erosional potential of a megaflood than unit stream power. However, this is only the case at broad (≥25 km) spatial scales and does not work for portions of the flood pathway where inundation extents are vastly different. In other steep mountainous landscapes, we would expect similar patterns in flood power between smaller and larger magnitude outburst floods: scaling relationships that are valid for regional changes in flood power, with mismatches occurring where the difference in channel and valley widths is large.

1.5.3.4 Megaflood deposition of slackwater sand and gravel could affect modern erosional processes

Slackwater sand to gravel-sized sediments are important recorders of outburst flood inundation, hydraulics, and recurrence (e.g., O'Connor et al., 2001). Previous workers identified 51 slackwater sand and gravel deposits along the Siang River that are attributed to megafloods sourced from impoundments at Namche Barwa upstream of the Gorge and elsewhere in the YSR headwaters (Table A1; Borgohain et al., 2020; Lang et al., 2013; Panda et al., 2020; Srivastava et al., 2017; Turzewski et al., 2020). It is unknown whether any of these were deposited by a megaflood sourced from failure of a dam of the height and location simulated in this study (i.e., corresponding to the dam location and lower impounded lake level reconstructed by Montgomery et al. (2004)). However, most megaflood slackwater deposits along the Siang valley occur in topographic settings where megaflood slackwater deposits have been observed in other regions (e.g., Benito and O'Connor, 2013; Carling et al., 2009), namely on low relief terraces and at tributary junctions (~67% and ~25% of YSR deposits, respectively) (Table A1; **Figure 1.1**). Thus,

comparing observed deposits to our hydraulics simulation results can provide insight into the hydraulic and landscape features that are important for megaflood deposition along the YSR and in high relief mountain landscapes in general.

The simulated megaflood inundates 44 out of 51 previously identified megaflood deposits, all of which are sand-sized sediment (grain size information in Table A1). At 31 out of the 44 inundated deposits, the simulated megaflood bed shear stress is high enough to transport sand (0.63-2.0 mm) during the rising stage of the flood and low enough to deposit sand in the waning stage (Data Set S1). Bed shear stresses at the other 13 inundated deposit locations remain higher than the bed shear stress required to transport sand for the entire duration of inundation (Data Set S1). These results show that a megaflood of the magnitude we simulated could deposit sand at most of the previously identified slackwater deposit locations. Although these deposits likely do not come from the same flood event, the broad consistency of simulated inundation and hydraulic patterns with the deposit locations generally supports the accuracy of the 2D hydraulic modeling approach (Carrivick, 2006; Bohorquez and Darby, 2008; Denlinger and O'Connell, 2010).

In general, we observe local topographic controls on simulated flood hydraulics that predict deposition of sand-sized particles in wide portions of the river valley. Hydraulics indicative of sand-sized deposition may be controlled locally at the 1-5 km-reach scale by topography (a) around channel/valley widening, (b) upstream of inundated obstacles (i.e. ridges, tight meanders), and (c) on top of low-relief surfaces that are inundated. For example, such features occur near Tuting and lead to hydraulics that predict sand deposition on the low relief terraces that flank the Siang River there (**Figure 1.7**). Ridges that protrude into the narrow, confined valley cause local gradients in speed, bed shear stress, and flood power that are relatively stable while the ridges are inundated. In contrast, when the low relief features of the terraces at Tuting are inundated, dynamic spatial and temporal gradients in speed, bed shear stress and flood power appear—these patterns are expected to increase the likelihood of megaflood deposition on those low relief terraces (**Figure 1.7** and associated movies). On those Tuting terraces, multiple generations of megaflood slackwater sand deposits have been identified (Borgohain et al., 2020; Lang et al., 2013; Panda et al., 2020; Turzewski et al., 2020), all of which experience sufficient bed shear stress to transport sand (Data Set S1). This correspondence supports the idea that our simulation of a specific reconstructed megaflood event can provide general insight into relationships between topography, megaflood hydraulics, and deposition in steep terrain.

In addition to predicted depositional areas discussed above, we expect that tributaries that are subjected to megaflood backflow to experience exceptional deposition of sand- and gravel-sized sediment. For example, the two tributaries to the Siang at Tuting experience ~8-12 km (**Figure 1.1**, **Figure 1.7**, and associated movies) and the Siyom River experiences ~60 km (**Figure 1.1** and **Figure 1.6**) of megaflood backflow inundation. While previous workers have not reported megaflood deposits along the Siyom River (Misra & Srivastava, 2009), we observe similar bed shear stress and flood power to those on the Tuting terraces; therefore, we would expect to find megaflood deposits with similar grain sizes throughout the Siyom River valley. Such a pulse of sediment supplied to the channel could have profound effects of fluvial processes, such as in the Altai floods where megaflood deposition along tributaries led to a temporarily dammed tributary (e.g., Carling et al., 2002; Herget et al., 2020). Depending on the spatial distribution of megaflood deposited sand and the stream power of the tributary in question, such deposition could be either be enough to transition the system from detachment limited into a transport limited scheme, preventing the river from incising into its bedrock,k or provide the necessary tools with which to more efficient incise into its bedrock (e.g., Gasparini et al., 2007; Johnson et al., 2009; Sklar & Dietrich, 2004; Turowski et al., 2007).

We hypothesize that widespread megaflood deposition of sand-sized particles on low-gradient surfaces could impede erosional processes on hillslopes, changing the rate at which sediment moves through the system. Sediment deposited on low-gradient hillslopes is likely mobilized during megafloods (see bed shear stresses from **Figure 1.7**), but there is evidence that flood deposits along the Siang River can remain on certain hillslopes for hundreds to thousands of years (Borgohain et al., 2020; Panda et al., 2020; Turzewski et al., 2020). A positive feedback loop could occur in which (a) lower gradient hillslopes have a higher likelihood of megaflood deposition and (b) megaflood deposits have higher residence times on these lower gradient surfaces, which (v) reinforces the lower gradient of that surface, (d) making it more likely that the next megaflood (or outburst flood that inundates hillslopes) will deposit sediment on that surface. If low gradient topography is created along the YSR, for instance via landsliding or alluvial deposition, and a megaflood happens shortly after, that feature will likely exert an influence on megaflood hydraulics, causing local deposition of sand around/on top of it. The low recurrence interval of megafloods throughout the Quaternary (eight floods between 1 and 7 ka, Panda et al., 2020) means that sediment deposited on low gradient hillslopes will likely remain in the system

for hundreds to thousands of years between megafloods, showing a link between deposition and evolution of the valley morphology over long timescales.

1.5.3.5 Megaflood deposition of boulders could impede modern bedrock river incision rates

Previous workers have speculated about the relationship between large outburst floods and meter-scale or larger boulders. On two central Nepalese rivers, boulders too large to be mobilized during annual monsoon floods (1-10 m in diameter) have been observed and are hypothesized to have been deposited by GLOFs (Cook et al., 2018; Huber et al., 2020). These studies suggest that boulders are moved and deposited during GLOFs or LLOFs and then become long-lived features in the landscape—meteoric floods may abrade, but do not produce high enough bed shear stresses to move these large boulders. Along the YSR, Turzewski et al. (2019) identified >70 boulder bars with boulders 1-12 m in diameter potentially related to either LLOFs such as the YF or megaflooding, which we examine in light of our new megaflood simulations.

We hypothesize that many of the >70 boulder bars along the YSR are remnant megaflood deposits. While it's impossible to directly link the stability or movement of individual boulders to the simulated megaflood, we can consider the general mobility and the potential source of these boulders. For example, at Tuting, our field observations reveal at least 11 boulder bars with boulders >4 m in diameter—too large to be moved by either the annual monsoon or the YF (**Figure 1.7**; Figure A8). Additionally, most of these boulders are granodioritic (Figure A8), while the local bedrock lithology is metasedimentary. This difference suggests that the boulders were either derived from the bedrock channel or hillslopes upstream of Tuting. Simulation results show that megaflood hydraulics in the Tuting area can produce bed shear stresses >3 kPa and flood power >10 kW/m^2, enough to mobilize a boulder that is ~8 m in diameter on the local measured channel gradient (**Figure 1.7**). Spatial and temporal flow gradients during the simulated megaflood produce high enough bed shear stress and flood power to mobilize these large boulders and then subsequently deposit them in the area (**Figure 1.7**). For these reasons, we suggest that most of the boulders >4 m in diameter that we observe around Tuting were mobilized to the region and deposited during megaflooding and have not been moved by smaller-magnitude modern flows. The same is likely true for large boulders in boulder bars throughout the YSR.

The persistence of large grains in the landscape between megafloods likely influences where the modern river can incise into its bed. The prevalence of large boulder bars along the YSR

indicates the stability of these large grains. These boulders will remain in the landscape either until the next megaflood or until the boulders are winnowed to a small enough diameter to move in lower magnitude flows. Unlike monsoon related boulder-deposition, these boulders will be in positions directly related to megaflood hydraulics. Boulders deposited in these locations can armor the bed, increase roughness, and prevent incision, potentially changing the way that the modern river erodes (Cook et al., 2018; Sklar & Dietrich, 2004; Shobe et al., 2016; Turowski et al., 2008; Turzewski et al., 2019). Boulder presence in river channels may cause changes in channel width and/or produce "stepped" profiles due to the spatial heterogeneity in boulder deposition along the profile (Shobe et al., 2016, 2021). Because of this, we hypothesize that the deposition of large boulders during a megaflood is a key way in which megafloods exert long-term influence on bedrock incision patterns of the YSR.

1.6 CONCLUSIONS

This study represents the first 2D numerical simulation of a megaflood in the eastern Himalaya sourced from an 81 km^3 lake. The simulated megaflood reaches a maximum breach discharge of 3.1 x 10^6 m^3/s, over three times as large as the predicted discharge based on dam breach geometry and lake volume. Our simulations allow us to gain intuition for how megaflood erosion and deposition is likely to be distributed throughout the Yarlung-Siang River valley and what that might mean for high-magnitude outburst floods in other steep, mountainous regions. Megafloods not only produce higher flood power than smaller magnitude outburst floods, they also produce different patterns of erosional potential—patterns that are directly related to inundated valley topography. We found that features like tight meander bends and ridges are important for controlling local megaflood hydraulics, but might also influence hydraulics up to 5 kilometers away. For instance, while features like valley narrowing are often indicative of high megaflood erosional potential, a downstream feature could cause water to pool at a relatively narrow location, causing a decrease in erosional potential. Additionally, in places where the valley is wide, interactions between megaflood water and terrace topography near the town of Tuting cause local increases in bed shear stress and flood power similar in magnitude to the narrowest region of the flood pathway, the Yarlung-Tsangpo Gorge. Patterns of bed shear stress and flood power are dynamic in time and space, changing constantly with distribution of inundation.

Previous megaflood studies have used stream power to estimate the relative power of different megafloods around the world (e.g., O'Connor & Beebee, 2009), but our results indicate that unit stream power and flood power from a lower magnitude LLOF both do a poor job of predicting local patterns of megaflood flood power and, thus, erosional potential. In a comparison between maximum megaflood flood power and modern unit stream power, we find no relationship at the local, kilometer scale. At larger spatial scales (≥25 km) a stronger power-law relationship develops, but does not capture the reach-scale topographic changes that are directly responsible for megaflood hydraulics important for erosion. We caution against using stream power patterns to predict patterns of megaflood erosion in steep, mountainous terrain, without first considering the scale of the question of interest. In a comparison between maximum megaflood flood power and flood power of the 2000 Yigong Flood, we find a stronger power-law relationship at the larger (≥25 km) scale, but little to no relationship at the kilometer scale. While the same types of features cause the same types of hydraulics in the larger flood, the individual features responsible for erosion relevant hydraulic patterns differ depending on the magnitude of inundation. The power-law relationship at the larger, regional scale breaks down in locations downstream of the Gorge due to drastic differences in channel/valley widths and the extent of inundated topography. Our results suggest that using smaller magnitude outburst floods to predict patterns of megaflood flood power is a useful tool in high relief mountainous terrain, except in locations where floods inundate significantly different types of topography, like ridges or terraces that are high above the modern river.

Our findings also include a link between megaflood hydraulics and sand to boulder-size deposition, with potential implications for long-term river and hillslope processes in the YSR and in other mountainous landscapes that experience megaflooding. We predict widespread megaflood deposition of sand-sized particles on low-gradient surfaces that flank the river where the valley is wide. We would also expect significant deposition of slackwater sand along inundated tributaries, potentially enough to change the ability of that tributary to incise into its bedrock. We hypothesize that many of the 70+ boulder bars along the YSR are remnant megaflood deposits. These boulders are too large to be moved by smaller flows and will persist in the landscape, limiting river incision at the location of the boulder bar. In these two ways, we suggest that megaflood deposition can control the rate at which the landscape can evolve after a megaflood—a result that suggests the

depositional legacy of megafloods may be more important for mountain landscape morphology than previously recognized.

2. **CHAPTER 2**: Sedimentary evidence of Quaternary megaflood deposition in the Siyom River valley, eastern Himalaya

In preparation for submission to *GSA Bulletin*; coauthors: Susannah M. Morey, Karl A. Lang, Katharine W. Huntington, Charles M. Shobe, Srinanda Nath, Chloe Loreen

Numerical simulations of an eastern Himalayan megaflood reveal extensive backflooding along the Siyom River valley of the eastern Himalaya. Backflood deposits are useful to reconstruct paleoflood magnitude, frequency, and source, yet they are rarely preserved in mountain landscapes. We investigate evidence of Quaternary megaflood backflooding in the sedimentary record of the Siyom River valley using fluvial terrace sedimentology and stratigraphy as well as radiocarbon and detrital zircon U-Th-Pb geochronology. We identified three fill terraces within the maximum inundation levels of the simulated megaflood. Within one of those terraces, we find evidence for typical fluvial deposits, but also several sequences of deposition from deep stagnant and turbulent waters consistent with simulated megaflood inundation and flow conditions. The highest of these deposits shows calibrated radiocarbon age ranges (2σ) of 10,560-10,710 cal yr BP and 10,660-10,820 cal yr BP. These ages correspond to the timing of paleolakes on the Tibetan Plateau—the source of eastern Himalayan megafloods. We therefore interpret that T2 contains a record of deposition during megaflood backflooding and hypothesize that other terraces within the Siyom River valley likely contain other evidence for megaflood backflooding.

2.1 INTRODUCTION

Extensive backflooding is common during dam break outburst flooding, particularly megafloods with discharges $>10^6$ m^3/s (e.g., Bretz, 1929; Komatsu et al., 2009; Schmidt et al., 2009; Carling et al., 2010; Waitt, 2016; O'Connor et al., 2020; Benito and Thorndycraft, 2020; Denlinger et al., 2021; van der Bilt et al., 2021; Nag et al., 2022). Slackwater deposits are key to reconstructing paleoflood magnitude, frequency, and source (Kochel et al., 1982; Baker et al., 1983; Greenbaum et al., 2014; Guo et al., 2023). However, backflooding deposits are rare in the sedimentary record and the processes leading to their deposition and post-depositional preservation

are not well understood. This is especially true in steep mountain landscapes where fine sediment has relatively short residence times (e.g., Hodge et al., 2011; Nelson and Dube, 2016).

In the eastern Himalaya, there is ample evidence for megafloods throughout the Quaternary (e.g., Montgomery et al., 2004; Lang et al., 2013; Song et al., 2013; Liu et al., 2015; Turzewski et al., 2020; Xu et al., 2020), making it a potential natural laboratory for studying these processes. Simulations of a megaflood sourced from a reconstructed 81 km^3 glacial paleolake impounded on the Tibetan Plateau predict extensive backflooding up a tributary of the main flood pathway (Morey et al., 2022). The inundated tributary—the Siyom River (**Figure 1.1**)—is an anomalously low sloping river flanked by aggradational fluvial terraces. If the Siyom were inundated during megaflooding throughout the Quaternary, we would expect the valley to have a rich archive of eastern Himalayan megaflooding. This study focuses on interpreting topography and deposits along the Siyom River valley to answer the question: To what extent can terrace development and sedimentary deposits within the Siyom River valley be explained by megaflood backflooding inundation?

To assess this question, we mapped low relief terraces through the Siyom valley and conducted field work to document terrace sedimentology and stratigraphy to interpret depositional environments. We provide new radiocarbon dates to constrain deposit chronology and detrital zircon U-Th-Pb geochronology to assess sedimentary provenance. Interpreted in the context of previous flood studies and hydraulic modeling in the region, our detailed field study provides new insight into the complex legacy of megaflood deposits in this river system.

2.2 BACKGROUND

As the largest tributary of the Siang River, the 2250 km^2 Siyom River catchment has an anomalously low relief drainage compared to other tributaries of the Yarlung-Siang River (YSR) (Jha, 2021). Unlike other Siang tributaries, the Siyom transitions from a bedrock channel in its headwaters to a braided alluvial system before transitioning back to a bedrock gorge near its confluence with the YSR. The catchment has an overall relief of 3550 m, 300 m of which is represented in **Figure 2.1**. The Siyom River predominantly drains metasedimentary rocks of the Lesser Himalayan Sequence (LHS) exposed on the western limb of the Siang Antiform (e.g., Salvi et al., 2021), although the headwaters access Greater Himalayan Sequence (GHS) lithologies across the Main Central Thrust (Clarke et al., 2016; Hooker, 2022). Other mapped faults in the

region include the Tuting Basar Strike-Slip Fault and the Ramgarh Thrust, although, the activity and exact location of the latter is debated (e.g., Salvi et al., 2021; Hooker, 2022).

Slackwater deposits have been studied extensively as a record of glacial lake outburst megafloods in the eastern Himalaya (**Figure 2.1a**). The headwaters of the Yarlung-Siang-Brahmaputra River on the Tibetan Plateau were impounded by glacial moraine dams throughout the Quaternary (e.g. Liu et al., 2006; Montgomery et al., 2004; Xu et al., 2020). Recent numerical modeling of eastern Himalayan megafloods predicts deposition in sheltered areas along the Yarlung-Siang River (YSR) and up adjoining tributaries. More than 50 deposits have been identified within and beside the YSR, but no work has yet looked for slackwater deposition in tributaries. We focus on the largest tributary, the Siyom River, in which models predict more than 50 hours of megaflood backflow inundation (Morey et al., 2022). In these simulations, backflow extended up to 60 km upstream of the Siyom confluence with the YSR, reaching flow depths of up to 110 m, (**Figure 2.1b**). The depth, speed, shear stresses, and flood power produced during these simulations indicate a high capacity for transporting sediment ranging up to cobbles.

Previous workers have reported thick sedimentary deposits within the Siyom River valley interpreted to be alluvial and lacustrine deposits attributed to local damming by active faulting (Misra and Srivastava, 2009). However, the significance of valley-crossing structures to potential damming-related deposits remains ambiguous. Acharyya and Saha (2008), Misra and Srivastava (2009), and Salvi et al. (2021) all identified faults within the valley, but disagree about the location, activity, and type of faulting. More recent field mapping of lithotectonic and lithostratigraphic relationships (Figure 3.2; Hooker, 2022) alternatively finds no evidence for active faults cross-cutting the Siyom downstream of Aalo(ng).

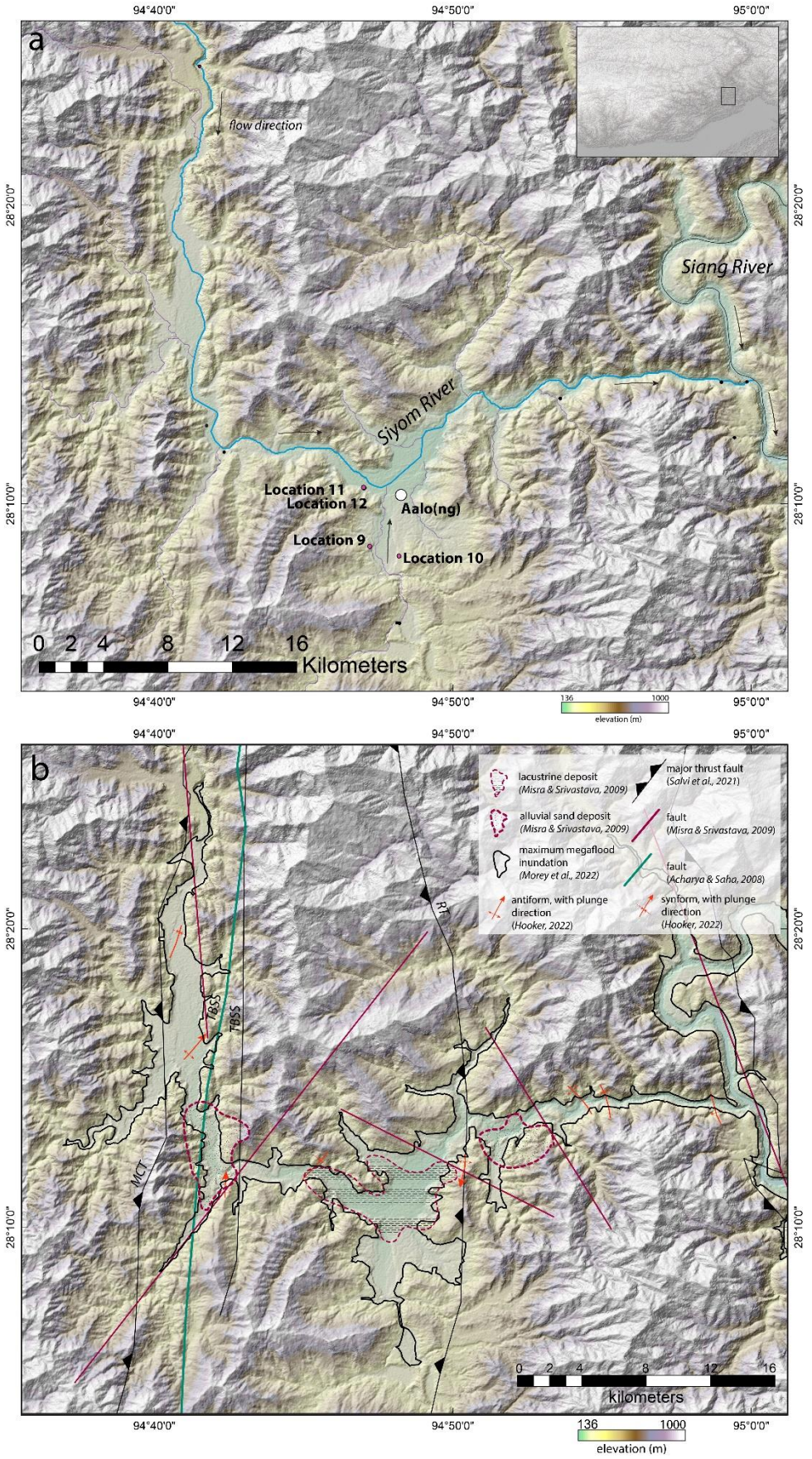
a
94°40'0"
94°50'0"
95°0'0"
28°20'0"
28°10'0"
flow direction
Siang River
Siyom River
Location 11
Location 12
Aalo(ng)
Location 9
Location 10
0 2 4 8 12 16
Kilometers
136
1000
elevation (m)
b
lacustrine deposit
(Misra & Srivastava, 2009)
alluvial sand deposit
(Misra & Srivastava, 2009)
maximum megaflood inundation
(Morey et al., 2022)
antiform, with plunge direction
(Hooker, 2022)
major thrust fault
(Salvi et al., 2021)
fault
(Misra & Srivastava, 2009)
fault
(Acharya & Saha, 2008)
synform, with plunge direction
(Hooker, 2022)
MCT
STDS
STDS
RT
0 2 4 8 12 16
kilometers
136
1000
elevation (m)

Figure 2.1. A regional map of the Siyom River valley in the eastern Himalaya.

a) Includes sample Locations 9, 10, 11, and 12 (pink dots). Black dots are other samples taken during fieldwork in 2019. b) structural features of the Siyom River valley with simulated maximum inundation of a megaflood from the failure of a dam on the Tibetan Plateau (Morey et al., 2022). TBSS = Tuting Basar Strike-Slip; MCT = Main Central Thrust; RT = Ramgarh Thrust.

2.3 METHODS

We investigate the potential for a megaflood origin of fine-grained deposits in the Siyom River valley by mapping fluvial terraces, describing sedimentary sections, radiocarbon dating, and detrital zircon provenance analysis. We are interested in (1) geographically widespread, consistent fluvial terrace elevations above the modern Siyom river, but below the maximum extent of predicted megaflood inundation, (2) sedimentary features that might indicate unusual depositional processes not expected in gravel bedded alluvial rivers, (3) ages that correlate to dated paleolakes on the Tibetan Plateau, and (4) foreign provenance signatures that are not expected given the Siyom drainage.

2.3.1 *Terrace mapping*

Fill terraces were mapped using a 12.5 m DEM constructed for the Siyom River valley using RTC (radiometrically terrain corrected) products from ALOS PALSAR (Advanced Land Observing Satellite Phased Array L-band Synthetic Aperture Radar) (Japan Aerospace Exploration Agency, 2021). Using Topotoolbox (Schwanghart and Scherler, 2014), we mapped terrace surfaces by identifying DEM cells with a mean slope less than 7° that were within 2 km of the main Siyom River channel or large tributaries with more than 10^3 m^2 drainage area. To match terraces surfaces by elevation, we calculated the relative elevation of terrace cells above the nearest channel and binned elevation in a histogram grouped by cell count (**Figure 2.2**). Peak elevation ranges were also checked for consistency with field observation of terrace elevations.

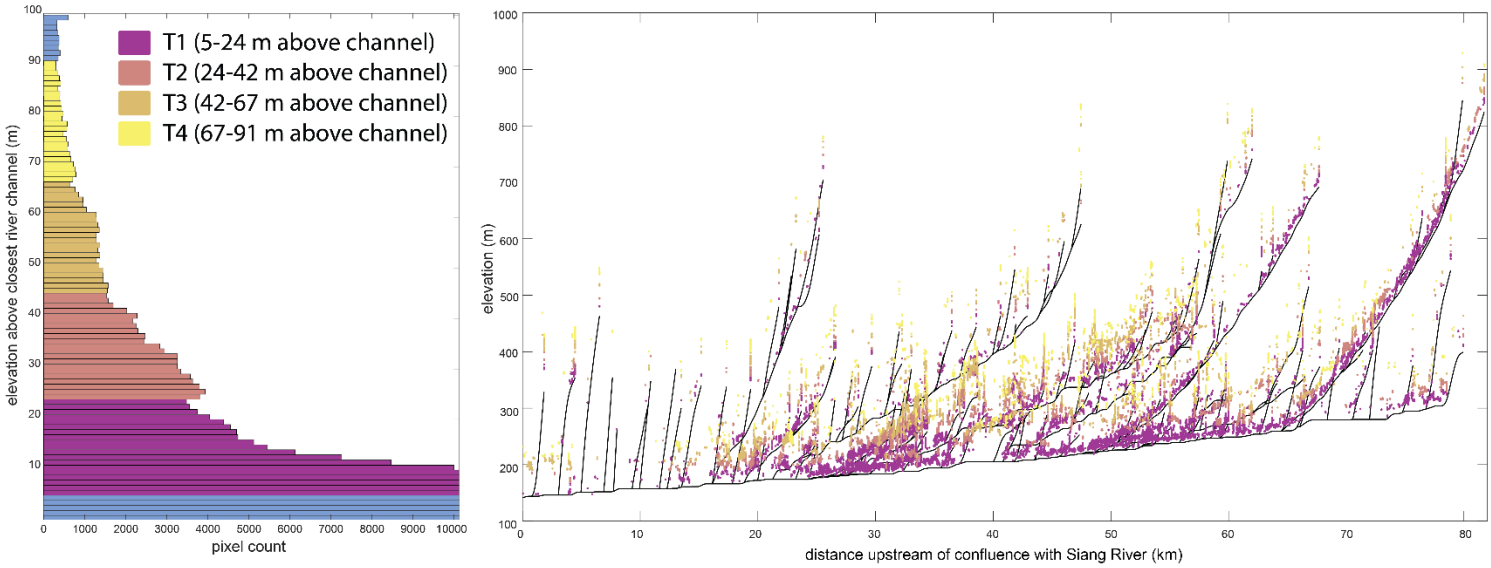

Figure 2.2. Methods for determining terrace elevations.

a) Histogram of elevations throughout the Siyom River valley b) terrace elevations plotted on Siyom River and tributaries longitudinal profiles

2.3.2 *Field observations of sedimentary deposits and grain size analysis*

Terrace deposits are concentrated in the Siyom River valley and adjoining tributaries 26 km, 27 km, and 35 km upstream of the Siang River confluence (**Figure 2.1**). We describe detailed sedimentary deposits in 8 vertical sections from 2 locations (Locations 11 and 12) in this valley from field observations collected in November of 2019 (**Figure 2.3**). Location 11 is ~70 m west and stratigraphically lower compared to Location 12. Sections were measured with a 2 m tape and described from excavated profiles in the field. Particle sizes for most deposits were estimated in the field by visual comparison with a grain size card, and quantitative particle size analysis of 100 g samples was conducted for key units. Each sample was sieved with a 1.4 mm (-0.4 φ) sieve to remove large grains prior to particle size analysis. The finer grain size fraction was analyzed at Georgia Tech using a Malvern Mastersizer 3000 laser diffraction particle size analyzer equipped with a HydroEV wet dispersion unit. Field descriptions of sedimentary features observed in different facies are described in **Table 2.1** and detailed stratigraphic columns can be found in **Appendix B** (**Figures B1 & B2**).

2.3.3 *Radiocarbon dating*

We collected wood, peat, clay, and silt samples from a variety of facies for radiocarbon dating. Samples were collected from internal cohesive sediments and manually inspected for rootlet contamination using a stereomicroscope. Radiocarbon dating of 11 samples was performed at the University of Georgia Center for Applied Isotope Studies accelerator mass spectrometry facility. Samples were pre-treated with hot HCl to remove any carbonate contamination. Radiocarbon ages were calibrated using CALIP REV8.2 (calibration dataset: incal20.14c; Stuiver and Reimer, 1993; Reimer et al., 2020). To compare to ages of known paleolakes on the Tibetan Plateau thought to be the source of megafloods, we recalibrated radiocarbon ages from Montgomery et al. (2004) using the same calibration dataset.

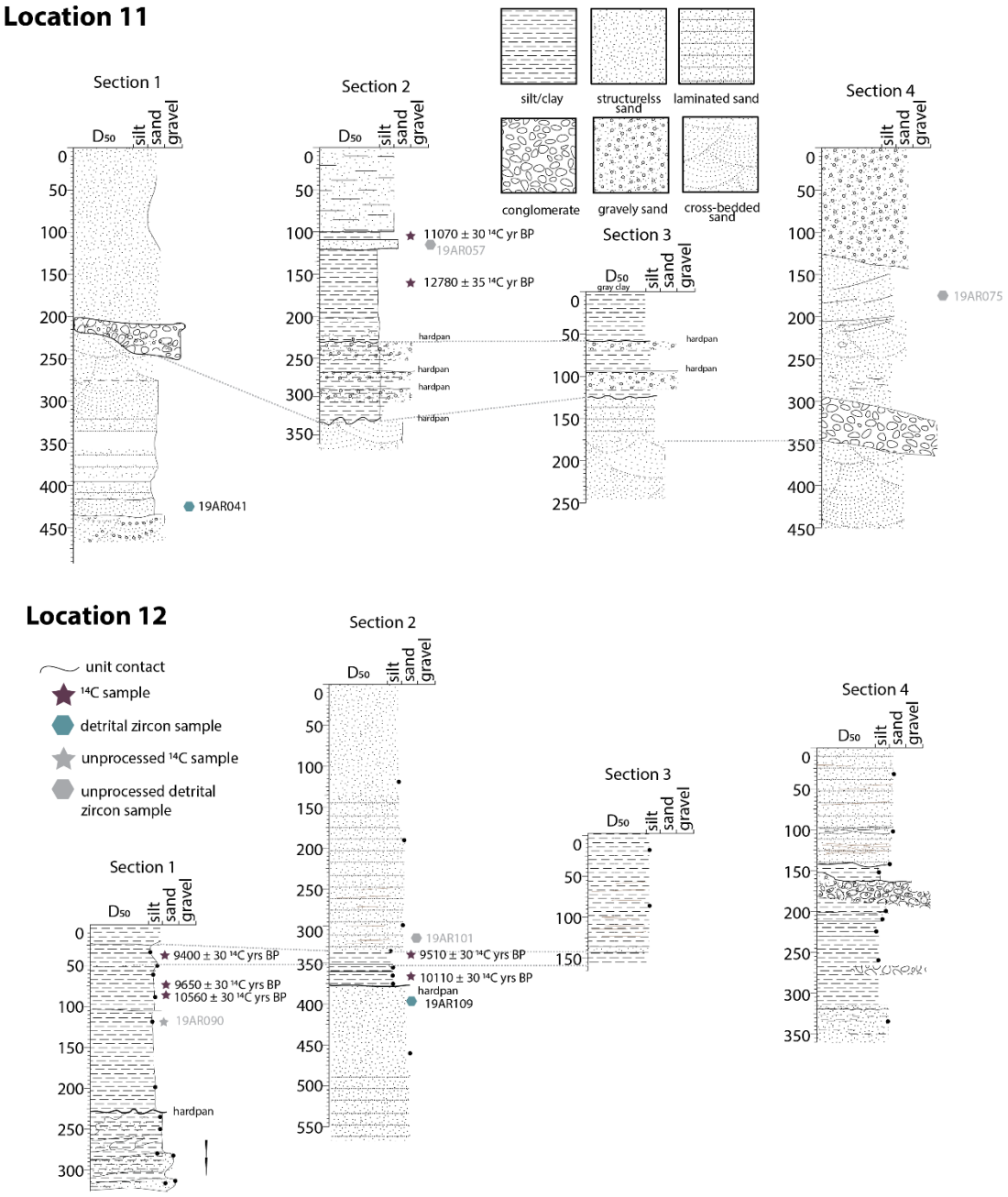

Figure 2.3. Stratigraphic columns from Locations 11 and 12.

Table 2.1. Sedimentary facies observed in the Siyom River valley

Facies ID	***Facies name***	***Sedimentary structures***	***Occurrence***	***Interpreted depositional environment***
A	Cross-bedded sand	Unconsolidated coarse sand to fine gravel, 20-25 cm thick bed of fine gray sand, faint fine laminations or massive. Very fine to medium, moderately sorted sand with long-wavelength trough crossbedding. Locally oxidized (visible in 11.11-7 and 11.11-3) and exhibits secondary deformation and bioturbation	Location 11, Sections: 1, 2, 3, 4 Location 12, Sections: 1	Seasonal depositional of fluvial suspended load
B	Cobble conglomerate	A matrix supported pebble and cobble conglomerate with occasional boulders. Clasts are rounded and show crude imbrication. Matrix is alternatively sand-rich and clay rich. Irregular, unconformable base and top.	Location 10 Location 11, Sections: 1, 4 Location 12, Sections: 4	Fluvial bedload channel lag
C	Structureless sand	Silt and fine sand with faint flat and steeply dipping laminations that grade into structureless, poorly sorted silt to very coarse sand	Location 11, Sections: 1 Location 12, Sections: 1, 2, 3, 4	Event deposit; rapid deposition from suspension
D	Sequential silts, coarse sands, and gravels	Sequences of silt to medium sand that grade into silt to coarse sand with gravel and pebbles. Irregular, unconformable base and top of each sequence. Contacts exhibit oxidized secondary groundwater alteration. Rare flame structures are present that inject coarse sands into facies on top.	Location 11, Sections: 2, 3 Location 12, Sections: Section 1	Complex, energy changing flow
E	Clay and silt	Structureless clay and silt beds; Irregular, unconformable base where contact exhibits oxidized secondary groundwater alteration. Color can be blue-gray, gray, or white. At Location 11, base is oxidized and faintly laminated with some fine sand.	Location 11, Sections: 2, 3 Location 12, Sections: 1,2,3,4	Event deposit; deep, stagnant water;
F	Laminated silt to structureless sand	Wavy laminated mm-scale silts and fine sands that alternate from light brown to orange that grades into lightly laminated fine sand and then structureless silt to medium sand.	Location 12, Sections: 2, 3, 4	Event deposit; rapid deposition
G	Peat	Black to dark brown organic rich peat layer. Very dense, crumbly and dry.	Location 12, Sections: 1, 2, 3, 4	Deep stagnant, organic rich water;

Table 2.2. Radiocarbon data for sediment samples in the Siyom River valley.

Unique Sample number	**sample name**	**latitude**	**longitude**	**elevation**	**sample material**	**Radiocarbon Age** (^{14}C yr BP)	**Radiocarbon Uncertainty** (1σ)	**Median Probability** (cal BP)	**1σ** (cal BP)	**1σ** relative fractional area under probability distribution	**2σ** (cal BP)	**2σ** relative fractional area under probability distribution
19AR004	09.1C	28.10003	94.802223	353.81	wood	52620	-	-	-	-	-	-
19AR005	09.1D	28.100027	94.802223	353.81	clay	29400	90	34020	33874 - 34168	1	33278 - 34287	1
19AR007	09.2B	28.142723	94.787010	367.55	silt/sand	9410	30	10640	10582 - 10634	0.583	10523 - 10529	0.007
									10643 - 10682	0.417	10564 - 10735	0.993
19AR021	10.1N	28.137646	94.802963	320.33	silt/sand	15410	40	18750	18705 - 18785	1	18665 - 18819	1
19AR022	10.1O	28.137646	94.802963	320.33	silt/sand	20200	50	24240	24131 - 24322	1	24046 - 24511	1
19AR024	10.4W	28.19528	94.705681	313.12	silt/sand	14230	40	17280	17144 - 17217	0.319	17104 - 17410	1
									17271 - 17388	0.681		
19AR047	11.1-5V	28.175663	94.783386	286.16	clay	12780	35	15240	15173 -15300	1	15099 - 15392	1
19AR056	11.1-5W	28.175663	94.783386	286.16		11070	30	13010	12934 - 12939	0.031	12910 - 13088	1

									12968 - 13077	0.969		
19AR087	12.1-1L	28.175159	94.783909	290	peat	9400	30	10630	10577 - 10663	0.974	10513 - 10538	0.041
									10673 - 10677	0.026	10556 - 10713	0.959
19AR088	12.1-1M	28.175159	94.783909	290	clay	9650	30	11080	10882 - 10925	0.276	10800 - 10852	0.088
									11076 - 11172	0.724	10866 - 10960	0.32
											11007 - 11026	0.025
											11067 - 11187	0.567
19AR089	12.1-1N	28.175159	94.783909	290	clay	10560	30	12600	12496 - 12536	0.536	12486 - 12546	0.455
									12609 - 12625	0.185	12590 - 12682	0.545
									12641 - 12667	0.279		
19AR107	12.1-4F	28.175159	94.783909	290	peat	9510	30	10780	10703 - 10782	0.626	10660 -10820	0.571

									10971 - 10999	0.224	10845 - 10872	0.038
									11039 - 11061	0.151	10950 - 11069	0.391
19AR108	12.1-4G	28.175159	94.783909	290	clay	10110	30	11720	11645 - 11668	0.164	11405 - 11434	0.029
									11692 - 11769	0.537	11497 - 11559	0.071
									11771 - 11814	0.299	11562 - 11574	0.006
											11602 - 11834	0.894
Beta-169377	L3 (low terrace)	*See Montgomery et al. (2004)*			wood	1220	40	1140	-	-	1010-1020	0.070
									-	-	1050-1280	0.948
Beta-168580	L5 (low terrace)	*See Montgomery et al. (2004)*			wood	1660	40	1550	-	-	1660-1700	0.081
											1410-1620	0.0873
Beta-168578	L2 (high terrace)	*See Montgomery et al. (2004)*			wood	8860	40	9990	-	-	9760-10180	0.954
Beta-168579	L6 (high terrace)	*See Montgomery et al. (2004)*			wood	9870	50	11270	-	-	11190-11410	0.954
											11450-11470	0.040

2.3.4 *Detrital zircon geochronology*

We processed three sand samples for detrital zircon U-Th-Pb geochronology. Analysis of detrital zircon U-Th-Pb crystallization ages is a well-developed method for interpreting the provenance of sedimentary deposits in the Yarlung-Siang-Brahmaputra river system (e.g., Zhang et al., 2012; Lang et al., 2013; Lang et al., 2014; Turzewski et al., 2020). Samples 19AR041 is from Facies A at Location 11 and 19AR109 is from Facies C at Location 12 (**Figure 2.1**), while 19AR025 is from an active bar on the Siyom River, upstream of the maximum extent of backflow inundation predicted from hydraulic simulations of an 81 km^3 lake failure on the Tibetan Plateau (Morey et al., 2022) (**Figure 1.1**). Zircons were separated using standard heavy mineral separation procedures at the University of Washington (Licht et al., 2019; Shekut & Licht, 2020). Grains were co-mounted with reference minerals (R33, FC-1, Sri Lanka standard), polished, and imaged using electron backscatter and cathodoluminescence detectors on a Hitachi 3400N SEM equipped with a GatanCL2 cathodoluminescence detector. Zircon cores were systematically targeted for isotopic measurements via laser ablation using a Photo Machines Analyte G2 excimer laser coupled to a Nu Plasma MC-ICP-MS at the Arizona LaserChron Center (Gehrels et al., 2008). Analytical protocol for isotope measurements follows Gehrels et al. (2008), Gehrels and Pecha (2014) and Pullen et al. (2018). U-Th-Pb data were reduced using E2agecalc (Gehrels et al., 2008) and visualized in **Figure 2.4** using Density Plotter (Vermeesch, 2012).

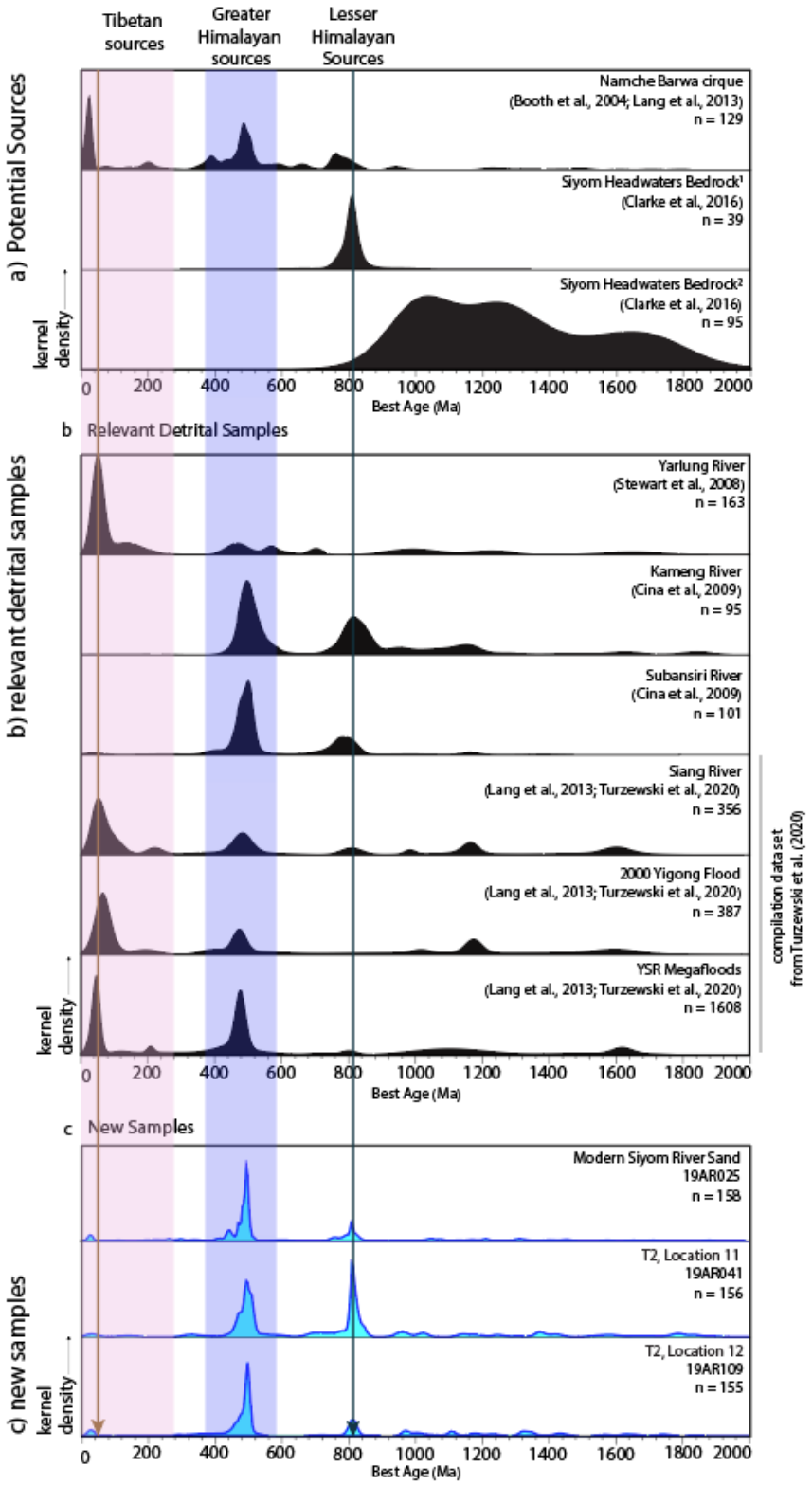

Figure 2.4. U-Pb detrital zircon kernel density plots created using DensityPlotter

a) bedrock source regions b) detrital zircon samples from previous studies that are relevant c) new samples. The gold line represents the age peak at ~50 Ma that is characteristic of Yarlung River samples. The pink swath represents

Tibetan aged sources. The blue swath represents Greater Himalayan Sources and the blue line represents Lesser Himalayan sources.

2.4 RESULTS

2.4.1 *Terrace mapping*

We identified four terrace surfaces at different relative elevations above the modern Siyom River channel: T1 (5-24 m), T2 (24-42 m) T3 (42-67 m) and T4 (67-91 m relative elevation) (**Figure 2.2; Figure 2.5**). Terrace surfaces between 0 and 5 m above the nearest channel are interpreted to represent the active channel and floodplain and are therefore omitted from analysis. T1 has the best preserved surface and is prevalent throughout the valley. It is an aggradational terrace closest to the modern Siyom channel and contains densely vegetated bars that are often cleared for agriculture (**Figure 2.8;** samples 19AR041, 19AR109, and 19AR008-024). T2 is a dissected aggradational terrace upon which the town of Aalo(ng) sits. Locations 11 and 12 (**Figure 2.8**) are from within T2. Elsewhere in the Siyom River valley, smaller villages are also located on T2. T3 is an aggradational terrace above T2 and the highest elevation houses in Aalo(ng) are upon it. T3 contains an outcrop of several meters of imbricated rounded cobbles topped by several meters of fine sediment with a reddened, well-developed soil profile (Figure B3; samples 19AR008-024). T4 is a bedrock strath terrace topped by sandy beds (samples 19AR006, 19AR007, 19AR027) and consists of the highest low relief surfaces in the valley. This is the least common terrace and is highly dissected in the upper reaches of the valley.

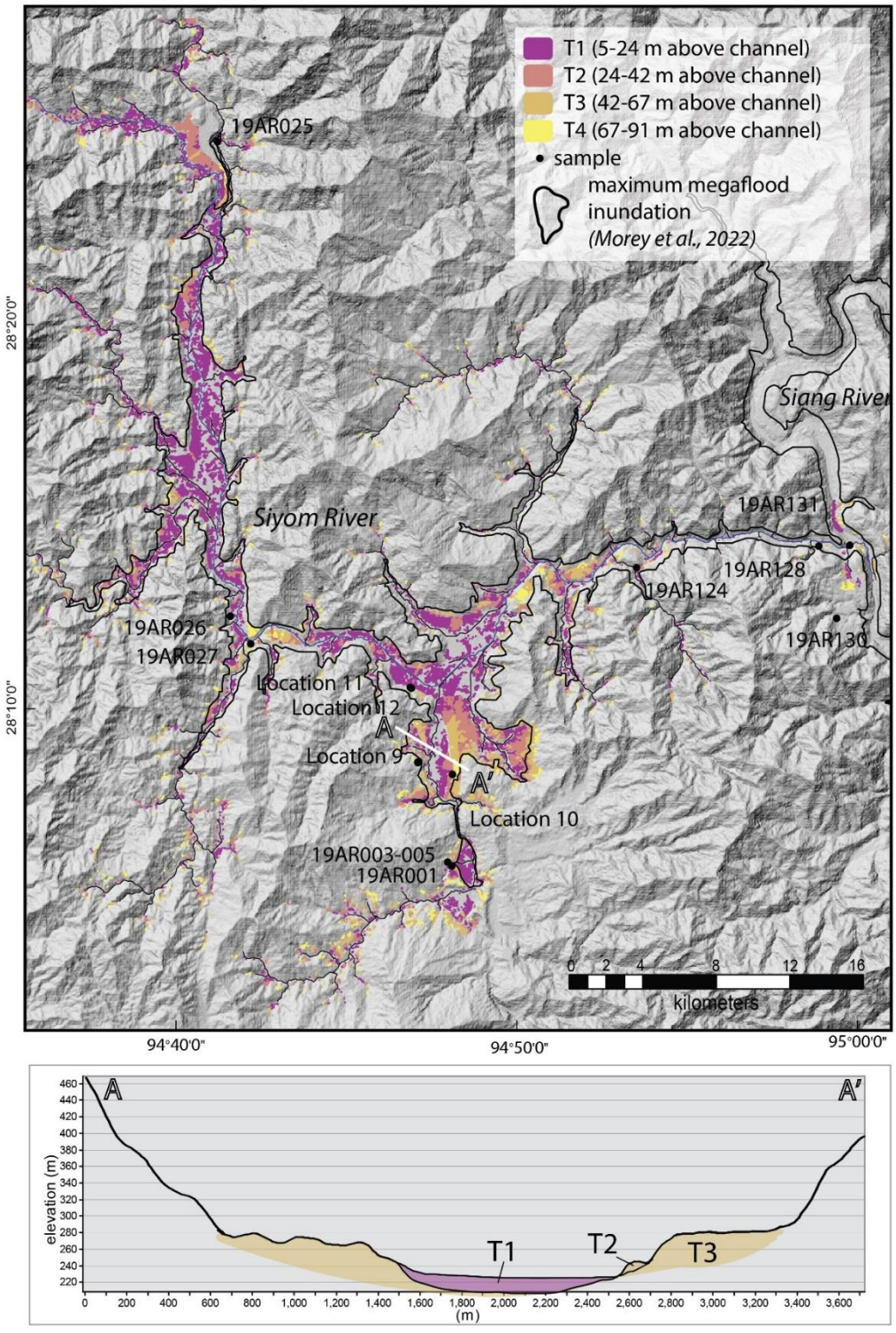

Figure 2.5. Mapped extents of the four terraces identified in this study.

2.4.2 *Deposit sedimentology and stratigraphy*

We define seven sedimentary facies observed in terrace deposits in the Siyom River valley. Facies are described in **Table 2.1** and illustrated in stratigraphic columns in **Figure 2.3.** Stratigraphic columns from Locations 11 and 12. Photographs of these faces can be found in Appendix B. These facies include: Facies A, a cross-bedded medium to fine sand; Facies B, a matrix supported conglomerate; Facies C, a structureless sand; Facies D: laminated silt, sand, and gravel; Facies E: structureless clay and silt; Facies F: laminated silt that grades up to structureless sand; and Facies G: a peat.

2.4.3 *Radiocarbon dating*

Of the four mapped terraces, we dated T2, T3, and T4. One of the samples yielded an erroneous date of >50,190 ^{14}C yrs BP, and the remaining 10 samples yielded dates ranging from 9,400-29,400 ^{14}C yrs BP (10,630-34,020 yr cal BP) (**Table 2.2**). T2 has 8 samples with ages that span the Holocene and Pleistocene, while T4 has a single Holocene age. Of the 8 T2 samples, 7 are from Locations 11 and 12. Two samples from the same black peat layer (Facies G) at Location 12 (19AR087 & 19AR107) yield consistent age ranges (2σ) of 10,560-10,710 cal yr BP and 10,660-10,820 cal yr BP (**Table 2.2; Figure 2.5**). Below the peat is a gray clay (Facies E) that was sampled 3 times (19AR088, 19AR089, and 19AR108) for radiocarbon, yielding more variable ages (2σ) of 10,870-10,960 cal yr BP, 12,590-12,680 cal yr BP, and 11,600-11,830 cal yr BP (**Table 2.2; Figure 2.3**). The remaining two samples from these locations come from a white clay and a blue-gray clay both from Facies E that are stratigraphically beneath the peat and gray clay samples (19AR047 and 19AR056). These two samples have age ranges (2σ) of 15,100-15390 cal yr BP and 12,910-13090 cal yr BP, respectively (**Table 2.2; Figure 2.3**). The last sample from T2 (19AR024; **Figure 2.3**) is a sand sampled from Facies A at the base of Location 11 with an age range (2σ) of 17,100-17,410 cal yr BP (**Table 2.2**). The sandy silt sample from T4 (19AR007) has an age range of 10,560-10,740 cal yr BP. T3 contains two samples (19AR021 and 19AR022) dated using radiocarbon: both from similar sandy silts which are above >50 m of imbricated boulder conglomerates. These samples yield age ranges of 18,670-18,820 cal yr BP and 24,050-24,510 cal yr BP (**Table 2.2**). The remaining valid radiocarbon sample within the Siyom River Valley is in an isolated terrace surface south of Aalo(ng) and has an age range of 33,280-34,290 cal yr BP

(19AR005). The sample that returned the >50 ka age (12AR004) is from this location as well. The radiocarbon samples from the lower terraces of Montomery et al. (2004) have recalibrated age ranges (2σ) of 1,010-1,020 cal yr BP and 1050-1,280 cal yr BP, while the upper terraces have recalibrated age ranges (2σ) of 9,760-10,180 cal yr BP and 11,190-11,410 cal yr BP (**Table 2.2**)

2.4.4 *Detrital zircon geochronology*

All three samples processed have primary detrital zircon age components between 420-630 Ma and 740-840 Ma (**Figure 2.4**). Approximately 56% of zircon ages from the modern Siyom River sample (19AR025, n = 158) are between 420-630 Ma and 18% are between 740-840 Ma. Most of the remaining ages are >1 Ga, with no significant age components, and only 5 ages are less than 100 Ma (with U/Th ratios between 18-194 (Appendix B)). In 19AR041 (n=156), ~35% of ages are between 420-630 Ma and ~28% are between 740-840 Ma. 3 ages are less than 100 Ma (U/Th ratios of 16-569) and most of the remaining ages are >1 Ga with no significant age component. In 19AR109 (n = 155), ~43% of ages are between 420 Ma and 12% are between 740-840 Ma. 6 ages are less than 100 Ma (U/Th ratios of 23-166) and, like the other two samples, most of the remaining ages are >1 Ga with no significant age components.

2.5 Depositional environments of sedimentary facies in the Siyom River valley

In this section, we discuss the different sedimentary facies and their potential depositional environments given their grain size, sedimentary structures, and stratigraphic relationships. The sediment in fill terraces of the Siyom River valley suggests that at least three different depositional environments controlled aggradation and re-incision at different elevations in the valley: fluvial, deep stagnant water, and deep, turbulent water.

We interpret faces A and B to reflect fluvial deposition in a braided river system. Facies A represents the deposition of suspended load from the fluvial channel, while the cobbles present in Facies B are a channel lag deposit from the active channel that represent the grain sizes moving as bedload in the river (**Table 2.1**). The modern Siyom River channel has both grain sizes present **(**Figure C11). Both facies are present in T2 at Locations 11 and 12, while only the channel lag deposit is present in T3 at Location 10. The deposits at Locations 11 and 12 are likely from the

ancient Siyom River, while those at Location 10 might represent bedload of the adjacent Siyom River tributary (**Figure 2.3**).

We interpret facies E and G to reflect the deposition of fine-grained suspended sediment in stagnant water. The apparently structureless silts and clays from Facies E represent deposition of fine particles from suspension in units with varying degrees of organic material. The variable color of the silts in this valley indicates variations in the relative abundance of organic material, with both mostly reduced units (gray, blue-gray, and white silts/clays) and oxidized units present (orange silts/clays). The faintly laminated, oxidized sandy silt at the base of the blue-gray clay could record a transition from a higher energy environment to the stagnant water required to deposit the structureless blue-gray clay. The irregular, unconformable base of the blue-gray clay in Facies E indicates an episode of erosion before the deposition of this structureless clay. We interpret facies G, a 50 cm thick peat layer to reflect deposition of coarse organic material in stagnant water. Similar black peat and blue-gray clay sequences are also apparent in the agricultural land of T1.

We interpret Facies C to represent slackwater deposition during megaflood events. The lack of sedimentary structures and poor sorting of Facies C combined with the thickness (>1 m) suggests rapid settling from a deep turbulent flow. We interpret them to be deposits from a sediment-laden flow that experienced a sudden decrease in energy, similar to deposits interpreted to be megaflood deposits found along the mainstem of the Siang River (e.g., Lang et al., 2013; Turzewski et al., 2020; Panda et al., 2020; Borgohain et al., 2020). In megafloods, massive flood sands are deposited in hydraulically sheltered areas where water has significantly lower energy than the main flood channel (e.g., Lang et al., 2013; Turzewski et al. 2020). Flows that experience this rapid decrease in energy can also produce weakly structured sand, like that observed at the base of Facies C. If megafloods inundated a tributary, we would expect to see similarly deposited structureless sand, as observed in other tributaries of megafloods.

Facies F also potentially represents a flood deposit that transitions from laminated fine-grained silts to coarser structureless sand. If this sediment were part of a typical overbank floodplain deposit, we would expect to see alternating clay, silt and sand as a part of the sequence along with paleosols and unconformities (e.g. Williams and Rust, 1969; Gurnell et al., 2008; Thayer and Ashmore, 2016). Instead, we observe silt that gradually grades up to sand, representing a change in the energy of the flow during deposition (Figure 2.10). Benito et al., (2003) identified

convoluted bedding as a result to channel widening sequences during an outburst flood. Because the laminations in Facies F are not strictly parallel to each other and instead are wavy (Figure C9), we interpret the bedded silt to represent some slight changes in flow direction in a low energy area of a flood, possibly silt that has settled over some planar surface in low energy periods of a flood (e.g., Zwoliński, 1992; Stewart et al., 2020; Benito et al., 2003). This facies grades up into a more massive sandy unit, similar to that of Facies C, but finer grained. The thickness of the unit combined with the slow transition from silt to sand suggests a gradual change in energy during deposition. We interpret facies F to reflect at least two different stages of backflood inundation. The laminated silt at the base was deposited on the peripheries of the valley during the beginning of backflooding, when shear stresses were variable and low. As the valley continued to be inundated in the rising stage of the floodwaters, we would expect the grain size to increase, which it does. Because Location 11 and 12 are located on the peripheries of the valley, it is likely that the structureless sand at the top of facies F represents slackwater deposition, like what is observed along the Siang River and associated with slackwater deposition along the main flood pathway.

Facies D has a less clear depositional environment interpretation, as it has sequences of coarsening upwards silts to sands and gravels (Figure C7). This facies always occurs directly underneath the clay and silt layers of Facies F. While this unit could record a short spatial scale fluvial increase in energy, it could also be related to complex backflooding hydraulics. The observed changes in grain size and soft sediment deformation look similar to Missoula Flood slackwater beds observed by Smith (1993) and Waitt (1984). The irregular, unconformable contact at the base of this facies leads us to interpret this sediment as some type of flow event that eroded the previously deposited fluvial sands of Facies A (Figure B7). A flood that mobilized a wide range of multiple grain sizes could produce density flows that erode fluvial sands and deposit sequences of sediment like those observed in Facies D (Carling, 2013).

The above interpretations lead to the following interpreted history of changing depositional environments in the Siyom River valley. (1) The Siyom River deposited typical fluvial sands and cobbles (Facies A and B); (2) Those processes either continued or a density flow triggered by rising flood waters was deposited (Facies D); (3) Parts of the valley experienced deep, stagnant water in which fine sediment rapidly accumulated (Faces E and G); (4) A flood with deep, turbulent flow inundated the valley and deposited laminated silts (Facies F) and structureless sand (Facies C); (5) Eventually, the valley returned to typical fluvial processes.

2.6 DISCUSSION

The sedimentary deposits of the Siyom River valley tell a rich story of aggradation along an anomalously low relief tributary of the Siang River, including sediment deposited by megaflood backflooding. We consider the observations of these deposits at the outcrop to reach scale in the context of the mapped terraces, geochronology, and sedimentary provenance constraints. We identify deposits that reflect deposition of silt and clay from deep, stagnant water and others that record rapid deposition of silt and sand out of suspension—both of which represent depositional environments not found in the modern Siyom River valley. We argue that these deposits record the varied hydraulics this tributary experienced during at least two phases of megaflood backflooding in the early Holocene and late Pleistocene.

2.6.1 *Depositional history of Quaternary deposits in the Siyom River valley*

We contextualize the observed terrace deposits within the Siyom River valley using radiocarbon geochronology and U-Th-Pb zircon dating constraints on provenance. This history does not require tectonic damming by active faults, identified by Misra and Srivastava (2009) but missing in more recent mapping (Hooker, 2022). Instead, our interpretation invokes repeated inundation by backflowing flood waters. Because the bulk of our observations are on T1, T2, and T3, we focus on those terraces. T4 is a bedrock terrace that is only on the highest elevations and is rare within the predicted maximum inundation levels of the simulated megaflood (**Figure 2.5**). Radiocarbon ages from peats are the most reliable of the samples analyzed and reflect a maximum-limiting age (e.g., Piotrowska et al., 2011). All samples from silt, sand, or silt/sand should be considered maximum ages owing to a significant fraction of recycled "old" carbon (Fowler et al., 1986; Nelson et al., 1988; Sharma et al., 2022).

The oldest fill terrace in the valley is T3 (42-67 m), which is widespread throughout the valley (**Figure 2.5**) both above and below the maximum simulated megaflood inundation level. Outcrops south of Aalo(ng) contain Facies B topped by a sandy silt (interpreted to be a soil profile) with Pleistocene age ranges (18,670-18,820 cal yr BP and 24,050-24,510 cal yr BP; **Table 2.2**). The two detrital zircon samples from this terrace are still being processed, but with this age and the relative relationship to the cobbles, we interpret T3 to be a fill terrace that records typical braided fluvial processes between 18.6 and 24.5 ka.

We interpret T2 to be an inset early Holocene-late Pleistocene fill terrace that was generated by sequences of fluvial processes and megaflood backflooding. When comparing the age of the black peat from Facies G (10,660-10,820 cal yr BP) and the gray clay directly below it from Facies E (11,497-11,559 cal yrs BP) to those of known paleolakes associated with megafloods on the Tibetan Plateau, it is close to the age reported from the high paleolake terraces mapped by Montgomery et al. (2004) (9,760-10,180 cal yr BP and 11,190-11,410 cal yr BP). These terraces correspond to an ancient glacial moraine dam at Namche Barwa 680 m above the elevation of the modern riverbed and a paleolake volume of 835 km^3. Morey et al. (2022) simulated the resulting flood from the breach of the smaller paleolake (81 km^3) reconstructed using the lower terrace elevation, but they suggested that larger lakes likely inundate at least the same topographic extent downstream, probably more. This similarity in dates supports our interpretation that the sequence of Faces E and G records deep, stagnant water produced by megaflood backflooding in the Siyom River Valley.

The repeated occurrence of Facies E suggests that the Siyom River valley experienced widespread inundation by deep, stagnant water at least four times since the late Pleistocene. We observe at least 3 layers of clay/silt (Facies E) of various thicknesses that were deposited from stagnant water and preserved within T2 with distinct (2σ) dates of 11,497-11,559 cal yrs BP, 12,910-13,088 cal yrs BP, and 15,099-15,392 cal year s BP (**Table 2.1; Figure 2.3**). Additionally, there are at least 2 distinct deposits that record sedimentation from deep, turbulent water that resulted in the rapid deposition of silt and sand (Facies C and F; **Figure 2.3**). Adjacent to the modern Siyom channel, T1 likely represents the 100-500 year floodplain throughout the Holocene that has also experienced megaflood backflow inundations. The relative elevation compared to the modern river suggests that modern extreme meteoric flooding likely inundates this terrace. While there are no radiocarbon dates from this terrace, parts of the bars within the channel are densely vegetated, suggesting stability. It is notable that we observe a blue-gray clay topped by a peat (Facies E & G, respectively) in the agricultural land of T1. The presence of this sequence indicates that megaflood backflooding processes that deposited Facies E and G happened again during the deposition of T1.

2.6.2 *Provenance of Siyom River valley sediment*

Other Himalayan rivers adjacent to the Siyom River valley (i.e., the Subansiri and Kameng Rivers) drain GHS and LHS bedrock and have detrital zircon age components between 400-600 Ma and ~800 Ma, respectively (**Figure 2.4b**; Cina et al., 2009; Gehrels et al., 2011). Because the Siyom River accesses the same bedrock, we would expect modern detrital zircon age components similar to those of the Subansiri and Kameng Rivers (i.e., 400-600 Ma and ~800 Ma). Notably, these headwaters do not erode <300 Ma Tibetan aged bedrock, like the main stem of the YSR does (Lang et al., 2014). Megaflood deposits identified along the Siang River have distinct mixed Tibetan and Himalayan provenance (Lang et al., 2013; Turzewski et al., 2020), with characteristic peaks at ~50 Ma and ~490 Ma, respectively (**Figure 2.4**). We might expect megaflood slackwater backflooding deposits in the Siyom River valley to have similar Tibetan and Himalayan age components.

Detrital zircon U-Th-Pb geochronology indicates that the modern Siyom sample and our two samples from T2 have detrital zircon age components that match GHS and LHS sources, but notably lack <300 Ma Tibetan age components. As expected, the modern Siyom sample (19AR025) has age components between 450-650 Ma and 750-850 Ma—the same age components present in the adjacent Subansiri and Kameng drainages (**Figure 2.4**; Cina et al., 2009). The fluvial sand deposit sampled from the lowest section of Location 11 in T2 (19AR041) has age components that match our modern Siyom River sands (**Figure 2.4**). This result suggests that the modern Siyom erodes the same sources as the paleo-Siyom did >15 ka. The megaflood-interpreted structureless sand deposit sampled from Location 12 in T2 (19AR109) has the same age components as the other two new samples from this study. This result suggests that megaflood backflooding remobilized and re-deposited sediment that was already within the Siyom River valley. We do not observe any significant age components <300 Ma, which suggests that there is no evidence for Tibetan sourced sediments present in T2. However, the few ages that are <100 Ma have high U/Th ratios (**Table B1**), which might suggest the presence of anatectic zircons (Hoskin and Schaltegger, 2003) which likely form from intrusive rocks—either within the GHS (Clarke et al., 2016) or from the Namche Barwa massif (Booth et al., 2004; Lang et al., 2013).

2.6.3 *Mechanisms for impoundment of the Siyom River valley*

A previous study interpreted the clay and peat layers in T2 as lacustrine deposits created by tectonic damming by active faults that cross the Siyom River Valley downstream of Aalo(ng) and the sand present in multiple terraces is attributed to alluvial deposition (Misra and Srivastava, 2009). Further investigation of tectonic structures in this valley does not identify active structures that cross the Siyom River in the location required to impound the river and create lacustrine deposits (Salvi et al., 2021; Hooker, 2022). The entire Siyom River Valley seems to have experienced the same relative local uplift for the last several million years associated with the Siang Antiform (Salvi et al., 2021).

Alternatively, a large landslide could have temporarily dammed the Siyom River and caused widespread fine-grained deposition. Given the low-relief morphology of the Siyom River valley near Aalo(ng), we might explain the deep, stagnant water deposits in T2 and T1 by repeated temporary landslide dams. Other locations in the eastern Himalaya which experience repeated landslide damming, like the Yigong River on the Tibetan Plateau, have visible scars in the landscape from the repeated immense mass-movement required to create a stable dam (e.g., Shang et al., 2003; Delaney and Evans, 2015). The landslide required to deposit T2 would need to be at least 42 m in height, likely higher in order to achieve the deep, stagnant water required to emplace the observed deposits. In the location required to create the topography observed we see no landslide scars and no evidence for ancient landslide dams. Additionally, there is no history of immense landsliding in the Siyom drainage since before 1974 (Larsen and Montgomery, 2012)—which we would expect given the repetition of Facies E and G that we observe in T2 and T1. Neither the proposed location of the fault which could have tectonically dammed the Siyom nor the location of a landslide dam required to deposit the clay and peat of Facies E and G, can explain the presence of T1 deposits on tributaries in the downstream bedrock gorge part of the Siyom River (i.e., sample 19AR124; **Figure 2.5**).

We interpret the sedimentary evidence in the Siyom river valley to record inundation and damming by backflow sedimentation of Quaternary megafloods, rather than alternative methods for impounding this YSR tributary. Carling et al. (2009) discuss evidence of backflooding by the Altai floods and provide a reasonable mechanism for tributary damming during megaflooding: pulsed deposition of gravels at tributary mouths. Previous hydraulic modeling results in **Figure 1.4** show that when backflowing megaflood waters enter the valley near Aalo(ng) (where the valley

widens), the flow spreads out and we observe decreases in shear stresses. This spatial gradient of shear stress could lead to widespread deposition of sediment that was previously in suspension (Morey et al., 2022). If the megaflood waters were carrying gravel and cobble sized sediment (as simulated shear stresses suggest), then this sediment would be deposited at the location of the shear stress gradient. The hydraulics during this inundation would be complex—Siyom river waters would have to compete both with the megaflood waters and the sediment deposited by it. Inundation of tributaries during megaflooding elsewhere has led to density flow deposition that has reverse grading (i.e., coarsening upwards) sandwiched between thick, structureless clays (e.g., Atwater, 1986). If the river cannot compete with the floodwater and sediment, it would begin to pool, potentially creating impoundments of various sizes. This could explain the erosional base and the repeated coarsening upwards sequences we observe in Facies D at Location 11 and Location 12 (**Figure 2.3**) and the immediate transition to the massive blue-gray clay of Facies E. Simulations predict floodwaters up to 110m deep (Figure 1.4; Morey et al., 2022), deep enough water to deposit thick structureless clays and silts. This impoundment method could provide sufficiently deep water that transitions dynamically from stagnant and turbulent flow depending on the timing of inundation. This impoundment method does not require the entire valley to be blocked and could explain the deposits on tributaries downstream of Aalo(ng) like 19AR124 (**Figure 2.5**). Because of this, we hypothesize that at least three megafloods inundated the Siyom and temporarily dammed it with rapid sedimentation.

2.7 CONCLUSIONS

We compared predictions of megaflood backflow inundation in the Siyom River valley (Morey et al., 2022) to the sedimentary record. We find evidence for deep, stagnant water within the valley and at least two different types of deposits that require deep, turbulent water. We invoke megaflood backflooding as the mechanism for the deposition of both the fine-grained clay and silt deposits and the structureless sand observed throughout mapped terraces (T2 and T1). We outline our sedimentary observations and include radiocarbon dates of peat and clay layers that suggest concurrent timing of deposition with paleolakes on the Tibetan Plateau that are hypothesized as the sources for megafloods that coursed down the Yarlung-Siang River during the Quaternary Period. Detrital zircon results for Siyom River valley deposits suggest that the river is accessing both GHS and LHS sediment, which could be from the Siyom River catchment or from the main

stem of the YSR. We contemplated alternative depositional hypotheses for the deposition of the fine-grained sediment observed in T1 and T2 and found a lack of evidence for both tectonic damming and landslide damming within the Siyom River valley. Instead, we propose that the Siyom River was temporarily impounded by megaflood sediment during backflooding inundation. The observed deposits in T2 and T1 fall within the predicted maximum inundation extent of the simulated megaflood, and the grain sizes and sedimentary characteristics of the observed facies in these terraces can be explained by the shear stresses observed in megaflood simulations (Morey et al., 2022). We therefore interpret that T2 records deposition during megaflood backflooding and hypothesize that other terraces within the Siyom River valley might record a rich history of other instances of backflooding inundation. Investigation of other megaflood backflow deposits in different regions of the valley could reveal more detail about the diverse types of deposits that megafloods cause when they inundate tributaries. Future analysis of these fluvial terrace deposits and correlation with detailed 3D hydraulic simulations could lead to a better understanding of megaflood backflooding processes and reveal much about eastern Himalayan megaflood magnitudes, frequencies, and sources.

3. **CHAPTER 3**: The lasting legacy of megaflood boulder deposition in mountain rivers

Submitted as: Morey, S. M., Shobe, C. M., Huntington, K. W., Lang, K. A., Johnson, A. G., Duvall, A. R. *The lasting legacy of megaflood boulder deposition in mountain rivers*. Geophysical Research Letters, June 2023 (in review).

Infrequent, large-magnitude discharge events known as megafloods can play a major role in landscape evolution. Prehistoric glacial-lake outburst megafloods transported and deposited large boulder (≥4m), yet few studies consider their potential lasting impact on river processes and form. We use a numerical model, constrained by observed boulder size distributions, to investigate the fluvial response to boulder deposition by megaflooding in the Yarlung-Siang River, eastern Himalaya. Results show that boulder deposition changes local channel steepness (k_{sn}) up to ~180% compared to simulations without boulder bars, introducing hundreds of meter-scale knickpoints to the channel that can be sustained for >20 kyr. Simulations further demonstrate that deposition of boulders in a single megaflood has a greater influence on k_{sn} than continuous deposition of boulders from hillslopes—an effect that compounds with multiple floods. Thus, in addition to extreme erosion, megafloods leave a lasting legacy of channel disequilibrium through widespread boulder deposition.

3.1 INTRODUCTION

High-magnitude, low-frequency geomorphic events, such as large floods, debris flows or landslides, perturb landscapes—potentially introducing long lasting disquilibrium to systems. For instance, megafloods (>10^6 m^3/s) sourced from the failure of dammed lakes have been shown to dramatically alter the topography they inundate, enough so that they have remained a topic of geomorphic research for more than a century (Baker and Milton, 1974; Bretz, 1925; Gilbert, 1890; O'Connor et al., 2013). Quantifying the amount, rate, and mechansims of erosion has been a primary focus of megaflood research (Baker and Kale, 1998; Lang et al., 2013; Larsen and Lamb, 2016). However, megafloods and other high discharge outburst floods can also transport and deposit an immense volume of sediment, including meter-scale boulders. In steep mountain landscapes, fine sediment can be relatively quickly evacuated (e.g., Hodge et al., 2011; Nelson and Dube, 2016), but the introduction of meter-scale boulders into mountain river channels may inhibit

erosion by altering the hydraulic roughness, flow velocity, and erosional power, as well as provide a mechanism for bed armoring (Sklar and Dietrich, 2004; Schneider et al., 2015; Shobe et al., 2016; Cook et al., 2018; Shobe et al., 2021). These findings suggest a potential long-term impact from widespread deposition of large boulders during a megaflood. In contrast to studies of megaflood erosion, the impact of boulder deposition on post-flood mountain river channel evolution is poorly understood.

The Yarlung-Siang River (YSR) in the eastern Himalaya (**Figure 3.1**) provides an excellent case study to examine the impact of megaflood- or event-deposited boulders because of its history of extreme floods and high concentrations of related large boulders in the channel. The YSR frequently experiences landslide lake outburst floods (LLOFs) with peak discharges between 10^4 and 10^5 m^3/s. There have been at least 10 LLOFs between 1950 and 2018 (Chen et al. 2020), including one of the largest historical outburst floods, the Yigong Flood in 2000 (discharge 1.2 x 10^5 m^3/s; Delaney and Evans, 2015; Turzewski et al., 2019). The Yigong River has been dammed by landslides at least 8 times in the same location over the last 6 kyr (Guo et al., 2020). Additionally, the YSR has experienced much larger outburst floods in the late Pleistocene and early Holocene. Estimates from paleolake deposits on the Tibetan Plateau (Montgomery et al., 2004; Song et al., 2013; Liu et al., 2015; Xu et al., 2020), moraine dams on the Tibetan Plateau at the Namche Barwa massif (**Figure 3.1**; Montgomery et al., 2004), and slackwater flood deposits downstream of the dams (Lang et al., 2013; Srivastava and Misra, 2012; Borgohain et al., 2020; Panda et al., 2020; Turzewski et al., 2020) indicate multiple megafloods originated from glacially impounded lakes at or upstream of the Namche Barwa massif drained through the YSR in the early Holocene and Pleistocene.

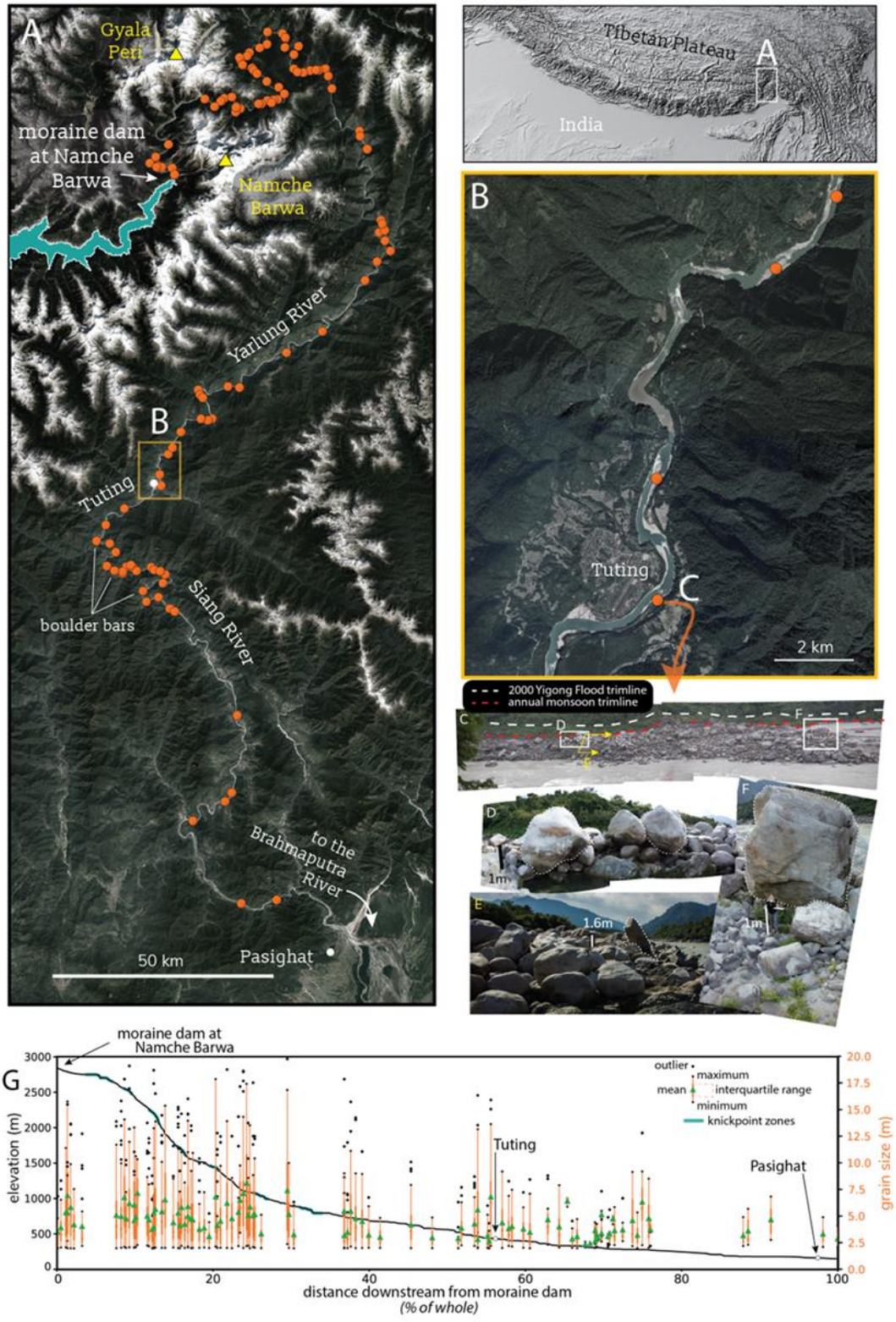

Figure 3.1. Regional map of the Yarlung-Siang River.

a) Regional map of the Yarlung-Siang River (YSR) between observed megaflood dams at Namche Barwa and where the YSR exits the range to join the Brahmaputra River at Pasighat. Orange dots represent observed boulder bars **b)** Tuting area **c)** a boulder bar at Tuting from (b) **d, e, & f)** boulders on the bar from (c) **g)** The longitudinal profile of the YSR with the grain size distribution of boulder measurements that are ≥2m at each observed boulder bar. Green triangles represent the mean boulder size at each bar.

Previous numerical flood modeling of outburst floods in the eastern Himalaya suggest interactions between the valley morphology and flood hydraulics result in depositional patterns unique to this type of flooding. Two-dimensional hydraulic modeling of (1) a historic 3 km^3 LLOF outburst flood (Turzewski et al., 2019) and (2) an ancient 81 km^3 lake outburst megaflood (Morey et al., 2022) on the YSR indicates that the high relief valley topography above the modern river channel in this landscape exerts a primary control on flood hydraulics. This causes the spatial distribution of flood deposits to differ dramatically from deposits by meteoric floods. Specifically, the boulder deposits documented in the YSR are located in unexpected locations (i.e., cut banks of meander bends) and have grain sizes too big to be moved by annual meteoric floods or even the largest historical outburst floods (Turzewski et al., 2019; Morey et al., 2022). Boulders that are too large to be mobilized by meteoric or smaller discharge modern outburst floods are likely to remain where they are deposited until either the next megaflood or until the boulders can be winnowed away to smaller, transportable sizes (e.g., Huber et al., 2020; Shobe et al. 2021). The difference in spatial distribution and general immobility of megaflood deposited boulders indicates a potentially different long term (10^2-10^5 yr) legacy in mountain rivers than the stochastic input of boulders sourced from local hillslopes.

In this paper, we present results from a river evolution model that help us address questions about the geomorphic legacy of outsized megaflood boulder deposits on mountain bedrock river profile evolution. We hypothesize that large boulder bar deposition locally reduces erosion rates and steepens the bedrock river channel downstream. Informed by >10,000 boulder measurements on the YSR, we work with an existing landscape evolution model (Shobe et al., 2016; 2018) which was developed to simulate the impact of hillslope derived blocks on bedrock river reaches, expanding it to an entire river longitudinal profile. Because megafloods deposit boulders in locations related to high relief valley morphology, not modern river stream power (Morey et al., 2022), the spatial distribution of boulder bars will likely lead to widespread changes in erosion rate that cannot be achieved by smaller scale events that cause only local introduction of boulders to the channel. While we are inspired by the YSR in the eastern Himalaya, the results are general and applicable to any event that can lead to widespread deposition of large, immobile boulders.

3.2 METHODS

We modify a version of the 1D numerical model of Shobe et al. (2016, 2018), which calculates the erosion-inhibiting effects of immobile/infrequently mobile boulders along a river's longitudinal profile, to assess post-megaflood erosion dynamics in a modeled mountain river system scaled to the YSR. The model accounts for two key effects of immobile boulders in the channel: bed armoring that shields the bed from erosion, and hydraulic drag that reduces erosive stresses on the bed. Model runs are inspired by the YSR, so the model domain has been modified to encompass a 500 km stretch of the YSR longitudinal profile, with relationships among downstream distance, drainage area, and river width broadly reflective of the YSR (Appendix C for detailed methods).

3.2.1 *Initial and boundary conditions*

The initial condition is a steady-state river profile generated to roughly match the length and fluvial relief of the YSR between the moraine dam identified on the Tibetan Plateau by Montgomery et al. (2004) and where the YSR exits the mountains to join the Brahmaputra River at Pasighat in Arunachal Pradesh, India (**Figure 3.1**a) under a constant rock uplift rate of 0.001 m/yr (same order of magnitude as Finnegan et al., 2008). A concavity of 0.8 is calculated for the equilibrium channel profile and is used as the reference concavity for later calculations (Figure C1). River width increases as a power-law function of drainage area (e.g., Wohl and David, 2008); downstream width increases were constrained by width measurements we made from satellite imagery at the upstream and downstream ends of the study reach. Initial megaflood boulder size and spatial distributions are made from new remote measurements of boulder size distributions from 106 in-channel boulder bars interpreted to be associated with megaflood deposition (Turzewski et al., 2019; Morey et al., 2022), and informed by estimates of the critical Shields stress for boulder transport from prior hydraulic work (Morey et al., 2022). River discharge is modeled using an inverse gamma distribution with parameters appropriate to monsoon-influenced eastern Himalayan rivers (Scherler et al., 2017). We track bed elevation, channel steepness (k_{sn}), the number/size of boulders, and fraction of the bed covered by boulders at a grid spacing of 250 m along the river profile.

3.2.2 *Experimental Design*

We compare three different experiments to examine the influence of megaflood-deposited boulders on subsequent channel evolution. The first is a control run with no boulders (R1). The remaining two runs represent end members of frequency/magnitude relationships of boulder addition: R2 is a run with hillslope-derived boulders that represents regular boulder addition by stochastic landsliding and R3 is a run with megaflood-deposited boulders that represents a single depositional event, with locations controlled by megaflood hydraulics. All three scenarios were run over 20 kyr with timesteps of 1 year beginning from the equilibrium longitudinal profile described in 3.2.1. R1 involves no boulder delivery to the river by any mechanism and is used as a baseline for comparison with R2 and R3. R2 mimics the experimental set up from Shobe et al. (2016), in which hillslope-derived blocks of a set grain size (4 m) are delivered to the channel in proportion to the rate of river incision (their Figure 3B). R3 does not include hillslope-derived boulders but includes initiation of the model with boulders grouped together in bars, the locations of which are taken from remote observations of 106 megaflood boulder bars in the YSR (**Figure 3.1**).

Boulder deposit characteristics were determined using Google Earth. At each bar, roughly 100 locations were measured, including boulders greater than 2 m in diameter, bedrock, and smaller grain sizes like sand and gravel (Figure C2b). Error of Google Earth measurements, estimated by comparing measurements to structure from motion photogrammetry was found to be less than 6 cm for boulders over 2 m in diameter (see Appendix C for detailed methods; Figure C2, Table C1). After measuring the proportion of the channel that each bar covers, we scaled the number of boulders at each bar to the bar cover fraction using the measured grain size distribution (**Figure 3.1**g). Simulations of megaflood hydraulics indicate that megafloods can mobilize boulders at least 4 m in diameter throughout the flood pathway (Morey et al., 2022). We thus excluded boulders smaller than 4 m in R3 to increase computational efficiency. Including boulders smaller than 4 m had no effect on the patterns and minimal effect on the magnitude of river profile elevation change. We assess the impact of boulder deposition on the river's longitudinal profile through time by calculating the percent difference in profile-averaged k_{sn} for R2 and R3 relative to the same river experiencing no boulder delivery (R1). This value is calculated locally for each 250 m cell along the profile and then local values are averaged over the entire longitudinal profile to obtain an average local percent change in k_{sn}.

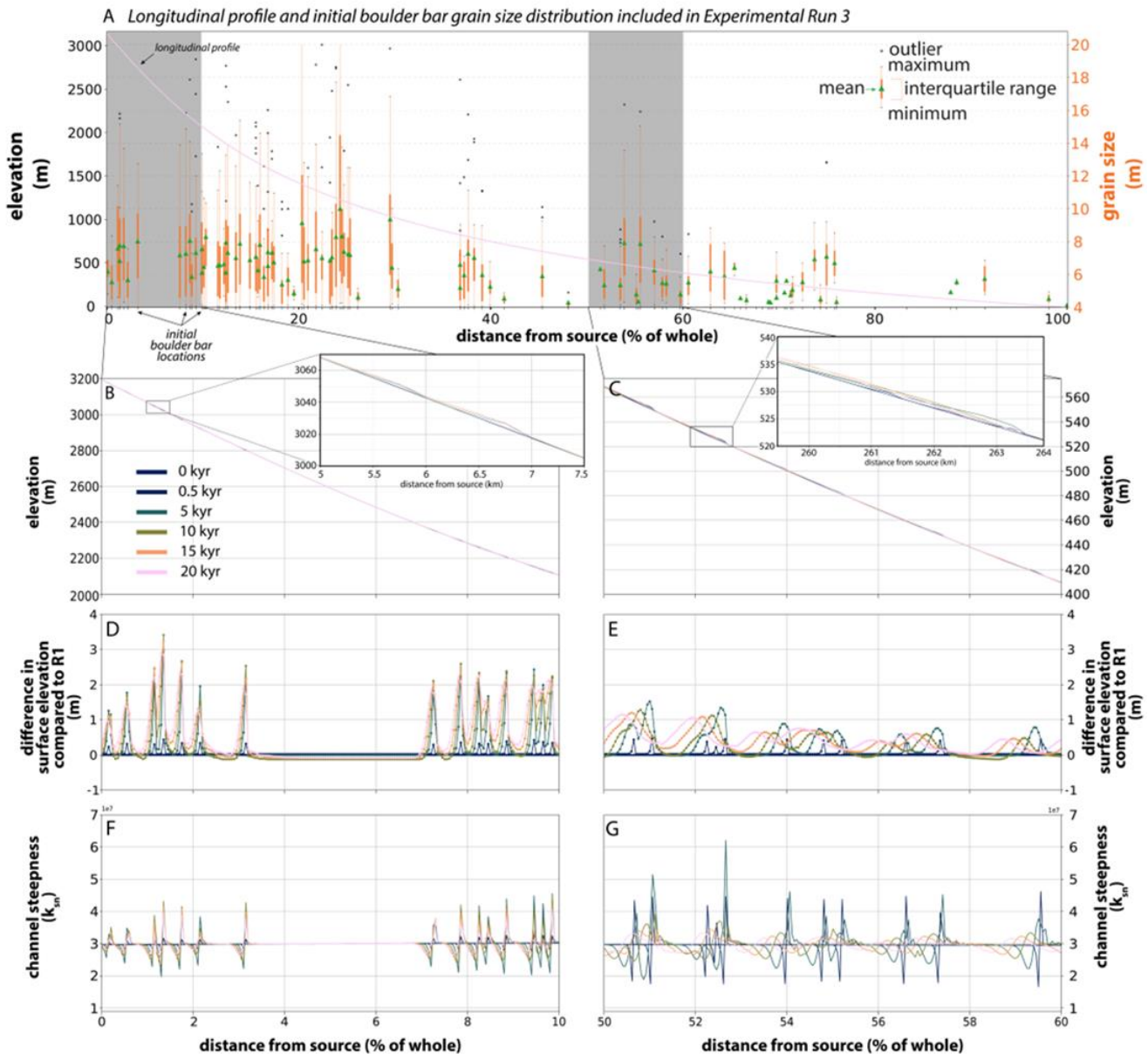

Figure 3.2. Model results.

a) Model results of the longitudinal profile plotted with distance downstream from source. The rest of the figure zooms into two sections: 0-10 % of the long profile (b, d, f) and 50-60% of the long profile (c, e, g). **b & c)** elevation (m) with insets that show horizontal distance **d & e)** elevation change in meters **f & g)** channel steepness (k_{sn}).

3.3 RESULTS

Boulders sourced from both hillslopes and megafloods reduce erosion rates where they are deposited, allowing rock uplift to outpace river incision. The scale of elevation change from megaflood boulders (R3) is an order of magnitude larger than that from hillslope-derived boulders

(R2). In R3, boulders cover a maximum of 44% of the channel bed at any given location along the longitudinal profile, which leads to up to 3.5 m of elevation change over the 20 kyr run (**Figure 3.2**). In R3, there are two predominant regimes of behavior: elevation change that remains centered on the original location of the boulder bar for long periods (**Figure 3.2**b, d, f) and elevation change that migrates upstream from the original boulder bar location (**Figure 3.2**a, c, e, g). The former results in increasing elevation for a longer period of time than the latter (11.5 kyr compared to 3.5 kyr for the examples in **Figure 3.2**). In R2, boulders cover < 0.3% of the channel bed at any given location and lead to < 0.5 m of elevation change. Further results from R2 can be found in the Appendix C Figure C3.

The addition of megaflood deposited boulder bars suppresses erosion at the initial location of each bar, which results in net channel-bed surface uplift at that location. We observe local, meter-scale changes in elevation that manifest as individual knickpoints at the reach scale but are not visible at the scale of the entire longitudinal profile with its 3,000 m of total fluvial relief. Bars tend to exert a zone of influence both up- and downstream of their initial locations that grows with time as the channel bed adjusts to the presence of boulders, an effect that can compound if there are multiple boulder bars near each other. For example, in a location with stationary boulder-induced elevation change due to the long timescales required for the channel to adjust to the boulder bar, peak elevation change is not reached until ~11 kyr.

If there is a boulder bar upstream of that location, with its own knickpoint, the two knickpoints will merge into one as the region of influence of each boulder bar spreads (**Figure 3.2**b,c). Then, by 20 kyr the perturbation migrates upstream, with the original location of the boulder bar losing elevation and the locations upstream of the bar continuing to gain elevation. The same process happens much more quickly in locations where the river can quickly adjust to the presence of the boulder bars. By 3-4 kyr, the original position of boulder bar deposit can begin to experience elevation loss (**Figure 3.2**b,c) as the knickpoint begins to migrate upstream and it becomes hard to distinguish between individual knickpoints if the bars were originally close together. By ~10 kyr, the boulder-induced knickpoints have been significantly reduced in magnitude and, by 20 kyr, the peak elevation change is no longer at the original bar location but has migrated up to a kilometer upstream. Whether post-deposition knickpoint behavior follows the regime of migrating or stationary boulder-induced elevation change depends on the river's ability to adjust to the influx of coarse sediment.

The largest boulders move downstream <500 m during each experiment and tend to first degrade to smaller sizes before they can be transported. As expected, the smaller the initial boulder size, the quicker subsequent transport happens. As boulders erode to grain sizes able to be transported by the imposed discharge distribution and move downstream, the area that experiences suppressed erosion rates spreads to downstream locations that now host boulders. This effect is enhanced when two boulder bars are close to each other. Boulder bars that retain the most megaflood deposited boulders are those that have boulder bars upstream of them. Winnowed boulders from the upstream bar are transported downstream but get "stuck" at the downstream bar: a boulder that could have been moved at that bar at the beginning of the run now requires more shear stress to move because that downstream bar has decreased the slope.

Boulder-induced changes in elevation lead to an increase in k_{sn} immediately downstream of the locus of boulder deposition and a decrease in k_{sn} immediately upstream (**Figure 3.3**f,g). We assess the impact of boulder deposition on the river's longitudinal profile through time by calculating the local percent change in k_{sn} compared to the baseline, no boulders run (R1). We then plot the average local percent change for the entire longitudinal profile for each time-step in Figure 3a. Megaflood boulders cause k_{sn} to change up to 174% with a maximum mean percent change of 6.8% compared to R1 (at 2.5 kyr; **Figure 3.3**). Hillslope-derived boulders only cause k_{sn} to change up to 30% with a mean percent change of 1.7% (**Figure 3.3**). Although the peak impact at every bar and location might not occur simultaneously, the average percent change allows us to make interpretations about the influence that wide-spread megaflood deposited boulder bars have on the whole river profile.

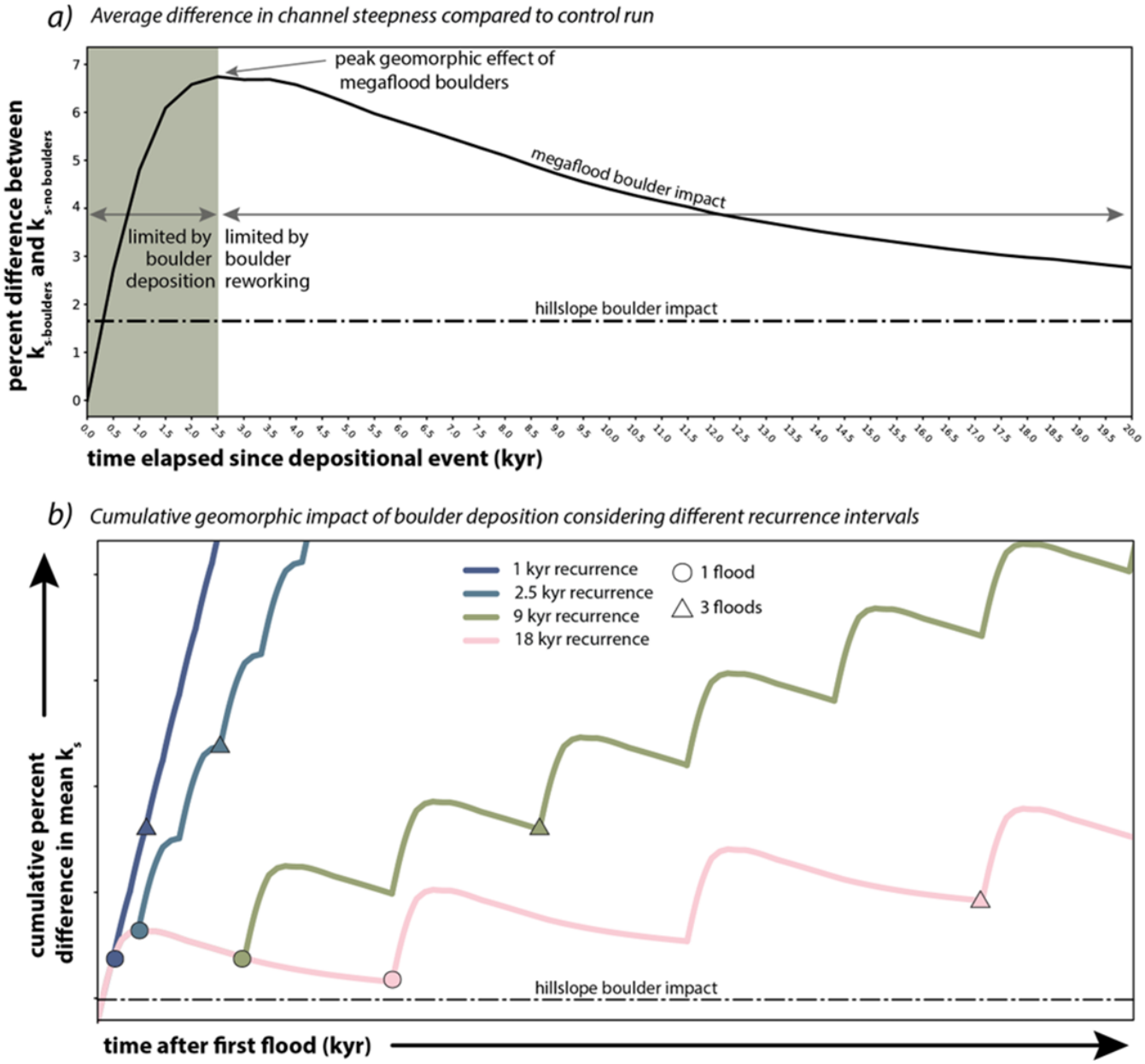

Figure 3.3. Average difference in local channel steepness.

a) Average local percent change in k_{sn} between R2 (dashed line) and R3 (solid line) with respect to the baseline at each time-step of the model run as a function of time elapsed after the megaflood depositional event. The highlighted green portion represents the time after a megaflood in which the average geomorphic response is limited by the initial size and spatial distribution of megaflood deposited boulders. The rest of the plot represents the time during which the geomorphic response is limited by the river's ability to rework the megaflood deposited boulders. **b)** Schematic of cumulative geomorphic impact due to the addition of megaflood boulders from sequences of many floods with 4 different recurrence intervals: 1 kyr, 2.5 kyr, 9 kyr, and 18 kyr. The dashed line is the same dashed line from A—the equilibrium effect of a landscape that experiences hillslope-derived boulder deposition. x- and y-axes are the same as in (a).

3.4 DISCUSSION

After a single megaflood, the river does not return to a smooth, concave-up equilibrium profile, even after 20,000 years. While this exact timescale and magnitude of change in k_{sn} is contingent on our choice of model parameters (e.g., bedrock erodibility), the shape of the curve is revealing. By 500 years, the megaflood boulder deposition has changed k_{sn} more than is possible in a channel with only hillslope-derived boulders (**Figure 3.3**a). Boulder bars along the simulated profile reach their peak impact on the river 2,500 years after deposition (time to peak boulder impact, t_{pbi}). Before t_{pbi}, the river's response to megaflood boulders is limited by the number and spatial distribution of megaflood-deposited boulders. After t_{pbi}, the river's response is limited by the ability of the river to abrade and rework the boulders and their descendants. After t_{pbi}, the average change in k_{sn} diminishes with time. k_{sn} is on average more changed in the simulated landscape that experiences megaflood boulder deposition compared to the one that only experiences hillslope-derived boulder deposition (**Figure 3.3**a).

The geomorphic effects of megaflood boulders compound with repeated megaflooding. During megafloods, existing coarse sediment in the landscape will tend to be reworked and re-organized into boulder bars. Because megaflood hydraulics in high-relief, confined river valleys are controlled by valley-scale topography (Morey et al., 2022), megafloods similar in magnitude will deposit sediment in similar positions in the landscape. We, therefore, argue that the depositional effects of multiple megafloods of similar magnitude should compound as coarse sediment deposition recurs in these valley-scale controlled locations. This compounding depositional effect is illustrated for different recurrence intervals in **Figure 3.3**b. If a flood has a recurrence interval shorter than t_{pbi} (2,500 years for our choice of model parameters), intense compounding effects of megaflood boulder deposition result in rapid change in average local k_{sn}. Compounding effects of boulder deposition from floods with recurrence intervals that are longer than t_{pbi} accrue at a slower rate (**Figure 3.3**b), but still outpace the effects of hillslope-derived boulders provided that the recurrence interval is shorter than the time it takes for all megaflood boulders to decay—a point not reached in our experiments (i.e., >20 kyr).

These results suggest that the modern YSR is still affected by the boulder deposition of the latest sequence of megafloods. Megaflood-deposited boulders have the potential to contribute to the many changes in channel steepness observed on the river's longitudinal profile (**Figure 3.1**g).

The knickpoints observed on the modern YSR (e.g., Korup and Montgomery, 2008; Wang et al., 2017) cannot be solely explained by the impact of megaflood boulders; however, these outsized grains can cause elevation change significant enough to create and sustain meter-scale knickpoints. There is broad consensus that at least 3-8 glacial lake sourced floods happened in the last 8-13 kyr (e.g. Montgomery et al., 2004; Song et al., 2013; Liu et al., 2015; Srivastava and Misra, 2012; Borgohain et al., 2020; Panda et al., 2020; Turzewski et al., 2020; Xu et al., 2020), with megaflood deposits identified as young as ~1 ka (Srivastava and Misra, 2012; Panda et al., 2020). This flood frequency combined with the prevalence of boulders throughout the river valley that are too large to be moved by modern flows (**Figure 3.1**) or by historical LLOFs (Turzewski et al., 2019) provide evidence that the YSR has either not exceeded t_{pbi} or exceeded it within the last couple of thousand years. This suggests that the YSR is still affected by the boulder deposition of the latest sequence of megafloods. Even if there had been no megafloods in the last 20 kyrs, we would expect to observe a landscape with a different average local channel steepness than one that did not experience megaflood deposition, regardless of whether or not there are boulders contributed by the hillslopes (**Figure 3.3**b).

Megafloods likely occurred in rapid succession following deglaciation, increasing the possibility that megaflood depositional effects persist for a significant amount of time without any subsequent megaflooding, enough to survive glacial/interglacial cycles barring any glacial erosion. Megafloods are not often thought to happen in isolation. Instead, many can occur in short intervals at the end of a glacial cycle due to the increasing instability of valley-crossing glaciers (e.g., Evans & Clague, 1994, 1997; O'Connor and Baker, 1992; Herget et al, 2020). Our results suggest that this effect could be felt for tens to hundreds of thousands of years afterwards, depending on the number of floods and the characteristics of the landscape (e.g., uplift/erosion rates, bedrock erodibility, etc.). The depositional effects of a series of megafloods could plausibly survive the 40-100 kyr interim between glacial and interglacial cycles (the length of glacial cycles pre- and post- Mid-Pleistocene Transition during the Quaternary, e.g. Shackleton and Opdyke, 1976; Berends et al., 2021), barring any overprinting by subsequent glacial processes. Bedrock river landscapes downstream of breached glacial dams may therefore retain vestiges of megaflood deposition from past glacial cycles.

While our study focuses on megaflooding, any event that can cause repeated, regionally synchronous deposition of ≥4m in diameter boulders (i.e., earthquake-triggered landslides,

seasonal flash flooding, etc., Dewey et al., 2021) could have similar long-term geomorphic impacts. For example, large earthquakes, like the 1950 Assam earthquake (e.g., Parkash, 2013; Devi and Bora, 2016), can trigger landslides that deposit boulders regionally in patterns unrelated to stream power. Instead, they are likely related to the magnitude of ground shaking (Nowicki Jessee et al., 2018) and the consequences of topographic amplification (Meunier et al., 2007; Rault et al., 2019; Dunham et al., 2022). Earthquakes that recur in similar locations in the landscape (i.e., on the same faults) could cause region-wide, repeated coarse deposition that, similar to the megafloods, produce compounding effects through time (**Figure 3.3**b). Repeated landslide dam breach events at the same location have also been shown to cause wide-spread changes in channel slope (Zhang et al., 2018; Lin et al., 2022). However, this change is tied to an event that impacts an individual location, creating a stable knickpoint at the location of the landslide with effects diffusing downstream. The coarse deposition that occurs during repeated megafloods and/or large earthquakes creates synoptic scale geomorphic changes that a repeated landslide dam cannot produce. We would expect similar geomorphic effects from any event that can cause repeated, synoptic scale deposition of ≥4m boulders within bedrock channels.

3.5 CONCLUSIONS

This study investigates the impact of large (≥4m), widespread boulder deposition on bedrock river process and form. Inspired by megaflooding and observations of widespread boulder bar deposits in the eastern Himalaya, we conduct model simulations that explore the geomorphic legacy of the depositional pattern of megaflood boulders. In the first scenario, no boulders are deposited, and in the second and third scenarios, boulders are deposited stochastically by hillslopes and in locations that reflect field observations of megaflood deposited boulders, respectively. The results show that the megaflood-deposited boulders have a greater impact on the river's longitudinal profile than hillslope-derived boulders, initiating hundreds of local, meter-scale knickpoints and causing up to 3.5 meters of elevation change throughout the profile. Elevation change is associated with locations where megaflood boulder bars are deposited, and post-deposition knickpoint behavior depends on the river's ability to adjust to the influx of coarse sediment. Instead of modern river hydraulics (i.e., stream power), megaflood boulder depositional patterns will be dictated by valley-scale topography (Morey et al., 2022). We show that the patterns of morphologic change produced by megaflood boulders are different from those driven by

hillslope-derived boulders. The deposition of boulders in bars during a single megaflood produces more change in channel steepness than do boulders supplied to the channel by background hillslope processes driven by bedrock incision. If megafloods happen in rapid succession, the impact from boulder bar deposition will compound after each flood. Our results suggest that the modern Yarlung-Siang River may still be experiencing the impacts of boulder bar deposition from the last sequence of megafloods and that it will continue to experience these effects for the next several thousand years, regardless of whether or not it experiences future megaflooding. Effects like this will happen after any events that can cause repeated, spatially extensive deposition of boulders too large to be mobilized by the modern river.

4. Dissertation Conclusions

The role of large-magnitude flood events in shaping planetary landscapes has intrigued geomorphologists for more than a century (Gilbert, 1980; Bretz, 1925; Baker and Milton, 1974). The largest of these floods are sourced from the failure of dammed lakes and may produce discharges several orders of magnitude higher than the annual hydrologic water discharge of a river system, even exceeding 10^6 m^3/s and entering the realm of "megafloods" (Baker, 2013). Despite being short lived, exceptional inundation and high shear stresses during a megaflood can cause profound landscape change with extreme fluxes of water and sediment extending up to thousands of kilometers from source to sink. Much of our understanding of megaflood hydraulics and their subsequent erosion and deposition comes from the study of megafloods in low relief systems (e.g., Denlinger and O'Connell, 2010; Lehnigk and Larsen, 2022). However, the eastern Himalayan syntaxis is one of the highest relief landscapes in the world and has regularly experienced outburst floods, including modern and historical landslide dam break outburst floods and Holocene megafloods sourced from Tibetan glacial lakes. While eastern Himalayan megafloods have been proposed as agents of massive geomorphic change along the Yarlung-Siang River (e.g., Montgomery et al, 2004; Lang et al., 2013; Borgohain et al., 2020), an exploration of interactions between this high relief landscape and the hydraulics of a megaflood has remained absent in the literature. In this dissertation, I have explored the processes and long-term legacy of megafloods in the high relief eastern Himalaya. I simulated the hydraulics of a megaflood and predicted the erosional patterns that result. I then considered megaflood deposition and the consequences that deposition has in this rapidly uplifting landscape.

I simulated eastern Himalayan megaflood hydraulics for the first time, which enabled a new intuition for megaflood erosional and depositional patterns in steep mountain landscapes (Morey et al., 2022). Previous studies used simple geometric calculations and stream power to predict discharge and erosional patterns of megafloods in this landscape. However, the high relief nature of the YSR river is likely the reason that those calculations under predicted discharge by a third and could not capture the patterns of bed shear stress produced in the 2D hydraulic simulations. If the $>10^3$ year erosional patterns of this region are dominated by megaflood erosion instead of typical annual erosional patterns (as debated by Lang et al., 2013; Yang et al., 2018; Borgohain et al., 2020; Turzewski et al., 2020 and many others), then using stream power as a

proxy for erosion in the eastern Himalaya will not yield correct estimations of erosional patterns. This has important implications for the interactions between surface processes and tectonics, including the debate concerning the validity of the tectonic aneurysm model in the eastern Himalayan syntaxis (e.g., Koons et al., 2013; Yang et al, 2018; Dong et al., 2023). The numerical simulations represent a significant step towards estimating the volume of bedrock erosion caused by a single eastern Himalayan megaflood. Future studies should combine field investigations of bedrock lithology, fracture patterns, and megaflood hydraulic simulations, with experimental or numerical studies of block plucking (e.g., Lamb et al., 2015; Gardner et al., 2023)

In addition to considering megaflood erosion, I discovered the widespread potential for deposition throughout the YSR flood pathway—an underappreciated legacy of eastern Himalayan megaflooding. Measuring the amount, rate, and mechanisms of erosion has been the primary focus of megaflood research in recent years (e.g., Lamb et al., 2008; Lang et al., 2013; Larsen and Lamb, 2016; Cook et al., 2018; Huber et al., 2020; Lehnigk and Larsen, 2022). However, megafloods can transport an enormous volume of sediment (Carling et al., 2013), and, as demonstrated in Chapters 2 and 3, deposition of megaflood sediment can have a profound impact on river channel processes and form. Simulations of megaflood hydraulics revealed the capacity for megafloods to transport and deposit (1) sand and silt along the peripheries of the main flood pathway and along inundated tributaries (Morey et al., *in prep*) and (2) decameter scale boulders within the modern YSR channel (Morey et al., *in review*).

In the Siyom River, a tributary predicted to be inundated during a simulated megaflood, I observe evidence for inundation by deep water, both stagnant and turbulent, which requires different depositional processes than observed in the modern tributary valley. While there are other possible mechanisms for temporarily impounding the Siyom River valley, I do not find evidence in the landscape for recently active faults that could tectonically dam the river or ancient landslide dams. Instead, I invoke megaflood backflooding as the cause of the deep water. This interpretation is supported, not only by the observed sedimentary characteristics within fill terraces, but also by radiocarbon dating of those deposits. The ages of peat and clay deposits coincide with the timing of paleolake formation on the Tibetan Plateau (e.g., Montgomery et al., 2004; Wang et al., 2023). This exploration of fill terrace deposits in the Siyom River valley provides the first evidence for extensive megaflood backflow on the YSR. It is likely that so long as the paleo-Siyom maintained its low slope, it was inundated every time a megaflood coursed down the YSR and, therefore,

megaflood deposition likely reinforced the low slope of this river valley. Further investigation of these deposits and others within inundated tributaries could shed light on megaflood backflooding depositional processes, which could enable better reconstructions of paleoflood magnitude, frequency and source.

While the discussion in Chapter 2 explains the depositional processes that happen during widespread megaflood backflooding, it does not explain the origin of the low relief Siyom River valley in the first place. The reason the Siyom River was likely inundated so extensively during megafloods is because of its anomalously low slope. Most, if not all, other tributaries of the YSR downstream of the Tibetan Plateau are bedrock rivers that have higher slopes than the adjacent YSR. The Siyom River, on the other hand, is a mixed bedrock alluvial river with a slope almost identical to that of the adjacent YSR. Parts of the river follow the Tuting Basar Strike-Slip Fault or cuts through the western limb of the Siang Window Antiform, running perpendicular to structures. Past deformation along these structures could be responsible for the original low slope of this region, but current literature (including our study) cannot provide answers yet. Future studies should look more closely at other fill terrace deposits, paying particular attention to contacts with bedrock.

In Chapter 3, I explored the geomorphic legacy of decameter-scale, megaflood-deposited boulders, showing how their deposition inhibits bedrock erosion throughout the flood pathway, creating hundreds of meter-scale knickpoints. Because megafloods do not happen in isolation, but rather occur in quick succession during a warming climate, the effects of these deposited boulders should compound. After a cycle of multiple megafloods, the river would potentially be changed so significantly that the knickpoints could persist for tens of thousands of years. While megaflood boulder deposition alone cannot explain the presence of the knickpoints apparent on the modern YSR (e.g., Korup and Montgomery, 2008), my dissertation shows that megaflood deposition alone can contribute to variable patterns of long-term ($> 10^3$ year) incision and uplift. While this depositional effect will happen after every megaflood in the eastern Himalaya, it does not have to be unique to megaflooding. Any process that can cause repeated, regionally synchronous deposition of ≥4 m diameter boulders could have similar geomorphic impacts. Mountain landscapes that do experience this type of widespread boulder deposition will evolve differently than either (1) a landscape that does not experience any boulder deposition or (2) a landscape that only experiences stochastic deposition of boulders. Chapter 3 shows that the depositional legacy

of megaflooding, while probably not as immediately apparent as megaflood erosion, is just as important. Further investigation of this legacy is necessary, like incorporating the effects of boulder deposition on channel width in landscape evolution models.

The investigations into the legacy of megaflooding in the eastern Himalayan in this dissertation have expanded our understanding of how these immense floods behave in and shape steep mountain landscapes. 2D numerical simulations give me insight into the dynamic interactions between the rugged topography and flood waters, while scrutiny of sedimentary deposits revealed details about megaflood backflooding depositional processes and a landscape evolution model explored the impact of megaflood-deposited boulders on long-term longitudinal river profile evolution. The implications discussed herein represent the continuation of a multidisciplinary, team-driven approach to studying the ways in which megafloods impact the landscape of the eastern Himalaya. These findings highlight the complex way in which megafloods shape this region—a significant advancement of our understanding of how outburst flood hydraulics affect high-relief landscapes.

REFERENCES

Acharyya, S. K., & Saha, P. (2008). Geological setting of the Siang Dome located at the Eastern Himalayan Syntaxis. *Him. J. Sci., Spec. Issue, extended abstr*, *5*, 16-17.

Atwater, B. F., Adam, D. P., Bradbury, J. P., Forester, R. M., Mark, R. K., Lettis, W. R., ... & Robinson, S. W. (1986). A fan dam for Tulare Lake, California, and implications for the Wisconsin glacial history of the Sierra Nevada. *Geological Society of America Bulletin*, 97(1), 97-109.

Baker, V. R. (2009). Channeled scabland morphology. *Megaflooding on Earth and Mars*, 65-77.

Baker, V. R. (2013). 9.26 Global Late Quaternary fluvial paleohydrology: With special emphasis on paleofloods and megafloods.

Baker, V. R., & Kale, V. S. (1998). The role of extreme floods in shaping bedrock channels. *Geophysical Monograph-American Geophysical Union*, *107*, 153-166.

Baker, V. R., & Milton, D. J. (1974). Erosion by catastrophic floods on Mars and Earth. Icarus, 23(1), 27-41.

Baker, V. R., Kochel, R. C., Patton, P. C., & Pickup, G. (1983). Palaeohydrologic analysis of Holocene flood slack-water sediments. *Modern and ancient fluvial systems*, 229-239.

Baynes, E. R. C., Attal, M., Niedermann, S., Kirstein, L. A., Dugmore, A. J., & Naylor, M. (2015). Erosion during extreme flood events dominates Holocene canyon evolution in northeast Iceland. *Proceedings of the National Academy of Sciences*, *112*(8), 2355–2360. https://doi.org/10.1073/pnas.1415443112

Benito, G. (1997). Energy Expenditure and Geomorphic Work of the Cataclysmic Missoula Flooding in the Columbia River GGorge, USA. Earth Surface Processes and Landforms: The Journal of the British Geomorphological Group, 22(5), 457-472.

Benito, G., & O'Connor, J. E. (2013). Quantitative Paleoflood Hydrology. In *Treatise on Geomorphology* (Vol. 9). https://doi.org/10.1016/B978-0-12-374739-6.00250-5

Benito, G., & Thorndycraft, V. R. (2020). Catastrophic glacial-lake outburst flooding of the Patagonian Ice Sheet. Earth-Science Reviews, 200(October 2019), 102996. https://doi.org/10.1016/j.earscirev.2019.102996

Benito, G., Sánchez-Moya, Y., & Sopeña, A. (2003). Sedimentology of high-stage flood deposits of the Tagus River, Central Spain. Sedimentary Geology, 157(1-2), 107-132.

Berends, C. J., Köhler, P., Lourens, L. J., & van de Wal, R. S. W. (2021). On the cause of the mid-Pleistocene transition.

Berger, M. J., George, D. L., LeVeque, R. J., & Mandli, K. T. (2011). The GeoClaw software for depth-averaged flows with adaptive refinement. *Advances in Water Resources*, *34*(9), 1195–1206.

Blum, M., Rogers, K., Gleason, J., Najman, Y., Cruz, J., & Fox, L. (2018). Allogenic and autogenic signals in the stratigraphic record of the deep-sea Bengal Fan. Scientific Reports, 8(1), 1-13.

Bohorquez, P., & Darby, S. E. (2008). The use of one- and two-dimensional hydraulic modelling to reconstruct a glacial outburst flood in a steep Alpine valley. *Journal of Hydrology*, *361*(3–4), 240–261. https://doi.org/10.1016/j.jhydrol.2008.07.043

Bohorquez, P., Carling, P. A., & Herget, J. (2016). Dynamic simulation of catastrophic late Pleistocene glacial-lake drainage, Altai Mountains, central Asia. *International Geology Review*, *58*(14), 1795–1817. https://doi.org/10.1080/00206814.2015.1046956

Booth, A. L., Zeitler, P. K., Kidd, W. S. F., Wooden, J., Liu, Y., Idleman, B., … Chamberlain, C. P. (2004). U-Pb zircon constraints on the tectonic evolution of southeastern Tibet, Namche Barwa area. *American Journal of Science*, *304*(10), 889–929. https://doi.org/10.2475/ajs.304.10.889

Borgohain, B., Mathew, G., Chauhan, N., Jain, V., & Singhvi, A. K. (2020). Evidence of episodically accelerated denudation on the Namche Barwa massif by megafloods. *Quaternary Science Reviews*, *245*, 106410. https://doi.org/10.1016/j.quascirev.2020.106410

Bretz, J. H. (1925). The Spokane flood beyond the channeled scablands. The Journal of Geology, 33(2), 97-115.

Bretz, J. H. (1929). Valley Deposits Immediately East of the Channeled Scabland of Washington. I. The Journal of Geology, 37(5), 393-427.

Burg, J. P., Nievergelt, P., Oberli, F., Seward, D., Davy, P., Maurin, J. C., Diao, Z., & Meier, M. (1998). The Namche Barwa syntaxis: Evidence for exhumation related to compressional crustal folding. *Journal of Asian Earth Sciences*, 16(2–3), 239–252. https://doi.org/10.1016/S0743-9547(98)00002-6

Burr, D. M., Carling, P. A., & Baker, V. R. (Eds.). (2009). *Megaflooding on Earth and Mars*. Cambridge University Press.

Burr, D. M., Grier, J. A., McEwen, A. S., & Keszthelyi, L. P. (2002). Repeated aqueous flooding from the cerberus fossae: Evidence for very recently extant, deep groundwater on Mars. *Icarus*, *159*(1), 53–73. https://doi.org/10.1006/icar.2002.6921

Carling, P. A. (2013). Freshwater megaflood sedimentation: What can we learn about generic processes? *Earth-Science Reviews*, 125, 87-113.

Carling, P. A., Burr, D. M., Johnsen, T. F., & Brennand, T. A. (2009). A review of open-channel megaflood depositional landforms on earth and mars. *Megaflooding on Earth and Mars*, 33–49. https://doi.org/10.1017/CBO9780511635632.003

Carling, P. A., Kirkbride, a D., Parnachov, S., Borodavko, P. S., & Berger, G. W. (2002). Late Quaternary Catastrophic Flooding in the Altai Mountains of South–Central Siberia: A Synoptic Overview and an Introduction to Flood Deposit Sedimentology. *Flood and Megaflood Processes and Deposits*, October 2015, 17–35. https://doi.org/10.1002/9781444304299.ch2

Carling, P. A., Villanueva, I., Herget, J., Wright, N., Borodavko, P., & Morvan, H. (2010). Unsteady 1D and 2D hydraulic models with ice dam break for Quaternary megaflood, Altai Mountains, southern Siberia. *Global and Planetary Change*, *70*(1–4), 24–34. https://doi.org/10.1016/j.gloplacha.2009.11.005

Carrivick, J. L. (2006). Application of 2D hydrodynamic modelling to high-magnitude outburst floods: An example from Kverkfjöll, Iceland. *Journal of Hydrology*, *321*(1–4), 187–199. https://doi.org/10.1016/j.jhydrol.2005.07.042

Carrivick, J. L., & Rushmer, E. L. (2006). Understanding high-magnitude outburst floods. *Geology Today*, *22*(2), 60-65.

Carrivick, J. L., Jones, R., & Keevil, G. (2011). Experimental insights on geomorphological processes within dam break outburst floods. *Journal of Hydrology*, *408*(1–2), 153–163. https://doi.org/10.1016/j.jhydrol.2011.07.037

Cenderelli, D. A. (2000). Floods from Natural and Artificial Dam Failures. In *Inland Flood Hazards*. https://doi.org/10.1017/cbo9780511529412.004

Cenderelli, D. A., & Wohl, E. E. (2001). Peak discharge estimates of glacial-lake outburst floods and "normal" climatic floods in the Mount Everest region, Nepal. *Geomorphology*, *40*(1-2), 57-90.

Cenderelli, D. A., & Wohl, E. E. (2003). Flow hydraulics and geomorphic effects of glacial-lake outburst floods in the Mount Everest region, Nepal. *Earth Surface Processes and Landforms*, *28*(4), 385–407. https://doi.org/10.1002/esp.448

Central Water Commission Guwahati. (2019). Brahmaputra Basin, 2017-18. *In Water Quality Year Book*, Government of India, Brahmaputra and Barak Basin Organisation. http://old.cwc.gov.in/main/webpages/2017-18.html

Chen, C., Zhang, L., Xiao, T., & He, J. (2020). Barrier lake bursting and flood routing in the Yarlung Tsangpo Grand Canyon in October 2018. *Journal of Hydrology*, 583(August 2019), 124603. https://doi.org/10.1016/j.jhydrol.2020.124603

Cina, S. E., Yin, A., Grove, M., Dubey, C. S., Shukla, D. P., Lovera, O. M., ... & Foster, D. A. (2009). Gangdese arc detritus within the eastern Himalayan Neogene foreland basin: implications for the Neogene evolution of the Yalu–Brahmaputra River system. *Earth and Planetary Science Letters*, 285(1-2), 150-162.

Clague, J. J., & Evans, S. G. (2000). A review of catastrophic drainage of moraine-dammed lakes in British Columbia. *Quaternary Science Reviews*, *19*, 1763–1783. https://doi.org/10.1016/S0277-3791(00)00090-1

Clarke, G. L., Bhowmik, S. K., Ireland, T. R., Aitchison, J. C., Chapman, S. L., & Kent, L. (2016). Inverted Oligo-Miocene metamorphism in the Lesser Himalaya Sequence, Arunachal Pradesh, India; age and grade relationships. *Journal of Metamorphic Geology*, 34(8), 805-820.

Cook, K. L., Andermann, C., Gimbert, F., Adhikari, B. R., & Hovius, N. (2018). Glacial lake outburst floods as drivers of fluvial erosion in the Himalaya. *Science*, *362*(6410), 53–57. https://doi.org/10.1126/science.aat4981

Copeland, P., & Harrison, M. T. (1990). Episodic rapid uplift in the Himalaya revealed by 40Ar/39Ar analysis of detrital K-feldspar and muscovite, Bengal fan.

Corrigan, J. D., & Crowley, K. D. (1990). Fission-track analysis of detrital apatites from sites 717 and 718, Leg 116, Central Indian Ocean. In Proc. Ocean Drill. Program Sci. Results (Vol. 116, pp. 75-92).

Delaney, K. B., & Evans, S. G. (2015). The 2000 Yigong landslide (Tibetan Plateau), rockslide-dammed lake and outburst flood: Review, remote sensing analysis, and process modelling. *Geomorphology*, *246*, 377–393. https://doi.org/10.1016/j.geomorph.2015.06.020

Denlinger, R. P., & O'Connell, D. R. H. (2010). Simulations of cataclysmic outburst floods from Pleistocene glacial lake Missoula. *Bulletin of the Geological Society of America, 122*(5–6), 678–689. https://doi.org/10.1130/B26454.1

Denlinger, R. P., George, D. L., Cannon, C. M., O'Connor, J. E., & Waitt, R. B. (2021). Diverse cataclysmic floods from Pleistocene glacial Lake Missoula. Untangling the Quaternary Period—A Legacy of Stephen C. Porter, *Geological Society of America Special Paper*, 548.

Devi, R. K. M., & Bora, P. K. (2016). The impact of the great 1950 Assam earthquake on the frontal regions of the Northeast Himalaya. Earthquakes and their impact on society, 475-489.

Dewey, J. F., Goff, J., & Ryan, P. D. (2021). The origins of marine and non-marine boulder deposits: a brief review. *Natural Hazards,* 109(2), 1981–2002. https://doi.org/10.1007/s11069-021-04906-3

Dong, X., Hu, X., Garzanti, E., Liang, W., Li, G., Lai, W., ... & Li, Z. (2023). The extraordinary Namche Barwa sediment factory in the Eastern Himalayan Syntaxis. *Basin Research*.

Dunham, A. M., Kiser, E., Kargel, J. S., Haritashya, U. K., Watson, C. S., Shugar, D. H., Hughes, A., & DeCelles, P. G. (2022). Topographic Control on Ground Motions and Landslides From the 2015 Gorkha Earthquake. *Geophysical Research Letters*, 49(10), 1–12. https://doi.org/10.1029/2022GL098582

Enkelmann, E, T.A. Ehlers, P.K. Zeitler, B. Hallet, (2011). Denudation of the Namche Barwa antiform, eastern Himalaya, *Earth and Planetary Science Letters*, Volume 307, Issues 3–4, 323-333. doi:10.1016/j.epsl.2011.05.004.

Evans, S. G., & Clague, J. J. (1994). Recent climatic change and catastrophic geomorphic processes in mountain environments. In *Geomorphology and natural hazards* (pp. 107-128). Elsevier.

Evans, S. G., & Clague, J. J. (1997). The impact of climate change on catastrophic geomorphic processes in the mountains of British Columbia, Yukon and Alberta. *Responding to global climate change in British Columbia and Yukon*, 1, 7-1.

Finlayson, D. P., Montgomery, D. R., & Hallet, B. (2002). Spatial coincidence of rapid inferred erosion with young metamorphic massifs in the Himalayas. *Geology*, 30(3), 219–222. https://doi.org/10.1130/0091-7613(2002)030<0219:SCORIE>2.0.CO;2

Finnegan, N. J., Hallet, B., Montgomery, D. R., Zeitler, P. K., Stone, J. O., Anders, A. M., & Yuping, L. (2008). Coupling of rock uplift and river incision in the Namche Barwa-Gyala

Peri massif, Tibet. *Bulletin of the Geological Society of America*, *120*(1–2), 142–155. https://doi.org/10.1130/B26224.1

Fowler, A. J., Gillespie, R., & Hedges, R. E. (1986). Radiocarbon dating of sediments. *Radiocarbon*, *28*(2A), 441-450.

Galy, V., France-Lanord, C., Beyssac, O., Faure, P., Kudrass, H., & Palhol, F. (2007). Efficient organic carbon burial in the Bengal fan sustained by the Himalayan erosional system. *Nature*, 450(7168), 407-410.

Garcia-Castellanos, D., Estrada, F., Jiménez-Munt, I., Gorini, C., Fernández, M., Vergés, J., & De Vicente, R. (2009). Catastrophic flood of the Mediterranean after the Messinian salinity crisis. *Nature*, *462*(7274), 778-781.

Gardner, M. (2023). Toward a Complete Kinematic Description of Hydraulic Plucking of Fractured Rock. *Journal of Hydraulic Engineering*, *149*(7), 04023015.

Gasparini, N. M., Whipple, K. X., & Bras, R. L. (2007). Predictions of steady state and transient landscape morphology using sediment-flux-dependent river incision models. *Journal of Geophysical Research: Earth Surface*, *112*(3), 1–20. https://doi.org/10.1029/2006JF000567

Gehrels, G. and Pecha, M. (2014). Detrital zircon U-Pb geochronology and Hf isotope geochemistry of Paleozoic and Triassic passive margin strata of western North America: *Geosphere*, v. 10 (1), p. 49-65.

Gehrels, G., Kapp, P., DeCelles, P., Pullen, A., Blakey, R., Weislogel, A., Ding, L., Guynn, J., Martin, A., McQuarrie, N., & Yin, A. (2011). Detrital zircon geochronology of pre-Tertiary strata in the Tibetan-Himalayan orogen. *Tectonics*, *30*(5).

Gehrels, G.E., Valencia, V., Ruiz, J. (2008). Enhanced precision, accuracy, efficiency, and spatial resolution of U-Pb ages by laser ablation–multicollector–inductively coupled plasma–mass spectrometry: *Geochemistry, Geophysics, Geosystem*s, v. 9, Q03017,

Gilbert, G. K. (1890). Lake Bonneville (Vol. 1). United States Geological Survey. 438 pp. doi:10.3133/m1.

Greenbaum, N., Harden, T. M., Baker, V. R., Weisheit, J., Cline, M. L., Porat, N., Halevi, R., & Dohrenwend, J. (2014). A 2000 year natural record of magnitudes and frequencies for the largest Upper Colorado River floods near Moab, Utah. *Water Resources Research*, *50*(6), 5249-5269.

Guo, C., Montgomery, D. R., Zhang, Y., Zhong, N., Fan, C., Wu, R., Yang., Ding Y., Jin J., & Yan, Y. (2020). Evidence for repeated failure of the giant Yigong landslide on the edge of the Tibetan Plateau. *Scientific reports*, 10(1), 14371.

Guo, Y., Ge, Y., Mao, P., & Liu, T. (2023). Reconstruction of mid-Holocene extreme flood events in the upper Minjiang River valley, eastern Tibetan Plateau, China. *Palaeogeography, Palaeoclimatology, Palaeoecology*, *617*, 111517.

Gupta, S., Collier, J. S., Palmer-Felgate, A., & Potter, G. (2007). Catastrophic flooding origin of shelf valley systems in the English Channel. *Nature*, *448*(7151), 342-345.

Gurnell, A. M., Blackall, T. D., & Petts, G. E. (2008). Characteristics of freshly deposited sand and finer sediments along an island-braided, gravel-bed river: the roles of water, wind and trees. *Geomorphology*, *99*(1-4), 254-269.

Henck, A. C., Montgomery, D. R., Huntington, K. W., & Liang, C. (2010). Monsoon control of effective discharge, Yunnan and Tibet. *Geology*, *38*(11), 975–978.

Herget, J., Agatova, A. R., Carling, P. A., & Nepop, R. K. (2020). Altai megafloods—The temporal context. *Earth-Science Reviews*, 200 (March 2019). https://doi.org/10.1016/j.earscirev.2019.102995

Hodge, R. A., Hoey, T. B., & Sklar, L. S. (2011). Bed load transport in bedrock rivers: The role of sediment cover in grain entrainment, translation, and deposition. *Journal of Geophysical Research: Earth Surface*, 116(F4).

Hooker, J. D. (2022). Lithotectonic Framework and Cenozoic Structural Evolution of the Easternmost Himalayan Orogen (*Doctoral dissertation, University of North Carolina Wilmington*).

Hoskin, P. W., & Schaltegger, U. (2003). The composition of zircon and igneous and metamorphic petrogenesis. *Reviews in mineralogy and geochemistry*, *53*(1), 27-62.

Hu, G., Yi, C. L., Liu, J. H., Wang, P., Zhang, J. F., Li, S. H., Li, D., Huang, J., Wang, H., Zhang, A. M., Shi, L., Shui, X. (2020). Glacial advances and stability of the moraine dam on Mount Namcha Barwa since the Last Glacial Maximum, eastern Himalayan syntaxis. *Geomorphology*, *365*, 107246. https://doi.org/10.1016/j.geomorph.2020.107246

Hu, H. P., Feng, J. L., & Chen, F. (2018). Sedimentary records of a palaeo-lake in the middle Yarlung Tsangpo: Implications for terrace genesis and outburst flooding. *Quaternary Science Reviews*, *192*, 135–148. https://doi.org/10.1016/j.quascirev.2018.05.037

Huang, S. Y., Chen, Y. G., Burr, G. S., Jaiswal, M. K., Lin, Y. N., Yin, G., Liu, J., Zhao, S., Cao, Z. (2014). Late Pleistocene sedimentary history of multiple glacially dammed lake episodes along the Yarlung-Tsangpo river, southeast Tibet. *Quaternary Research (United States)*, *82*(2), 430–440. https://doi.org/10.1016/j.yqres.2014.06.001

Huber, M. L., Lupker, M., Gallen, S. F., Christl, M., & Gajurel, A. P. (2020). Timing of exotic, far-traveled boulder emplacement and paleo-outburst flooding in the central Himalayas. *Earth Surface Dynamics*, 8(3), 769–787. https://doi.org/10.5194/esurf-8-769-2020

Japan Aerospace Exploration Agency (2021). ALOS World 3D 30 meter DEM. V3.2, Jan 2021. Distributed by OpenTopography. https://doi.org/10.5069/G94M92HB. Accessed: 2023-08-07

Jha, S. N. 2021 Geo-Ecological Perspective of Hydropower Projects in Siang River Basin. Quest Journals Journal of Research in Environmental and Earth Sciences Volume 7 ~ Issue 6 (2021) pp: 10-15 ISSN(Online) :2348-2532

Johnson, J. P. L., Whipple, K. X., Sklar, L. S., & Hanks, T. C. (2009). Transport slopes, sediment cover, and bedrock channel incision in the Henry Mountains, Utah. *Journal of Geophysical Research: Earth Surface*, *114*(2), 1–21. https://doi.org/10.1029/2007JF000862

Kaiser, K., Lai, Z., Schneider, B., & Junge, F. W. (2010). Late Pleistocene genesis of the middle Yarlung Zhangbo Valley, southern Tibet (China), as deduced by sedimentological and luminescence data. *Quaternary Geochronology*, *5*(2–3), 200–204. https://doi.org/10.1016/j.quageo.2009.01.005

Kochel, R. C., Baker, V. R., & Patton, P. C. (1982). Paleohydrology of southwestern Texas. *Water Resources Research*, *18*(4), 1165-1183.

Komatsu, G., Arzhannikov, S. G., Gillespie, A. R., Burke, R. M., Miyamoto, H., & Baker, V. R. (2009). Quaternary paleolake formation and cataclysmic flooding along the upper Yenisei River. *Geomorphology*, *104*(3-4), 143-164.

Kong, P., Na, C., Fink, D., Zhao, X., & Xiao, W. (2009). Moraine dam related to late Quaternary glaciation in the Yulong Mountains, southwest China, and impacts on the Jinsha River. *Quaternary Science Reviews*, *28*(27–28), 3224–3235. https://doi.org/10.1016/j.quascirev.2009.08.005

Koons, P. O., Zeitler, P. K., & Hallet, B. (2013). Tectonic aneurysms and mountain building. *Treatise on geomorphology*, *5*, 318-349.

Korup, O., & Montgomery, D. R. (2008). Tibetan plateau river incision inhibited by glacial stabilization of the Tsangpo gorge. *Nature*, *455*(7214), 786–789. https://doi.org/10.1038/nature07322

Korup, O., Montgomery, D. R., & Hewitt, K. (2010). Glacier and landslide feedbacks to topographic relief in the Himalayan syntaxes. *Proceedings of the National Academy of Sciences*, *107*(12), 5317–5322. https://doi.org/10.1073/pnas.0907531107

Lamb, M. P., Dietrich, W. E., & Venditti, J. G. (2008). Is the critical shields stress for incipient sediment motion dependent on channel-bed slope? *Journal of Geophysical Research: Earth Surface*, *113*(2), 1–20. https://doi.org/10.1029/2007JF000831

Lamb, M. P., Finnegan, N. J., Scheingross, J. S., & Sklar, L. S. (2015). New insights into the mechanics of fluvial bedrock erosion through flume experiments and theory. *Geomorphology*, *244*, 33–55. https://doi.org/10.1016/j.geomorph.2015.03.003

Lamb, M. P., & Fonstad, M. A. (2010). Rapid formation of a modern bedrock canyon by a single flood event. *Nature Geoscience*, *3*(7), 477–481. https://doi.org/10.1038/ngeo894

Lang, K. A., Huntington, K. W., & Montgomery, D. R. (2013). Erosion of the Tsangpo Gorge by megafloods, Eastern Himalaya. *Geology*, *41*(9), 1003–1006. https://doi.org/10.1130/G34693.1

Lapotre, M. G. A., Lamb, M. P., & Williams, R. M. E. (2016). Canyon formation constraints on the discharge of catastrophic outburst floods of Earth and Mars. *Journal of Geophysical Research: Planets*, *121*(7), 1232–1263. https://doi.org/10.1002/2016JE005061

Larsen, I. J., & Lamb, M. P. (2016). Progressive incision of the Channeled Scablands by outburst floods. *Nature*, *538*(7624), 229–232. https://doi.org/10.1038/nature19817

Larsen, I. J., & Montgomery, D. R. (2012). Landslide erosion coupled to tectonics and river incision. *Nature Geoscience*, *5*(7), 468–473. https://doi.org/10.1038/ngeo1479

Lee, H., Galy, V., Feng, X., Ponton, C., Galy, A., France-Lanord, C., & Feakins, S. J. (2019). Sustained wood burial in the Bengal Fan over the last 19 My. *Proceedings of the National Academy of Sciences of the United States of America*, 116(45), 22518–22525. https://doi.org/10.1073/pnas.1913714116

Lehnigk, K. E., and Larsen, I. J. (2022). Pleistocene megaflood discharge in Grand Coulee, Channeled Scabland, USA. *Journal of Geophysical Research: Earth Surface*, 127, https://doi.org/10.1029/2021JF006135.

LeVeque, R. J., George, D. L., & Berger, M. J. (2011). Tsunami modelling with adaptively refined finite volume methods. *Acta Numerica*, *20*, 211–289.

Licht, A., Dupont-Nivet, G., Win, Z., Swe, H. H., Kaythi, M., Roperch, P., Ugrai, T., Littell, V., Park, D., Westerweel, J., Jones, D., Poblete, F., Aung, D. W., Huang, H., Hoorn, C., & Sein,

K. (2019). Paleogene evolution of the Burmese forearc basin and implications for the history of India-Asia convergence. *Geological Society of America Bulletin*, 131(5-6), 730-748.

Liebke, U., Antolin, B., Appel, E., Basavaiah, N., Mikes, T., Dunkl, I., & Wemmer, K. (2011). Indication for clockwise rotation in the Siang window south of the eastern Himalayan syntaxis and new geochronological constraints for the area. *Geological Society, London, Special Publications*, 353(1), 71-97.

Lin, Y., An, C., Parker, G., Liu, W., & Fu, X. (2022). Morphodynamics of Bedrock-Alluvial Rivers Subsequent to Landslide Dam Outburst Floods. *Journal of Geophysical Research: Earth Surface*, 127(9). https://doi.org/10.1029/2022JF006605

Liu, W., Cui, P., Ge, Y., & Yi, Z. (2018). Paleosols identified by rock magnetic properties indicate dam-outburst events of the Min River, eastern Tibetan Plateau. *Palaeogeography, Palaeoclimatology, Palaeoecology*, *508*(December 2017), 139–147. https://doi.org/10.1016/j.palaeo.2018.07.029

Liu, W., Lai, Z., Hu, K., Ge, Y., Cui, P., Zhang, X., & Liu, F. (2015). Age and extent of a giant glacial-dammed lake at Yarlung Tsangpo gorge in the Tibetan Plateau. *Geomorphology*, *246*, 370–376. https://doi.org/10.1016/j.geomorph.2015.06.034

Liu, Y., Montgomery, D. R., Hallet, B., Tang, W., Zhang, J., & Zhang, X. (2006). Quaternary glacier blocking events at the entrance of Yarlung Zangbo Great Canyon, Southeast Tibet. *Quaternary Sciences*, *26*, 52–62.

Meunier, P., Hovius, N., & Haines, A. J. (2007). Regional patterns of earthquake-triggered landslides and their relation to ground motion. Geophysical Research Letters, 34(20).

Miller, A. J. (1995). Valley morphology and boundary conditions influencing spatial patterns of flood flow. *Natural and Anthropogenic Influences in Fluvial Geomorphology*, 57-81 (66-90 in file).

Misra, D. K., & Srivastava, P. (2009). River response to continuing movements along the active faults in the Siang valley, North-Eastern Himalaya, India. Zeitschrift Fur Geomorphologie, 53(4), 455–468. https://doi.org/10.1127/0372-8854/2009/0053-0455Montgomery, D. R., & Korup, O. (2010). Preservation of inner gorges through repeated Alpine glaciations. *Nature Geoscience*, *4*, 62. Retrieved from https://doi.org/10.1038/ngeo1030

Montgomery, D. R., Hallet, B., Yuping, L., Finnegan, N. J., Anders, A. M., Gillespie, A. R., & Greenberg, H. M. (2004). Evidence for Holocene megafloods down the Tsangpo River

gorge, southeastern Tibet. *Quaternary Research, 62*(2), 201–207. https://doi.org/10.1016/j.yqres.2004.06.008

Morey, S. M., Huntington, K. W., Turzewski, M. D., Mangipudi, M., & Montgomery, D. R. (2022). The Erosional and Depositional Potential of Holocene Tibetan Megafloods through the Yarlung Tsangpo Gorge, Eastern Himalaya: Insights from 2D Hydraulic Simulations. *Journal of Geophysical Research: Earth Surface*, 127(5), 1–23. https://doi.org/10.1029/2021JF006498

Morey, S. M., Lang, K. A., Huntington, K. W., Shobe C. M., Nath, S., Loreen, C. (in prep). Sedimentary evidence of Quaternary megaflood deposition in the Siyom River valley, eastern Himalaya. *Geological Society of America Bulletin.*

Morey, S. M., Shobe C. M., Huntington, K. W., Lang, K. A., Johnson, A. G., Duvall, A. R. (in review). The lasting legacy of megaflood boulder deposition in mountain rivers. *Geophysical Research Letters*.

Nag, D., Phartiyal, B., Kumar, P., Joshi, P., & Singh, R. (2022). Geomorphological and sedimentological evidences of palaeo-outburst flood events from TanglangLa-Gya catchment of River Indus, Ladakh, India. *Physical Geography*, *43*(6), 879-901.

Najman, Y., Bickle, M., BouDagher-Fadel, M., Carter, A., Garzanti, E., Paul, M.,Wijbrans, J., Willett, E., Oliver, E., Oliver, G., Parrish, R., Akhter, S. H., Allen, R., Ando, S., Chisty, E., Reisberg, L. Vezzoli, G. (2008). The Paleogene record of Himalayan erosion: Bengal Basin, Bangladesh. *Earth and Planetary Science Letters*, *273*(1–2), 1–14. https://doi.org/10.1016/j.epsl.2008.04.028

Nelson, A., & Dubé, K. (2016). Channel response to an extreme flood and sediment pulse in a mixed bedrock and gravel-bed river. *Earth Surface Processes and Landforms*, 41(2), 178-195.

Nelson, R. E., Carter, L. D., & Robinson, S. W. (1988). Anomalous radiocarbon ages from a Holocene detrital organic lens in Alaska and their implications for radiocarbon dating and paleoenvironmental reconstructions in the Arctic. *Quaternary Research*, *29*(1), 66-71.

Nowicki Jessee, M. A., Hamburger, M. W., Allstadt, K., Wald, D. J., Robeson, S. M., Tanyas, H., Hearne, M., & Thompson, E. M. (2018). A Global Empirical Model for Near-Real-Time Assessment of Seismically Induced Landslides. *Journal of Geophysical Research: Earth Surface*, 123(8), 1835–1859. https://doi.org/10.1029/2017JF004494

O'Connor, J. E., & Beebee, R. A. (2009). Floods from natural rock-material dams. In *Megaflooding on Earth and Mars*. https://doi.org/10.1017/CBO9780511635632.008

O'Connor, J. E., & Waitt, R. B. (1995). Beyond the Channeled Scabland—A field trip guide to Missoula flood features in the Columbia. Yakima, and Walla Walla Valleys of Washington and Oregon: *Oregon Geology*, 57(Part I), 51-60.

O'Connor, J. E., Baker, V. R., Waitt, R. B., Smith, L. N., Cannon, C. M., George, D. L., & Denlinger, R. P. (2020). The Missoula and Bonneville floods—A review of ice-age megafloods in the Columbia River basin. *Earth-Science Reviews*, *208*, 103181.

O'Connor, J. E., Clague, J. J., Walder, J. S., Manville, V., & Beebee, R. A. (2013). Outburst Floods. *In Treatise on Geomorphology* (Vol. 9). https://doi.org/10.1016/B978-0-12-374739-6.00251-7

O'Connor, J.E., Sarna-Wojcick, A., Woznikak, K.C., Polette, D.J., Fleck, R.J., (2001), Origin, Extent, and Thickness of Quaternary Geologic Units in the Willamette Valley, Oregon; *U.S. Geological Survey, Professional Paper* 1620, 51 p.

O'Connor, J. E. (1993). Hydrology, hydraulics, and geomorphology of the Bonneville flood (Vol. 274). *Geological Society of America*.

O'Connor, J. E., & Baker, V. R. (1992). Magnitudes and implications of peak discharges from glacial Lake Missoula. *Geological Society of America Bulletin*, 104(3), 267-279.

Panda, S., Kumar, A., Das, S., Devrani, R., Rai, S., Prakash, K., & Srivastava, P. (2020). Chronology and sediment provenance of extreme floods of Siang River (Tsangpo-Brahmaputra River valley), northeast Himalaya. *Earth Surface Processes and Landforms*, *45*(11), 2495–2511. https://doi.org/10.1002/esp.4893

Parkash, S. (2013). Earthquake related landslides in the Indian Himalaya: experiences from the past and implications for the future. *Landslide Science and Practice: Volume 5: Complex Environment*, 327-334.

Pickering, J. L., Diamond, M. S., Goodbred, S. L., Grall, C., Martin, J. M., Palamenghi, L., … Spiess, V. (2018). Impact of glacial-lake paleofloods on valley development since glacial termination II: A conundrum of hydrology and scale for the lowstand Brahmaputra-Jamuna paleovalley system. *Geological Society of America Bulletin*, (Xx), 14. https://doi.org/https://doi .org /10 .1130 /B31941 .1

Piotrowska, N., Blaauw, M., Mauquoy, D., & Chambers, F. M. (2011). Constructing deposition chronologies for peat deposits using radiocarbon dating. *Mires and Peat*, *7*(10), 1-14.

Pullen, A., Ibanez-Mejia, M., Gehrels, G., Giesler, D., and Pecha, M. (2018). Optimization of a Laser Ablation-Single Collector-Inductively Coupled Plasma-Mass Spectrometer (Thermo

Element 2) for Accurate, Precise, and Efficient Zircon U-Th-Pb Geochronology: *Geochemistry, Geophysics, Geosystems*, v. 19. https://doi. org/10.1029/2018GC007889

Rault, C., Robert, A., Marc, O., Hovius, N., & Meunier, P. (2019). Seismic and geologic controls on spatial clustering of landslides in three large earthquakes. Earth Surface Dynamics, 7(3), 829–839. https://doi.org/10.5194/esurf-7-829-2019

Reimer, P. J., Austin, W. E., Bard, E., Bayliss, A., Blackwell, P. G., Ramsey, C. B., ... & Talamo, S. (2020). The IntCal20 Northern Hemisphere radiocarbon age calibration curve (0–55 cal kBP). Radiocarbon, 62(4), 725-757.

Rice Jr, J. W., & Edgett, K. S. (1997). Catastrophic flood sediments in Chryse Basin, Mars, and Quincy Basin, Washington: Application of sandar facies model. *Journal of Geophysical Research: Planets*, *102*(E2), 4185-4200.

Salvi, D., Mathew, G., Pande, K., & Kohn, B. P. (2021). Phased cooling of the Siang antiform, Eastern Himalaya: Insight from multi-thermochronology and thermal studies. *Journal of Earth System Science*, 130, 1-20.

Scherler, D., DiBiase, R. A., Fisher, G. B., & Avouac, J. P. (2017). Testing monsoonal controls on bedrock river incision in the Himalaya and Eastern Tibet with a stochastic-threshold stream power model. *Journal of Geophysical Research: Earth Surface, 122*(7), 1389–1429. https://doi.org/10.1002/2016JF004011

Schmidt, K. L., Kauffman, J. D., Stewart, D. E., Garwood, D. L., Othberg, K. L., & Lewis, R. S. (2009). Geologic map of the Grave Point Quadrangle, Idaho County, Idaho, and Wallowa County, Oregon. *Idaho Geol. Sur., Digital Web Map, 111*.

Schneider, J.M., Rickenmann, D., Turowski, J.M., Bunte, K., Kirchner, J.W. (2015). Applicability of bed load transport models for mixed-size sediments in steep streams considering macro-roughness. *Water Resour. Res*. 51, 5260–5283.

Schwanghart, W., Scherler, D. (2014): TopoToolbox 2 – MATLAB-based software for topographic analysis and modeling in Earth surface sciences. *Earth Surface Dynamic*s, 2, 1-7. [DOI: 10.5194/esurf-2-1-2014]

Seward, D., & Burg, J. P. (2008). Growth of the Namche Barwa Syntaxis and associated evolution of the Tsangpo Gorge: Constraints from structural and thermochronological data. *Tectonophysics*, 451(1–4), 282–289. https://doi.org/10.1016/j.tecto.2007.11.057

Shackleton, N. J., & Opdyke, N. D. (1977). Oxygen isotope and palaeomagnetic evidence for early Northern Hemisphere glaciation. *Nature*, 270(5634), 216-219.

Sharma, C. P., Chahal, P., Kumar, A., Singhal, S., Sundriyal, Y. P., Ziegler, A. D., Agnihotri, R., Wasson, R. J., Shukla, U. K., & Srivastava, P. (2022). Late Pleistocene–Holocene flood history, flood-sediment provenance and human imprints from the upper Indus River catchment, Ladakh Himalaya. *Bulletin*, *134*(1-2), 275-292.

Shekut, S., Licht, A., & Abu-Alam, T. S. (2020). Late middle Miocene emergence of the Olympic Peninsula shown by sedimentary provenance. *Lithosphere*, 2020(1).

Shobe, C. M., Tucker, G. E., & Anderson, R. S. (2016). Hillslope-derived blocks retard river incision. *Geophysical Research Letters*, *43*(10), 5070–5078. https://doi.org/10.1002/2016GL069262

Shobe, C. M., Tucker, G. E., & Rossi, M. W. (2018). Variable-Threshold Behavior in Rivers Arising From Hillslope-Derived Blocks. Journal of Geophysical Research: Earth Surface, 123(8), 1931–1957. https://doi.org/10.1029/2017JF004575

Shobe, C. M., Turowski, J. M., Nativ, R., Glade, R. C., Bennett, G. L., & Dini, B. (2021). The role of infrequently mobile boulders in modulating landscape evolution and geomorphic hazards. Earth-Science Reviews, 220(January), 103717. https://doi.org/10.1016/j.earscirev.2021.103717

Singh, A. K., & Bikramaditya Singh, R. K. (2012). Petrogenetic evolution of the felsic and mafic volcanic suite in the siang window of Eastern Himalaya, Northeast India. *Geoscience Frontiers*, *3*(5), 613–634. https://doi.org/10.1016/j.gsf.2012.01.004

Sklar, L. S., & Dietrich, W. E. (2004). A mechanistic model for river incision into bedrock by saltating bed load. *Water Resources Research*, *40*(6). https://doi.org/10.1029/2003WR002496

Smith, G. A. (1993). Missoula flood dynamics and magnitudes inferred from sedimentology of slack-water deposits on the Columbia Plateau, Washington. Geological Society of America Bulletin, 105(1), 77-100.

Song, Z., Zhen-han, W., Xi-tao, Z., & Ke-yan, X. (2013). Glacial dammed lakes in the Tsangpo River during late Pleistocene, southeastern Tibet. *Quaternary International*, *298*, 114–122. https://doi.org/10.1016/j.quaint.2012.11.004

Srivastava, P., & Misra, D. K. (2012). Optically Stimulated Luminescence chronology of terrace sediments of Siang River, Higher NE Himalaya: Comparison of quartz and feldspar chronometers. *Journal of the Geological Society of India*, *79*(3), 252–258. https://doi.org/10.1007/s12594-012-0043-x

Srivastava, P., Kumar, A., Chaudhary, S., Meena, N., Sundriyal, Y. P., Rawat, S., Rana, N., Perumal, R. J., Bisht, P., Sharma, D., Agnihotri, R., Bagri, D.S., Juyal, N., Wasson, R. J., Ziegler, A. D. (2017). Paleofloods records in Himalaya. *Geomorphology*, *284*, 17–30. https://doi.org/10.1016/j.geomorph.2016.12.011

Stewart, C. L. (2020). Paleofloods and landform development influence carbon storage in a humid-subtropical river valley.

Stewart, R. J., Hallet, B., Zeitler, P. K., Malloy, M. A., Allen, C. M., & Trippett, D. (2008). Brahmaputra sediment flux dominated by highly localized rapid erosion from the easternmost Himalaya. Geology, 36(9), 711-714. doi: 10.1130/G24890A.1

Stock, J. D., & Montgomery, D. R. (1999). Geologic constraints on bedrock river incision using the stream power law. *Journal of Geophysical Research: Solid Earth*, *104*(B3), 4983–4993. https://doi.org/10.1029/98JB02139

Stucky de Quay, G., Roberts, G. G., Rood, D. H., & Fernandes, V. M. (2019). Holocene uplift and rapid fluvial erosion of Iceland: A record of post-glacial landscape evolution. *Earth and Planetary Science Letters*, *505*, 118–130. https://doi.org/10.1016/j.epsl.2018.10.026

Stuiver, M., & Reimer, P. J. (1993). Extended ^{14}C data base and revised CALIB 3.0 14C age calibration program. Radiocarbon, 35(1), 215-230.

Thayer, J. B., & Ashmore, P. (2016). Floodplain morphology, sedimentology, and development processes of a partially alluvial channel. Geomorphology, 269, 160-174.

Turowski, J. M., Hovius, N., Meng-Long, H., Lague, D., & Men-Chiang, C. (2008). Distribution of erosion across bedrock channels. *Earth Surf. Process. Landforms*, *33*, 353–363. https://doi.org/10.1002/esp.1559

Turowski, J. M., Lague, D., & Hovius, N. (2007). Cover effect in bedrock abrasion: A new derivation and its implications for the modeling of bedrock channel morphology. *Journal of Geophysical Research: Earth Surface*, *112*(4), 1–16. https://doi.org/10.1029/2006JF000697

Turzewski, M. D., Huntington, K. W., & LeVeque, R. J. (2019). The geomorphic impact of outburst floods: integrating numerical simulations, field and remote sensing observations of an extreme flood event in the eastern Himalaya. *Journal of Geophysical Research: Earth Surface*.

Turzewski, M. D., Huntington, K. W., Licht, A., & Lang, K. A. (2020). Provenance and erosional impact of Quaternary megafloods through the Yarlung-Tsangpo Gorge from

zircon U-Pb geochronology of flood deposits, eastern Himalaya. *Earth and Planetary Science Letters*, *535*, 116113. https://doi.org/10.1016/j.epsl.2020.116113

van der Bilt, W. G., Barr, I. D., Berben, S. M., Hennekam, R., Lane, T., Adamson, K., & Bakke, J. (2021). Late Holocene canyon-carving floods in northern Iceland were smaller than previously reported. *Communications earth & environment*, *2*(1), 86.

Vermeesch, P., 2012. On the visualisation of detrital age distributions. *Chemical Geology*, v.312-313, 190-194, doi: 10.1016/j.chemgeo.2012.04.021 0

Waitt, R. B. (1984). Periodic jökulhlaups from Pleistocene glacial Lake Missoula—new evidence from varved sediment in northern Idaho and Washington. Quaternary Research, 22(1), 46-58.

Waitt, R. B. (2016). Megafloods and Clovis cache at Wenatchee, Washington. *Quaternary Research*, *85*(3), 430-444.

Walder, J. S., & Costa, J. E. (1996). Outburst floods from glacier-dammed lakes: The effect of mode of lake drainage on flood magnitude. *Earth Surface Processes and Landforms*, 21(8), 701-723.

Wang, H., Tong, K., Hu, G., Wang, P., Li, D., Huang, J., Cao, G., Zhang, J. & Chen, J. (2021). Dam and megafloods at the First Bend of the Yangtze River since the Last Glacial Maximum. *Geomorphology*, *373*, 107491.

Wang, P., Wang, H., Hu, G., Ge, Y., Liu, T., & Xu, B. (2023). Reconstructing post-mid Pleistocene glacial-dammed paleolakes in the Tsangpo Gorge, southeastern Tibetan Plateau. *Quaternary Science Reviews*, *314*, 108228.

Wang, Y., Zhang, H., Zheng, D., von Dassow, W., Zhang, Z., Yu, J., & Pang, J. (2017). How a stationary knickpoint is sustained: New insights into the formation of the deep Yarlung Tsangpo Gorge. Geomorphology, 285, 28–43. https://doi.org/10.1016/j.geomorph.2017.02.005

Whipple, K. X., Hancock, G. S., & Anderson, R. S. (2000). River incision into bedrock: Mechanics and relative efficacy of plucking, abrasion, and cavitation. *Bulletin of the Geological Society of America*, *112*(3), 490–503. https://doi.org/10.1130/0016-7606(2000)112<490:RIIBMA>2.0.CO

Williams, P. F., & Rust, B. R. (1969). The sedimentology of a braided river. Journal of Sedimentary Research, 39(2).

Wohl, E. (2010). A brief review of the process domain concept and its application to quantifying sediment dynamics in bedrock canyons. Terra Nova, 22(6), 411-416. https://doi.org/10.1111/j.1365-3121.2010.00950.x

Wohl, E. E., & David, G. C. L. (2008). Consistency of scaling relations among bedrock and alluvial channels. Journal of Geophysical Research, 113(F4), F04013. https://doi.org/10.1029/2008JF000989

Xu, Q., Ji, J., Zhong, D., Hu, Y., Deino, A., Chen, J., Tu. H., Liu H., Wang H., Sun, D. (2020). Post-glacial entrenchment and knickpoint migration of the Yarlung Tsangpo Gorge, southeastern Tibetan Plateau. Journal of Asian Earth Sciences, 195(March), 104337. https://doi.org/10.1016/j.jseaes.2020.104337

Yang, R., Herman, F., Fellin, M. G., & Maden, C. (2018). Exhumation and topographic evolution of the Namche Barwa Syntaxis, eastern Himalaya. *Tectonophysics*, *722*(October 2017), 43–52. https://doi.org/10.1016/j.tecto.2017.10.026

Zeitler, P. K., Meltzer, A. S., Brown, L., Kidd, W. S. F., Lim, C., & Enkelmann, E. (2014). Tectonics and topographic evolution of Namche Barwa and the easternmost Lhasa block, Tibet. *Geological Society of America Special Papers*, *SPE507-02*, 23–58.

Zhang, J. Y., Yin, A., Liu, W. C., Wu, F. Y., Lin, D., & Grove, M. (2012). Coupled U-Pb dating and Hf isotopic analysis of detrital zircon of modern river sand from the yalu river (Yarlung Tsangpo) drainage system in southern tibet: Constraints on the transport processes and evolution of himalayan rivers. *Bulletin of the Geological Society of America*, *124*(9–10), 1449–1473. https://doi.org/10.1130/B30592.1

Zhang, L., Stark, C., Schumer, R., Kwang, J., Li, T., Fu, X., Wang, G., & Parker, G. (2018). The Advective-Diffusive Morphodynamics of Mixed Bedrock-Alluvial Rivers Subjected to Spatiotemporally Varying Sediment Supply. Journal of Geophysical Research: Earth Surface, 123(8), 1731–1755. https://doi.org/10.1029/2017JF004431

Zhu, S., Wu, Z., Zhao, X., Li, J., & Wang, H. (2012). Middle-late Pleistocene glacial lakes in the grand canyon of the Tsangpo River, Tibet. *Acta Geologica Sinica*, *86*(1), 266–283. https://doi.org/10.1111/j.1755-6724.2012.00627.x

Zwoliński, Z. (1992). Sedimentology and geomorphology of overbank flows on meandering river floodplains. Geomorphology, 4(6), 367-379.

APPENDIX A

Supporting Information for Chapter 1

The erosional and depositional potential of Holocene Tibetan megafloods throughout the Yarlung Tsangpo Gorge, eastern Himalaya: insights from 2D hydraulic simulations

S. M. Morey[1], K. W. Huntington[1], M. D. Turzewski[2], M. Mangipudi[1,3], and D. R. Mongtomery[1]

[1]Department of Earth and Space Science, University of Washington, Seattle, WA, USA.
[2]Department of Geosciences, Pacific Lutheran University, Tacoma, WA, USA.
[3]Stanford University, Stanford, CA, USA.

Contents of this file

Additional Supporting Information

Introduction

The Appendix below includes supplemental figures that are useful, but not necessary for understanding the main text, tables with details about (1) the previously identified megaflood deposits, (2) GeoClaw inputs, and (3) inundation extents for each inundated tributary. Sources for the previously identified megaflood deposits are listed. Inundation extents come from simulation results. Additionally, we include two data sets. The first of which shows depth, speed, stress, and flood power through time at the location of each megaflood deposit. The second shows depth, speed, stress, and flood power through time along the centerline of the modern channel at every kilometer downstream of the Gorge. This data is not averaged using a 5-minute moving average, as other data was in the main text. Note that, while our results for maps of megaflood hydraulics span from 0 to 63 hours, our results at individual locations only span from 0 to 52 hours. We have also included 25 movies that are referenced throughout the text. Their locations are linked to figures in the main text and are noted within each caption.

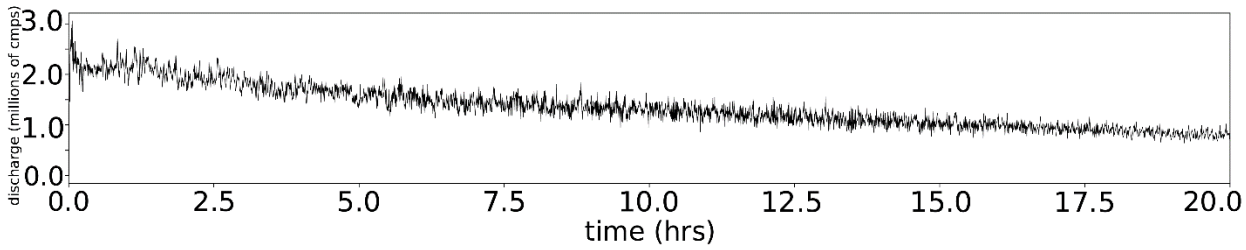

Figure A1. Discharge at the dam breach in cubic meters per second. Discharge was measured at a cross section 1 km downstream of the dam

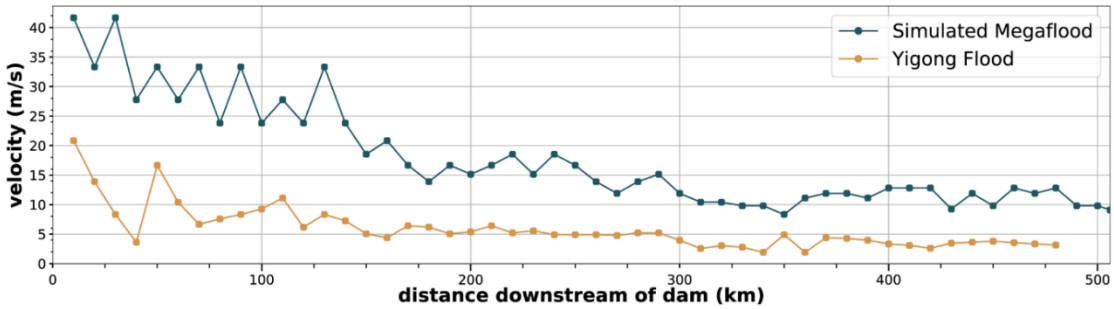

Figure A2. Frontal flood wave velocity for the simulated megaflood and the simulated 2000 Yigong Flood measured in meters per second.

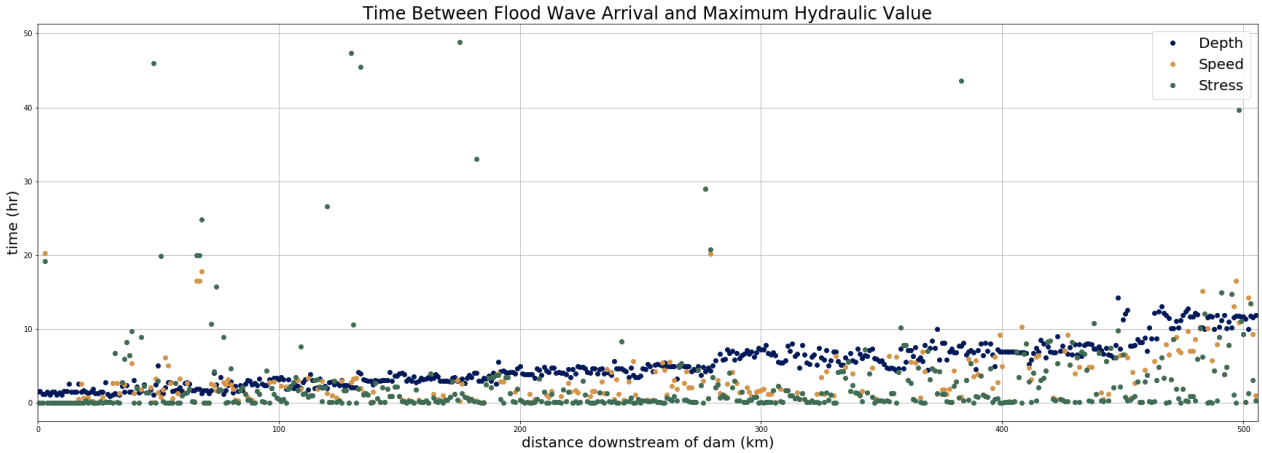

Figure A3. Time between simulated frontal megaflood wave arrival and maximum hydraulic value.

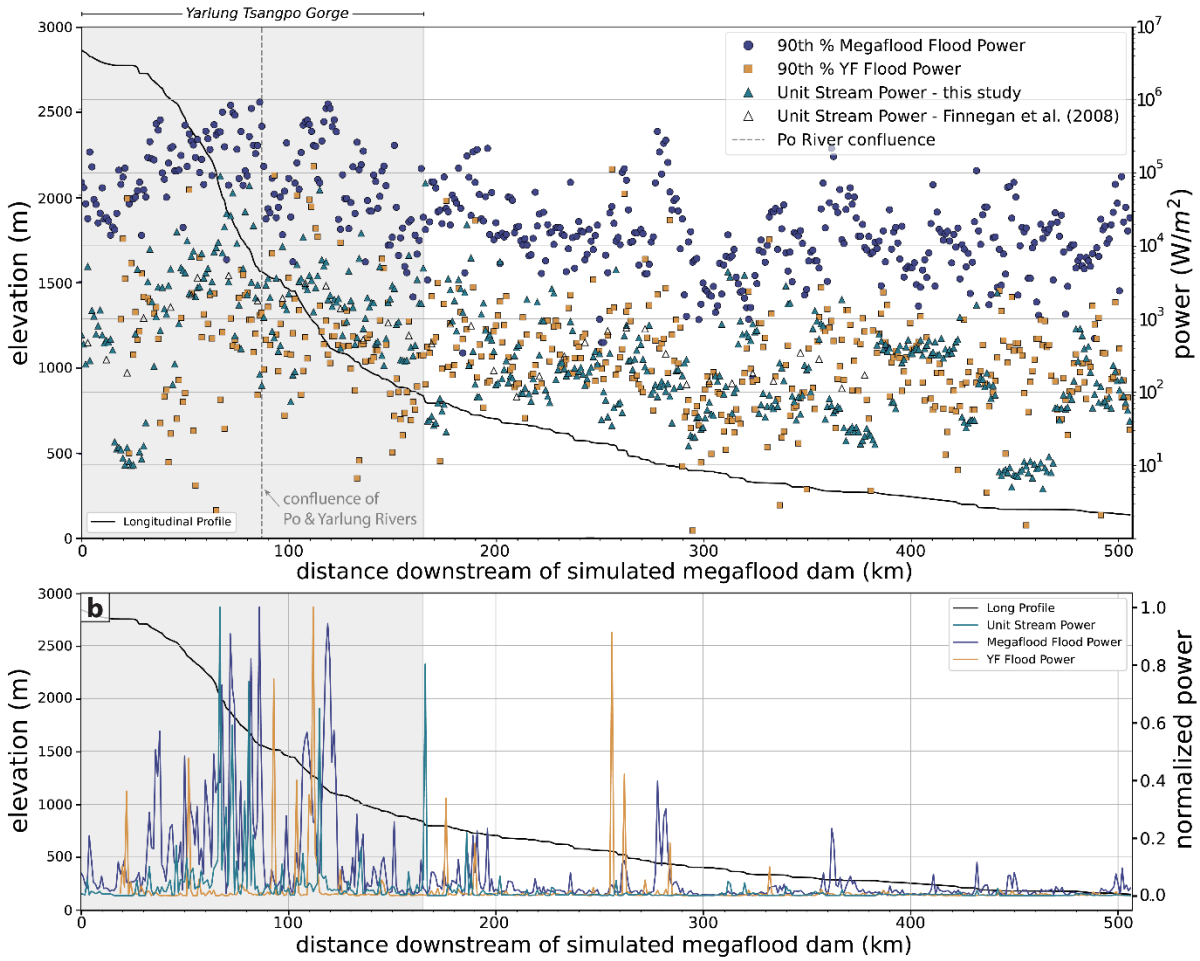

Figure A4. a) Unit stream power and 90th percentile flood power per unit area (W/m^2) for the simulated megaflood and YF along the longitudinal profile of the YSR, all plotted on a log scale vs. distance downstream of the simulated megaflood (see Figure 1.2 caption for details). The Gorge region is shaded. Blue circles and yellow squares are 90th percentile megaflood and YF flood power (over a 5-minute moving window), respectively, calculated from GeoClaw outputs measured at a point along the YSR channel axis. Teal triangles are unit stream power of the YSR at those same points in this study. Unfilled triangles are measurements of unit stream power averaged every 10 km from Finnegan et al. (2008). See Figure 1.8 for 10 km averaged megaflood and YF flood power values. b) The same 90th percentile megaflood flood power and YF flood power, and unit stream power (from this study) from (a) but normalized to the maximum values of each dataset to more easily compare spatial patterns.

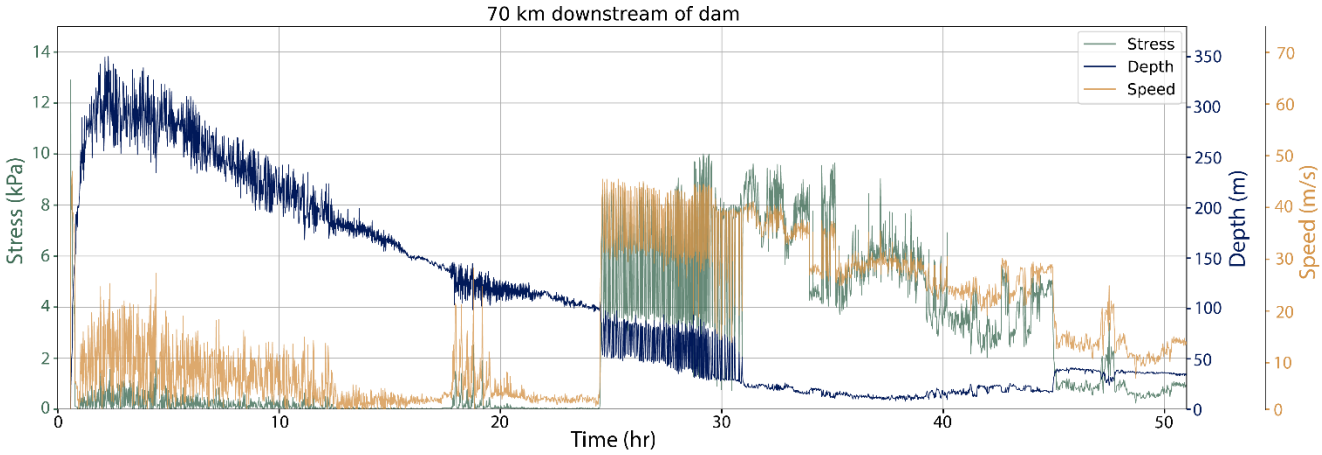

Figure A5. Time series of a location with a late increase in stress and speed. This measurement is taken 70 km downstream of dam on the centerline of the modern Yarlung River.

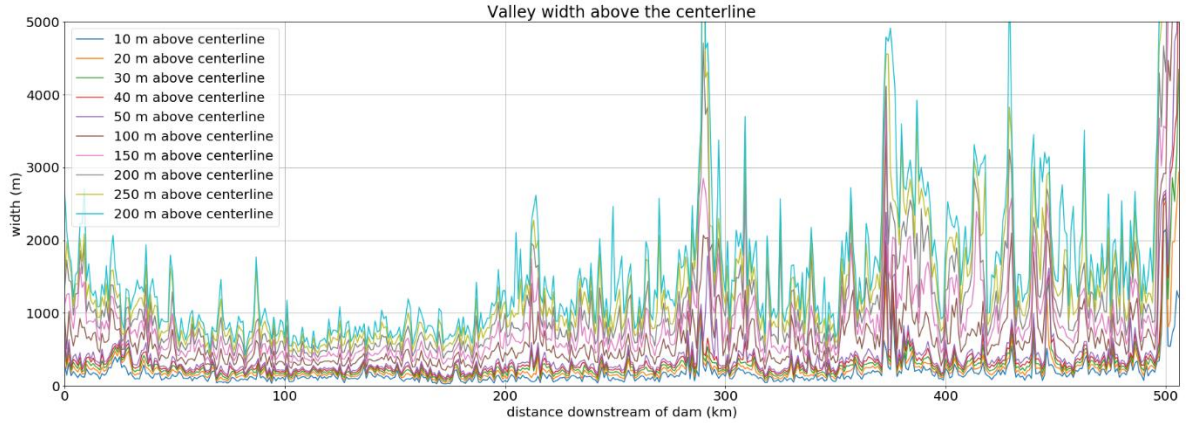

Figure A6. Measurements of valley width above the Yarlung-Siang channel center axis. Each valley width is measured at a certain height above the center axis. For example, the blue line is the width measured 10 m above the channel and the green line is measured 30 m above the channel.

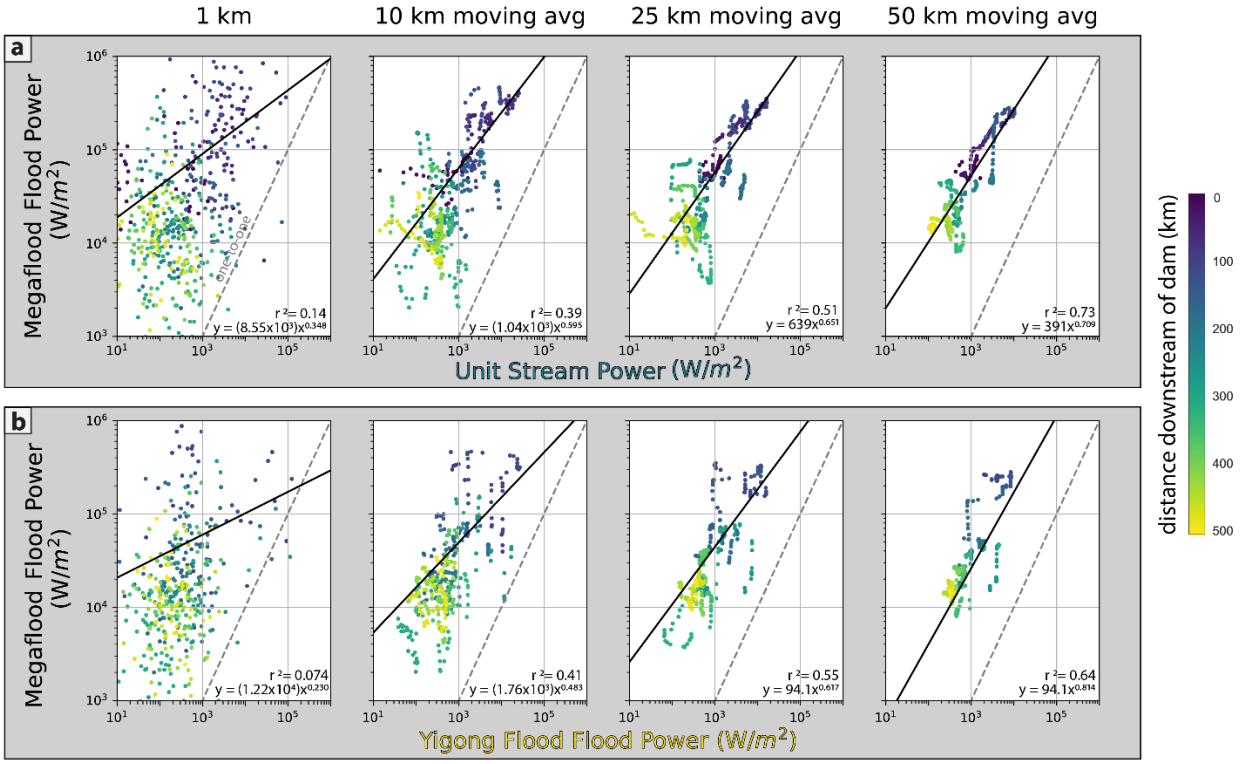

Figure A7. Comparison of stream power and 90th percentile flood power, both in Watts per square meter (W/m^2). Color is coded to distance downstream of dam. The dashed line plotted is one-to-one, while the solid lines represents the best fit line in a least squares sense. Equations for significant power-law regression relationships with r-squared value are shown. This plot contains data from the same locations as in Figure 1.8.

Figure A8. Field photo that demonstrates the difference in lithology between the bedrock (metasedimentary) and the large boulders (granodioritic) that rest upon it. This photo was taken at a boulder bar across the Siang River from Tuting.

Table A1. Previously identified megaflood deposits along the Siang River along with all published information about each deposit. Italics indicates that the deposit was not inundated during the simulated megaflood. *Deposits correlate to locations in Figure 1.2.*

study deposit first appears	#	sample name from relevant study	ID from relevant study	longitude	latitude	site location	physical location	description from study if given
Srivastava and Misra (2012)	1	TS-1	LD-517	94.888222	29.005861	Tuting	terrace (T4)	situated at ~88marl on highest elevation (oldest) terrace (~600 m above mean sea level (amsl)), ~8m offine grained sand capped by a meter of thick clayey silt overlies an alluvial terrace and is dated to 8±1 ka
	2	TS-2	LD-518	94.894306	28.993667	Tuting	terrace (T3)	taken from sandy layer (overlain by thick fluvial gravels and underlain by bedrock) on terrace that is ~550 m amsl
	3	TS-3	LD-519	94.894306	28.993667	Tuting	terrace (T3)	taken from sandy layer (overlain by thick fluvial gravels and underlain by bedrock) on terrace that is ~550 m amsl
	4	TS-4	LD-520	94.8955	28.997222	Tuting	terrace (Fan terrace T2)	sample taken from fan that emerges from terrace above it; fan aprons terrace below
	5	TS-5	LD-521	94.902806	28.981472	Tuting	terrace (T1)	on lowest elevation (youngest) terrace at 460 m amsl
	6	TS-6	LD-522	94.898583	29.041528	Tuting	above modern channel	valley fill ~6km upstream of Tuting
Lang et al. (2013)	1	08KH10		94.906178	29.051355	Tuting	alcove	none given
	2	08KH24		94.847082	28.965512	Tuting	terrace	ancient sand in road. laminated flood deposit. GS: medium to fine sand. soil on top. Indurated;
	3	08KH28		94.953281	28.317577	Boleng	terrace	ancient flood. Bolen Gas station.
	4	PFS-1		94.983443	28.233917	Siyom Confluence	tributary junction	none given

Srivastava et al. (2017)	1	YS-4	LD-551	95.01275	28.657222	Yinkiong	terrace	a 6 m thick flood sequence made up of oxidized, parallel laminated fine sand, with bar and swell topography, is located at ~98 m arl; The sequence is moderately bioturbated and is capped by a ~ 50 cm thick unit of clayey silt. A sample at a depth of 1.8 m has an OSL age of 7 ± 1 ka;
	2	*PS-1*	*LD-553*	*94.996694*	*28.219861*	*Panging*	*terrace*	*Similar fine grained sandy sequences dating to ~7 ka;*
	3	SG-1	LD-677	95.089917	28.420806	Geku	terrace	a similar 3.5m thick sequence of parallel laminated, moderately bioturbated, oxidized fine sand and extends laterally for over 1 km on undulatory topography. The deposit seats at ~98 m arl. A sample from 1 m above the base is dated to 6 ± 1 ka
Turzewski et al. (2020)	1	13SI21		95.02667	28.63944	Yinkiong	terrace	Large sand deposit in Yingkiong. Around 4 m exposed above road in town. Steeply sloping surface above deposit covered by vegetation and soils.
	2	13SI34		95.06693	28.57959	south of Yinkiong	terrace	Sand deposit taken from between landslide deposits
	3	13SI32		95.06281	28.57915	south of Yinkiong	terrace	Sand deposit taken from between landslide deposits
	4	13SI28		95.06302	28.5763	south of Yinkiong	terrace	Sand deposit taken from between landslide deposits. Highest deposit at Nubo bridge site.
	5	13SI40		95.08376	28.41904	Geku	terrace	2-3 m of sand taken from a roadcut near Geku. Deposit has soil on top.
	6	13SI11		94.98277	28.23355	Siyom Confluence	tributary junction	Two layers (third layer in the middle of outcrop) of sand separated by landslide material. Landslide terminates further down the road and deposit is all sand after this point. Landslide material and debris follow topography of lower sand layer. Sand has centimeter to decimeter scale bedding. Sample taken from highest sand layer

	7	*13SI02*	*95.19072*	*28.1533*	*near Yamne confluence*	*above modern channel*	*3-4 m of sand above landslide and deformed metamorphic units. Sand is covered by landslide. Sand layer is thicker near contact with metamorphic rocks. Basal contact is draped over topography along the deposit. Boulders of meter scale at base of deposit. Cut on both sides by more recent landsliding. Approx. 90 meters in length. Sand layer is fine to coarse and homogeneous. Has rare centimeter pebbles. Millimeter to centimeter scale bedding. Weathered near base. Very hard, possibly imbricated.*
Borgohain et al. (2020)	1	T1	94.89	28.99	Tuting	terrace	tributary junction; slackwater deposit
	2	T3	94.85	28.96	Tuting	terrace	tributary junction; slackwater deposit
	3	T2	94.903828	28.983536	Tuting	terrace	tributary junction; location approximate; given location was off; slackwater deposit
	4	Y3	95.03	28.61	Yingkiong	terrace	tributary junction; slackwater deposit
	5	Y2	95.02	28.63	Yingkiong	terrace	tributary junction; slackwater deposit
	6	Y1	95.03	28.64	Yingkiong	terrace	tributary junction; slackwater deposit
	7	Y4	95.02	28.63	Yingkiong	terrace	tributary junction; slackwater deposit
	8	G5	95.08	28.4	Geku	alcove	alcove; slackwater deposit
	9	G1	95.09	28.42	Geku	terrace	alcove; terrace; slackwater deposit
	10	G4	95.09	28.43	Geku	terrace	alcove; terrace; slackwater deposit
	11	G2	95.09	28.43	Geku	terrace	alcove; terrace; slackwater deposit
	12	G3	95.08	28.42	Geku	terrace	alcove; terrace; slackwater deposit
	13	B2	94.96	28.32	Boleng	tributary junction	slackwater deposit
	14	*B1*	*94.95*	*28.33*	*Boleng*	*tributary junction*	*slackwater deposit*
	15	B3	94.96	28.32	Boleng	tributary junction	slackwater deposit
	16	*A1*	*95*	*28.24*	*Boleng*	*tributary junction*	*slackwater deposit*
	17	P2	94.99	28.23	Pangi	tributary junction	slackwater deposit

	18	*P1*		*94.98*	*28.23*	*Pangi*	*tributary junction*	*slackwater deposit*
	19	R2		95.04	28.17	Ranaghat	tributary junction	slackwater deposit
	20	R1		95.03	28.17	Ranaghat	tributary junction	slackwater deposit
	21	*R3*		*95.11*	*28.13*	*Ranaghat*	*tributary junction*	*slackwater deposit*
Panda et al. (2020)	1	S-4	LD-3241	95.298889	28.103889	Ranaghat	above modern channel	slackwater deposit
	2	S-7	LD-3250	94.984528	28.2335	Ranaghat	tributary junction	a 2.5m thick sequence is located on a bedrock bench at an elevation of 78 ± 2m a.r.l. The sequence is made up of brownish-yellow
	3	S-10	LD-3244	95.090833	28.426944	Geku	terrace	paleoflood sediments form an apron on a fluvial terrace reaching an elevation of ~60m and 100m a.r.l. Three sections were studied at varied elevations at Geku. A ~13m thick massive yellowish colored sand (mean grain size 173µm) at a lower elevation had an OSL age of 3 ± 0.5ka
	4	S-9	LD-3245	95.090833	28.426944	Geku	terrace	A 7.3m thick section;
	5	S-11	LD-3246	95.090833	28.426944	Geku	terrace	Two samples from a 7m thick massive sand located at 100 ± 5m a.r.l. and yielded two similar OSL ages: 3 ± 0.7ka and 3 ± 0.4ka.
	6	S-12	LD-3249	95.090833	28.426944	Geku	terrace	
	7	S-14	LD-3251	95.024722	28.628056	Yinkiong	terrace	a 7m thick sequence of mas- sive grayish sand (mean grain size 120µm) located on a fluvial fill terrace at ~27m a.r.l. is studied. The top of the sequence had an age of 1.3 ± 0.7ka

	8	*S-19*	*LD-3248*	*95.892131*	*28.75324*	*Bombdao*	*above modern channel*	*an 11m thick, yellowish colored, massive sand deposit; elevation 290 m a.r.l.; sample taken from 6m below top has OSL age of 4 ± 0.6 ka.*
	9	S-23	LD-3243	94.848611	28.964444	Tuting	terrace	a 6m thick massive sand deposit was located at 151m a.r.l. The sequence showed the development of faint parallel laminations at places; and the whole sequence was comprised of six flood units with mean grain size between 160 and 190µm. The basal unit had an age of 7 ± 1ka (S-23);
	10	S-26	LD-3242	94.848611	28.964444	Tuting	terrace	the uppermost section had an age of 4 ± 1ka; terrace

Table A2. GeoClaw (version 5.5) input parameters for numerical simulation. Note that the model parameters allow for refinement up to 6 levels, however, only 5 levels were output such that the finest resolution of the simulation roughly matches that of the finest topographic input.

Input Parameter	**Value used**
Topographic data	SRTM 3 arc-second (~90 m cells) DEM combined with SRTM 1 arc-second (~30 m cells) from Turzewski et al. (2019)
Number of AMR levels	6
AMR refinement parameters	
Level 1	1 km^3 (1 km x 1 km)
Level 2	62500 m^3 (250 m by 250m), refined by ¼
Level 3	15625 m^3 (125 m by 125 m), refined by ½
Level 4	3906.25 m^3 (62.5 m x 62.5 m), refined by ½
Level 5	976.56 m^3 (31.25 m x 31.25 m), refined by ½
Level 6	244.14 m^3 (15.6 m x 15.6 m), refined by ½
Manning's roughness coefficient (n)	0.04
Dam elevation, height, width	3088 m, 246 m, 1.3 km (Montgomery et al., 2004)
Lake volume	81 km^3 (Montgomery et al., 2004)
Dam failure mechanism	instantaneous

Table A3. Extent of inundation along major tributaries of the Yarlung Siang River. Tuting, Amging, Mossing, and Boleng refer to the towns at the confluence of the tributary with the main stem of the YSR. Locations for tributaries are marked in Figure 1.1.

Tributary	**Max inundation distance upstream (km)**
Po River	13
Tuting	13
Amging	10
Mossing	8
Boleng	11
Siyom River	60

Data Set S1. This data set includes hydraulic variables at every previously identified megaflood deposit from Table 1. It can be found at https://doi.org/10.5281/zenodo.6301292. AuthorYearDeposit#: Depth (blue), speed (yellow), and bed shear stress (green) measurements at each of the previously identified megaflood deposits from Table S1. AuthorYearDeposit#_FP: flood power at each deposit. Pink indicates flood power > 10 kW/m^2 and blue indicates flood power < 5 kW/m^2. Included in a folder called "Sand Limits" within this data set are figures with depth, speed, and bed shear stress with the upper and lower bed shear stress limits required to transport sand grains (0.063-2.0 mm) on the measured local slope.

Data Set S2a,b Can be found at https://doi.org/10.5281/zenodo.6301292. Data Set S2a: every kilometer downstream of the dam (0 km) to the end of the Yarlung Tsangpo Gorge (165 km). Data Set S2b: every kilometer from the end of the Yarlung Tsangpo Gorge (166 km) to Pasighat (507 km). fig_Xkm_ds_SuppInfo: Depth (blue), speed (yellow), and bed shear stress (green) measurements along the centerline of the modern Yarlung Siang River. Measurements are taken once every kilometer downstream of dam. Fig_Xkm_ds_SuppInfo_FP: flood power calculation along the centerline of the modern Yarlung Siang River. Measurements are taken at the same locations a depth, speed, and stress.

Movie S1. Simulated depth in a narrow valley on the Yarlung Siang River during the first 63 hours of the flood. Same location as Figure 1.3A. Reference Figure 1.1c for location.

Movie S2. Simulated speed in a narrow valley on the Yarlung Siang River during the first 63 hours of the flood. Same location as Figure 1.3A. Reference Figure 1.1B for location.

Movie S3. Simulated stress in a narrow valley on the Yarlung Siang River during the first 63 hours of the flood. Same location as Figure 1.3A. Reference Figure 1.1B for location.

Movie S4. Simulated flood power in a narrow valley on the Yarlung Siang River during the first 63 hours of the flood. Same location as Figure 1.3A. Reference Figure 1.1c for location.

Movie S5. Simulated depth in a sharp turn on the Yarlung River during the first 63 hours of the flood. Same location as Figure 1.3B. Reference Figure 1.1c for location.

Movie S6. Simulated speed in a sharp turn on the Yarlung River during the first 63 hours of the flood. Same location as Figure 1.3B. Reference Figure 1.1c for location.

Movie S7. Simulated stress in a sharp turn on the Yarlung River during the first 63 hours of the flood. Same location as Figure 1.3B. Reference Figure 1.1c for location.

Movie S8. Simulated flood power in a sharp turn on the Yarlung River during the first 63 hours of the flood. Same location as Figure 1.3B. Reference Figure 1.1c for location.

Movie S9. Simulated depth in a tight meander on the Yarlung River during the first 63 hours of the flood. Same location as Figure 1.3C. Reference Figure 1.1c for location.

Movie S10. Simulated speed in a tight meander on the Yarlung River during the first 63 hours of the flood. Same location as Figure 1.3C. Reference Figure 1.1c for location.

Movie S11. Simulated stress in a tight meander on the Yarlung River during the first 63 hours of the flood. Same location as Figure 1.3C. Reference Figure 1.1c for location.

Movie S12. Simulated flood power in a tight meander on the Yarlung River during the first 63 hours of the flood. Same location as Figure 1.3C. Reference Figure 1.1c for location.

Movie S13. Simulated depth around an overtopped ridge on the Siang River during the first 63 hours of the flood. Same location as Figure 1.3D. Reference Figure 1.1c for location.

Movie S14. Simulated speed around an overtopped ridge on the Siang River during the first 63 hours of the flood. Same location as Figure 1.3D. Reference Figure 1.1c for location.

Movie S15. Simulated stress around an overtopped ridge on the Siang River during the first 63 hours of the flood. Same location as Figure 1.3D. Reference Figure 1.1c for location.

Movie S16. Simulated flood power around an overtopped ridge on the Siang River during the first 63 hours of the flood. Same location as Figure 1.3D. Reference Figure 1.1c for location.

Movie S17. Simulated flood power along the longitudinal profile of the Yarlung Siang River through time. A) t = 0hr to t = 10hr, B) t = 10hr to t = 20hr, C) t = 20hr to t = 30hr, D) t = 30hr to t = 40hr, E) t = 40hr to t = 50hr, F) t = 50hr to t = 53hr.

Movie S18. Simulated depth along the Siyom River during the first 63 hours of the flood. Same location as Figure 1.6. Reference Figure 1.4 for location.

Movie S19. Simulated speed along the Siyom River during the first 63 hours of the flood. Same location as Figure 1.6. Reference Figure 1.4 for location.

Movie S20. Simulated stress along the Siyom River during the first 63 hours of the flood. Same location as Figure 1.6. Reference Figure 1.4 for location.

Movie S21. Simulated flood power along the Siyom River during the first 63 hours of the flood. Same location as Figure 1.6. Reference Figure 1.4 for location.

Movie S22. Simulated depth around Tuting during the first 63 hours of the flood. Same location as Figure 1.6 Reference Figure 1.1c for location.

Movie S23. Simulated speed around Tuting during the first 63 hours of the flood. Same location as Figure 1.6. Reference Figure 1.1c for location.

Movie S24. Simulated stress around Tuting during the first 63 hours of the flood. Same location as Figure 1.6. Reference Figure 1.1c for location.

Movie S25. Simulated flood power around Tuting during the first 63 hours of the flood. Same location as Figure 1.6. Reference Figure 1.1c for location.

APPENDIX B

Supporting Information for Chapter 2

Sedimentary evidence of Quaternary megaflood backflow deposition along the Siyom River Valley, eastern Himalaya

S. M. Morey[1], K. A. Lang[2], K. W. Huntington[1], C M. Shobe[3,4], S. Nath[2], C. L. Loreen[1]

[1]Department of Earth and Space Sciences, University of Washington, Seattle, WA, USA.
[2]School of Earth and Atmospheric Sciences, Georgia Institute of Technology Main Campus, Atlanta, GA, USA.
[3]Department of Geology and Geography, West Virginia University, Morgantown, WV, USA.
[4]U.S. Forest Service Rocky Mountain Research Station, Fort Collins, CO, USA

Contents of this file

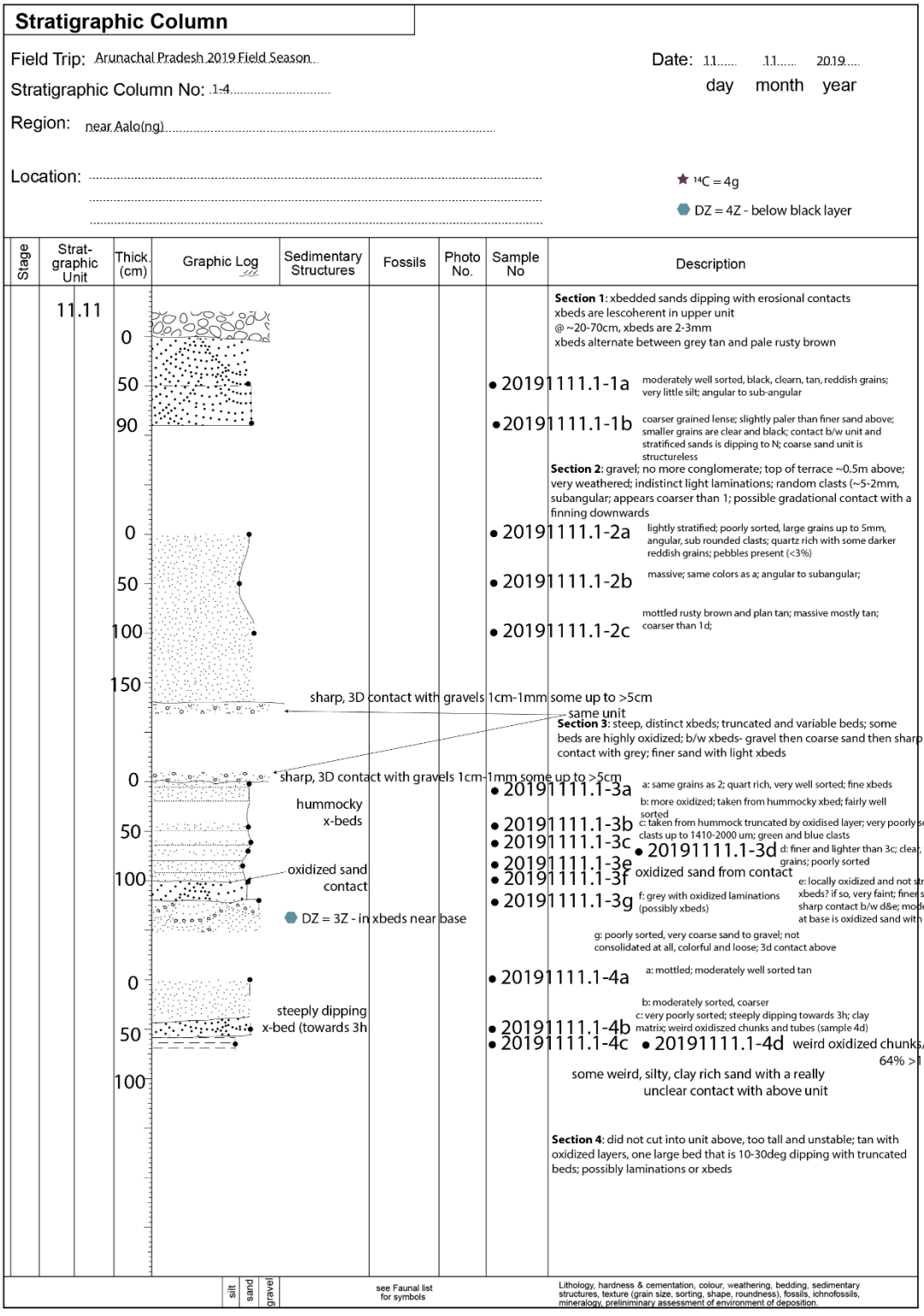
Stratigraphic Column
Field Trip: Arunachal Pradesh 2019 Field Season
Date: 1.1 1.1 2019
day month year
Stratigraphic Column No: 1-4
Region: near Aalo(ng)
Location:
¹⁴C = 4g
DZ = 4Z - below black layer
Stage
Strat-graphic Unit
Thick (cm)
Graphic Log
Sedimentary Structures
Fossils
Photo No.
Sample No
Description
Section 1
Section 2
Section 3
Section 4
11.11
0
50
90
0
50
100
150
0
50
100
0
50
100
sharp, 3D contact with gravels 1cm-1mm some up to >5cm
same unit
sharp, 3D contact with gravels 1cm-1mm some up to >5cm
hummocky x-beds
oxidized sand contact
DZ = 3Z - in xbeds near base
steeply dipping x-bed (towards 3h
Section 1: xbedded sands dipping with erosional contacts
xbeds are lescoherent in upper unit
@ ~20-70cm, xbeds are 2-3mm
xbeds alternate between grey tan and pale rusty brown
• 20191111.1-1a moderately well sorted, black, clearn, tan, reddish grains; very little silt; angular to sub-angular
• 20191111.1-1b coarser grained lense; slightly paler than finer sand above; smaller grains are clear and black; contact b/w unit and stratificed sands is dipping to N; coarse sand unit is structureless
Section 2: gravel; no more conglomerate; top of terrace ~0.5m above; very weathered; indistinct light laminations; random clasts (~5-2mm, subangular; appears coarser than 1; possible gradational contact with a finning downwards
• 20191111.1-2a lightly stratified; poorly sorted, large grains up to 5mm, angular, sub rounded clasts; quartz rich with some darker reddish grains; pebbles present (<3%)
• 20191111.1-2b massive; same colors as a; angular to subangular;
• 20191111.1-2c mottled rusty brown and plan tan; massive mostly tan; coarser than 1d;
Section 3: steep, distinct xbeds; truncated and variable beds; some beds are highly oxidized; b/w xbeds- gravel then coarse sand then sharp contact with grey; finer sand with light xbeds
• 20191111.1-3a a: same grains as 2; quart rich, very well sorted; fine xbeds
• 20191111.1-3b b: more oxidized; taken from hummocky xbed; fairly well sorted
• 20191111.1-3c c: taken from hummock truncated by oxidised layer; very poorly sorted; larger clasts up to 1410-2000 um; green and blue clasts
• 20191111.1-3d d: finer and lighter than 3c; clear, tan, black grains; poorly sorted
• 20191111.1-3e oxidized sand from contact
• 20191111.1-3f e: locally oxidized and not stratified; light xbeds? if so, very faint; finer sand; mottled; sharp contact b/w d&e; moderately sorted; at base is oxidized sand with silt
• 20191111.1-3g f: grey with oxidized laminations (possibly xbeds)
g: poorly sorted, very coarse sand to gravel; not consolidated at all, colorful and loose; 3d contact above
• 20191111.1-4a a: mottled; moderately well sorted tan
b: moderately sorted, coarser
c: very poorly sorted; steeply dipping towards 3h; clay matrix; weird oxidisized chunks and tubes (sample 4d)
• 20191111.1-4b
• 20191111.1-4c
• 20191111.1-4d weird oxidized chunks/tubes
64% >1.4 mm
some weird, silty, clay rich sand with a really unclear contact with above unit
Section 4: did not cut into unit above, too tall and unstable; tan with oxidized layers, one large bed that is 10-30deg dipping with truncated beds; possibly laminations or xbeds
silt
sand
gravel
see Faunal list for symbols
Lithology, hardness & cementation, colour, weathering, bedding, sedimentary structures, texture (grain size, sorting, shape, roundness), fossils, ichnofossils, mineralogy, preliminary assessment of environment of deposition.

Stratigraphic Column

Field Trip: Arunachal Pradesh 2019 Field Season

Date: 11 (day) 11 (month) 2019 (year)

Stratigraphic Column No: 5-7

Region: near Aalo(ng)

Location:

Stage	Strat-graphic Unit	Thick. (cm)	Graphic Log	Sedimentary Structures	Fossils	Photo No.	Sample No	Description
								Section 5
		0	modern soil is above; laminated, with vegetation and rootes, some rounded cobbles				• 20191111.1-5a	a: very fine sand with clay matrix; some black, mostly quartz; laminations visible
		50	★ ^{14}C = 5W DZ = 5Z in sand between upper grey clay layer and lower blue clay layer				• 20191111.1-5b • 20191111.1-5c	b: pale tan/white/gray clay with oxidized rind at top and bottom; plastic, moldable clay; ~10-12cm thick; unit looks laterally continuous c: poorly sorted sand; wet and horrible when sampled; quartz rich, some black grains up to 1.2mm
		100	★ ^{14}C = 4V				• 20191111.1-5d1	d: blue-ish grey clay with hard pan at top; oxidized layer at base is ~30 cm with coarser grains and flack flecs; has minor laminations
		150	hardpan hardpan				• 20191111.1-5d2 • 20191111.1-5e • 20191111.1-5f	there is water ponding at contact b/w 5d and 5e e: poorly sorted tan; sandy silt; cannot tell if e & f are two distinct units or one unit that changes slightly
		200						f: lenses of coarse material throughout; 2nd oxidized hardpan at ~170cm; slightly darker than 5e has faint x-beds
		250				KAL_2113	• 20191111.1-5g • 20191111.1-5h	g: heavily oxidized tan with reddish yellow ;xbeds are larger here and more apparent; alternating finer and coarser layers; h: similar subunit to 5f 8cm thick @widest; appears structureless; darker than
		300						**Section 5**: ~1m thick fine dark brown sand & silt above pale tan/grey clay (planar); hard contact w/oxidized layer ~1cm on each side below clay is ~10cm of sand then there's a thick 1-1.5m blue grey clay unit atop coarser xbedded sands that are laminated
								Section 6
		0	gray clay					
		50	hardpan					**Section 6**: same blue/grey clay and coarse/fine layers as in 5 with hard pan between; visible flame structures in sandy layers alternating between oxidized and tan beds; some beds are distorted; there are clay clasts in sand
		100						
		150						a: similar to 3h and 4c; 45 cm thick; "dirt"
		200				KAL_2240	• 20191111.1-6a • 20191111.1-6b	b: similar to 5e,f; poorly sorted; larger grains, oxidized layers; flecks of black organic material sampled for radiocarbon
		250						**Section 7**: finer massive warm brown sand above gravel layer (~10-15cm) below gravel is coarser sand (grey and rust) with large truncated x-beds; rounded boulders above look in place
		0					• 20191111.1-7a • 20191111.1-7b	a: gravelly, cobbly bouldery layer; some clases ~15cm; sampled finer layer that shares a contact with sands; poorly sorted b: sharp, non-gradational contact b/w a&b; fairly well sorted
		50					• 20191111.1-7c • 20191111.1-7d	c: less red; sharp contact b/w c&d; finer sand with silt; similar to 5a d: range of samples from gravelly layer; massive no structure; gravels and sands interbedded; dipping and cross contact; very poorly sorted gravelly layer with no structure; 66.8% >1.4mm; median grain size <1.4mm = 0.24 mm
		100					• 20191111.1-7e • 20191111.1-7f	e: sharp contact with gravel above; layer above oxidized xbeds; similar to 5e/f; sharp contact with beds below
		150					• 20191111.1-7g	f: discontinuous, thin warm brown band (3-4cm) pinches out laterally; fine sand with clay and some larger grains g: pale gray sand with oxidized layers; cut through by bioturbation; well sorted

Section 5 / Section 6 / Section 7

silt | sand | gravel

see Faunal list for symbols

Lithology, hardness & cementation, colour, weathering, bedding, sedimentary structures, texture (grain size, sorting, shape, roundness), fossils, ichnofossils, mineralogy, preliniminary assessment of environment of deposition.

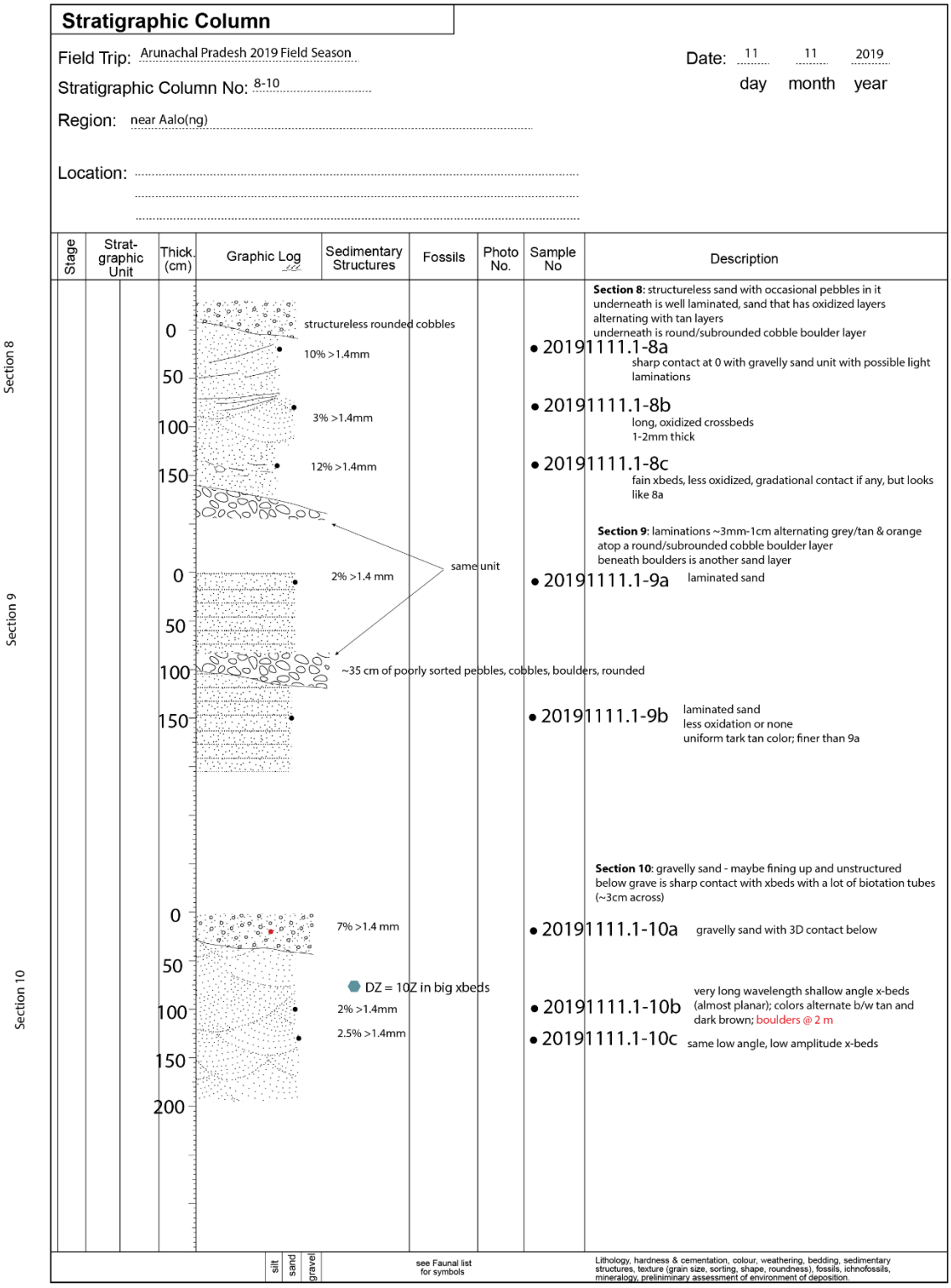

Figure C1. Stratigraphic column from Location 11. These sections have been condensed and simplified in Figure 3.5.

Stratigraphic Column

Field Trip: Arunachal Pradesh 2019 Field Season

Date: 12 (day) 11 (month) 2019 (year)

Stratigraphic Column No: 1-3

Region: near Aalo(ng)

Location:

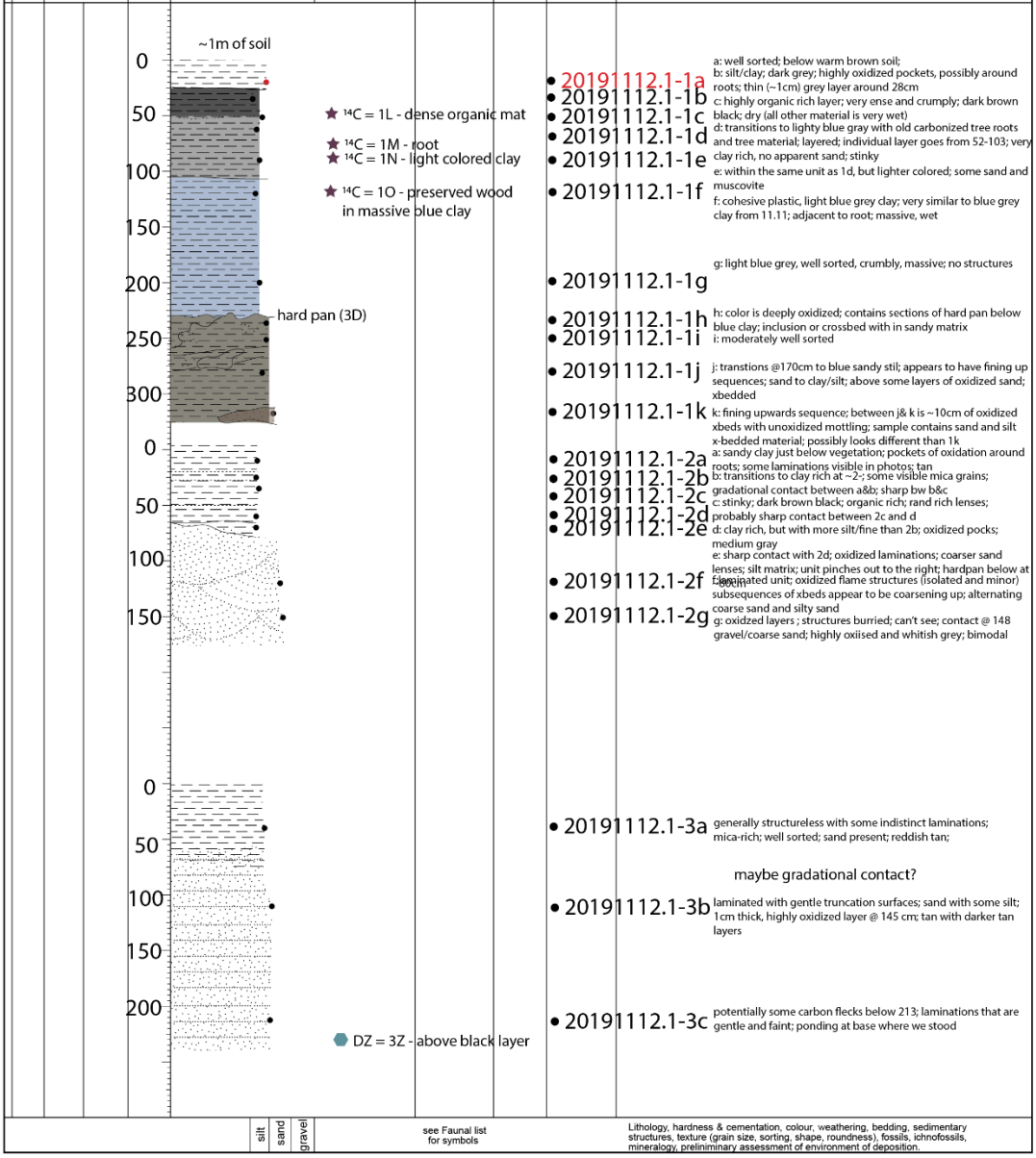

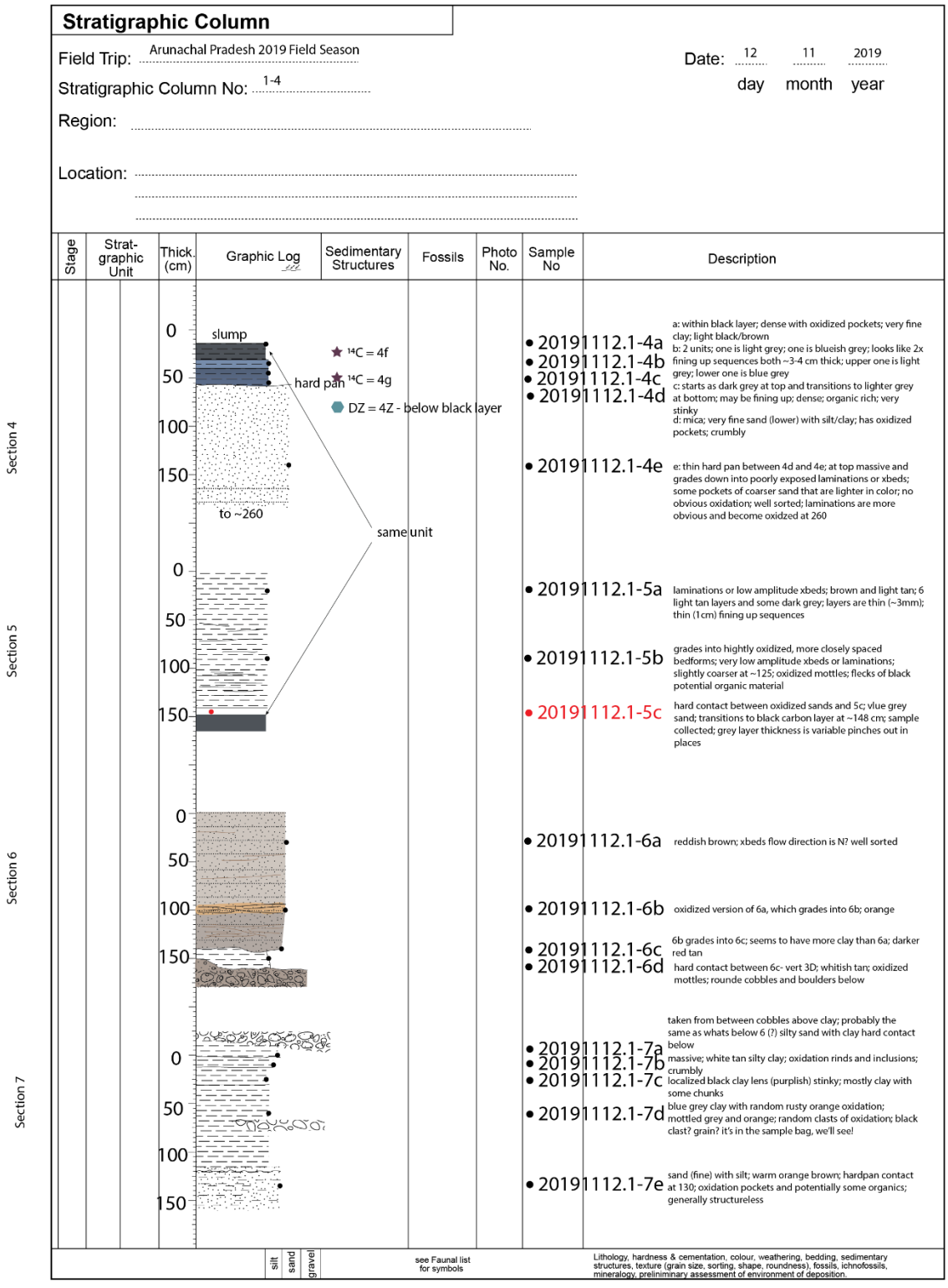

Figure C2. Stratigraphic column from Location 12. These sections have been condensed and simplified in Figure 3.5.

Figure C3. An example of rounded cobbles from T3.

Figure C4: Examples of sedimentary structures visible in Facies A.

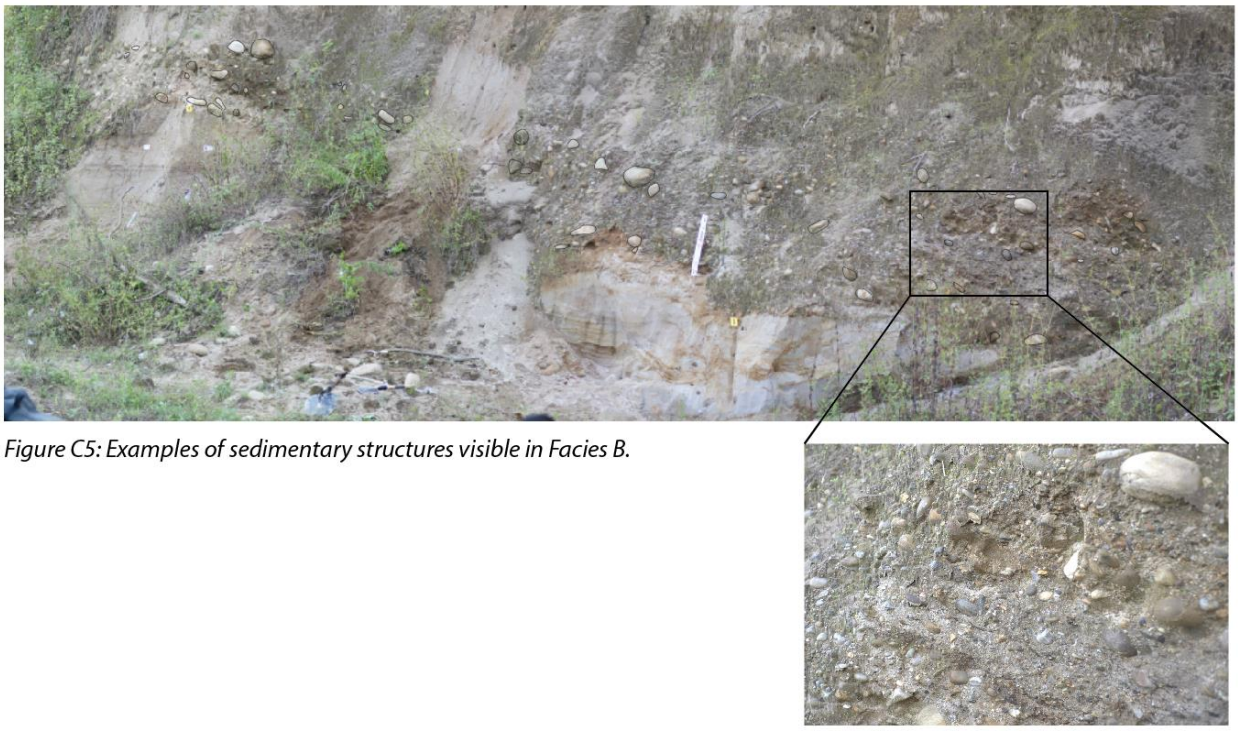

Figure C5: Examples of sedimentary structures visible in Facies B.

Figure C6. Examples of sedimentary structures visible in Facies C.

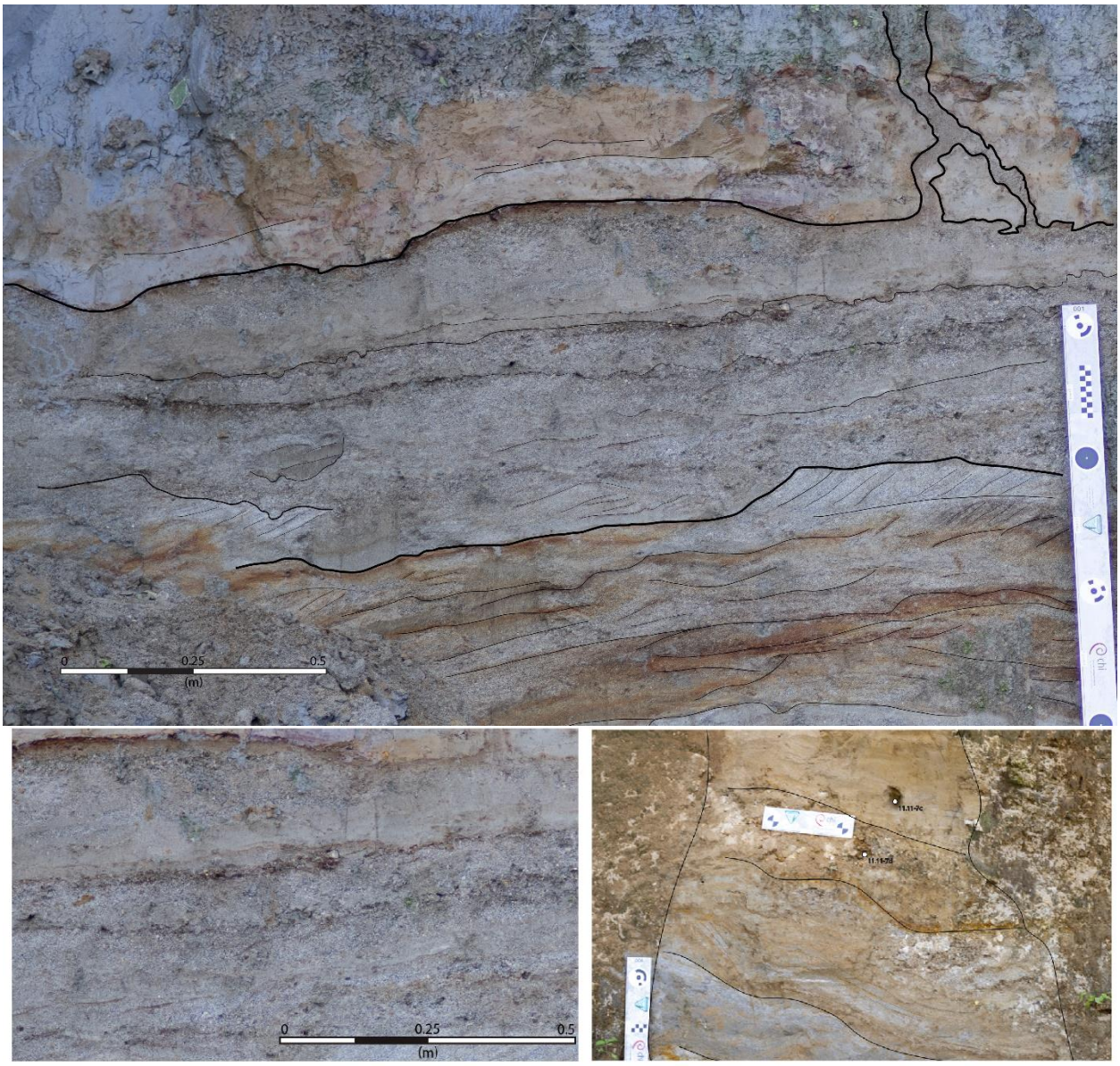

Figure C7: Examples of sedimentary structures visible in Facies D.

Figure C8: Examples of sedimentary structures visible in Facies E.

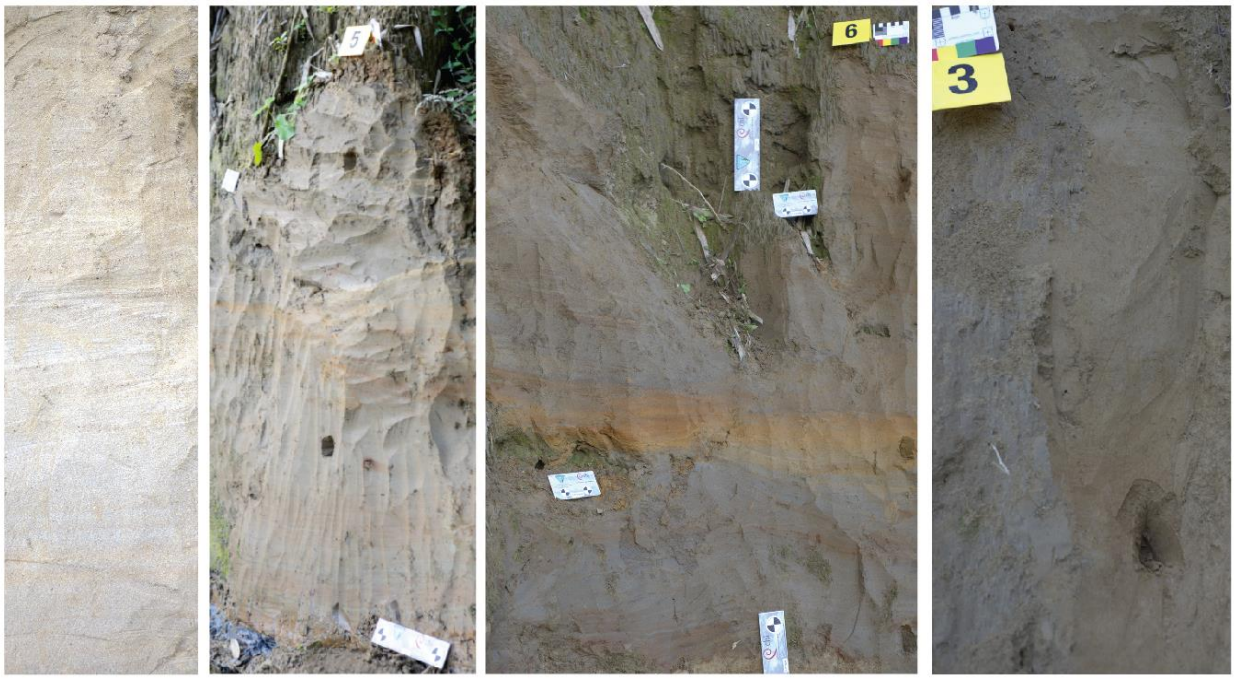

Figure C9: Examples of sedimentary structures visible in Facies F.

Figure C10: Examples of sedimentary structures visible in Facies G.

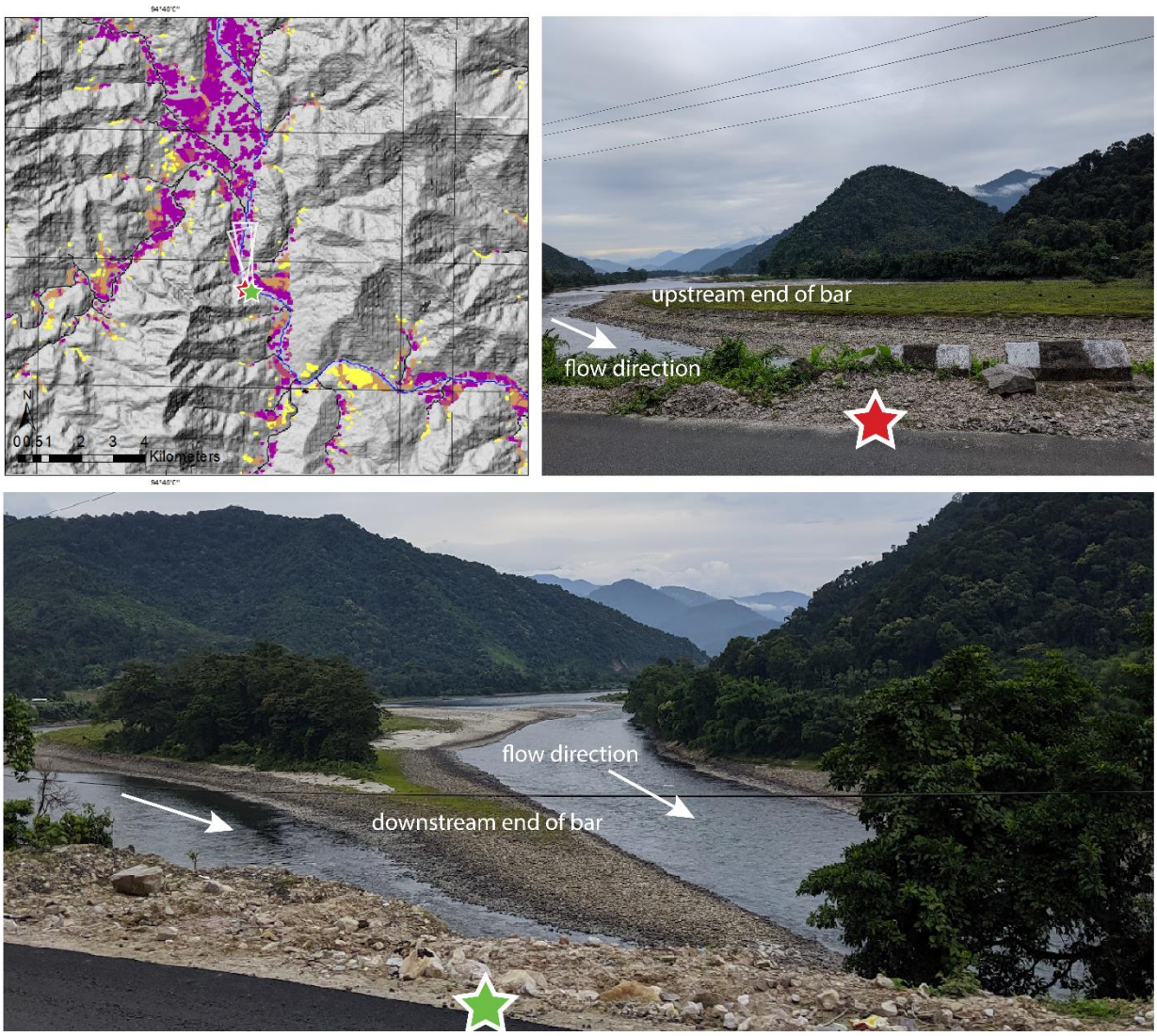

Figure C11. A view of the modern Siyom River.

Table B1. Detrital Zircon U-Th-Pb data for three samples analyzed in Chapter 2, attached in separate CSV.

APPENDIX C

Supporting Information for

The lasting legacy of megaflood boulder deposition in mountain rivers

S. M. Morey[1], C. M. Shobe[2,3], K. W. Huntington[1], K. A. Lang[4], A. G. Johnson[1], and A. R. Duvall[1]

[1]Department of Earth and Space Sciences, University of Washington, Seattle, WA, USA.
[2]Department of Geology and Geography, West Virginia University, Morgantown, WV, USA.
[3]U.S. Forest Service Rocky Mountain Research Station, Fort Collins, CO, USA
[4]School of Earth and Atmospheric Sciences, Georgia Institute of Technology Main Campus, Atlanta, GA, USA.

Corresponding authors: Susannah Morey (smmorey@uw.edu) and Katharine Huntington (kate1@uw.edu)

Contents of this file

Introduction

The Supporting Information below includes (1) detailed notes about how the authors changed the Blocky River and Knickpoint Evolution Model from a 1-D reach model into a full 1-D longitudinal profile model, (2) methods for boulder measurement in Google Earth and (3) methods for calculating uncertainty of boulder measurements between Google Earth and a 3-D Structure from Motion model. The new model (called longBRaKE) can be found at https://doi.org/10.5281/zenodo.8056912. Figures within the Supplemental Information include (C1) a log-log plot of slope and area of the Yarlung-Siang River used to calculate the reference concavity, (C2) visual aids for boulder measurement methods (both (2) and (3)), and (C3) model results of Experimental Run 3, in which boulders are added to the channel stochastically. Additionally, we include two tables: (C1) calibration data between Google Earth measurements

and the SfM model measurements and (C2) all boulder measurements at each bar. The latter is included as a separate CSV.

(1) **Notes on converting BRaKE from a reach to a river (longBRaKE).** The goal is to run BRaKE (Blocky River and Knickpoint Evolution) not simply with a spatially constant, but with a discharge value that scales with drainage area A (and therefore with downstream distance x). This will produce concave-up profiles. Currently BRaKE simply generates a discharge value Q by pulling from a Weibull distribution (Rossi et al., 2016). Instead, we want $Q\ (x) \propto\ A\ (x) \propto\ x$.

(a) Scaling discharge to distance downstream. By Hack's law:

$$A(x) = \left(\frac{x}{C}\right)^{1/h},$$

where x is distance downstream, C is some constant, and h is 0.5-0.6. By setting a value for C that is appropriate to the study landscape, we can know $A(x)$. Similarly, any extra increment of area gained by traveling downstream can be calculated:

$$\Delta A = \left(\frac{\Delta x}{C}\right)^{1/h},$$

where Δx is an increment of distance. By mass conservation, we can assume that $Q\ =\ rA$ where r is some measure of runoff [L/T]. Combing gives:

$$W = rA = r\left(\frac{x}{C}\right)^{1/h},$$

Where the values of r and C set the rate at which discharge increases downstream. Incremental increases in Q with x can also be calculated:

$$\Delta Q = r\Delta A = r\left(\frac{\Delta x}{C}\right)^{1/h}.$$

So we can assert that some discharge Q^* is the discharge at the left-hand side of the model domain (distance x_0; the point of lowest drainage area). We can then solve for $Q(x)$ at any given point:

$$Q(x) =\ Q^* + r\left(\frac{\Delta x}{C}\right)^{1/h},$$

where Δx is the distance between point x_0; and x. Q^* will be drawn using the same procedure as is currently used, and should be scaled approximately to the field landscape.

(b) Converting volumetric discharge to unit discharge through downstream-increasing channel width. The above procedure gives us volumetric water discharge [L^3/T], but we need discharge per unit width [L^2/T] to feed into the rest of the model. We get this by $q\ =\ Q/w$ where w is channel

width, which in the single-reach conceptualization is a constant. But in a long profile width typically goes to $w = k_w A^{0.5}$ (Leopold and Maddock, 1953); Wohl and David, 2008) where k_w is a scaling constant. Again. We can think about this as an incrementing function from the width at the uppermost point w_0:

$$\Delta w = k_w \Delta A^{0.5}.$$

So we need width to scale with drainage area. Starting with the last equation above:

$$Q(x) = Q^* + r\left(\frac{\Delta x}{C}\right)^{1/h},$$

we can then divide by the width at each point to get unit discharge:

$$q(x) = \frac{Q^* + r\left(\frac{\Delta x}{C}\right)^{1/h}}{w_0 + \Delta w}$$

$$q(x) = \frac{Q^* + r\left(\frac{\Delta x}{C}\right)^{1/h}}{w_0 + k_w \Delta A^{0.5}}$$

$$q(x) = \frac{Q^* + r\left(\frac{\Delta x}{C}\right)^{\frac{1}{h}}}{w_0 + k_w \left(\frac{\Delta x}{C}\right)^{\frac{0.5}{h}}}$$

The equation we end up with has some base unit discharge that increments as a function of distance. All this requires is drawing Q^* from a distribution, which BRaKE already does, and then specifying values for r, C, h, w_0, and k_w. h should be 0.5 to 0.6 while the values of the others don't matter so long as discharges and widths approximate what you observe in the field area.

(2) Methods for boulder measurement in Google Earth. We measure boulders using methods for grain size measurement from Bunte and Abt (2001). We began with the boulder bars previously identified by Turzewski et al. (2019) and added additional bars to the inventory based on methods described within Turzewski et al. (2019), for a total of 106 boulder bars. We outlined the spatial extent of each bar and then imported a grid from Plus Codes and used the southwest intersection for each green grid to select a grain to measure (Figure C2a). Using four classifications (bedrock, sand, gravel, and boulders, Figure C2b), we measured at least 100 boulders on each bar, starting at the upstream end and moving downstream in a rough line following the grid pattern.

(3) Methods for calculating uncertainty of boulder measurements. To calibrate error on our remote boulder measurements, we constructed a structure from motion (SfM) model of a boulder bar near Tuting, Arunachal Pradesh using images collected in the field. 25 unique boulders were identified in each data set and measured 10 times in each (Table C1, Figure C2c-e). The error in Google Earth was calculated as the standard deviation of measurements. Distortion in the SfM model was determined by measuring fixed meter sticks from field data. The standard deviation was calculated from adjusting this distortion. We then propagated the uncertainty between these two data sets by using:

$$\frac{y}{x}\sqrt{\left(\frac{dx}{x}\right)^2+\left(\frac{dy}{y}\right)^2}$$

, where x is the SfM measurement, dx is the error from the SfM model, y is the Google Earth measurement, and dy is the error for the Google Earth model. Uncertainty for each measurement can be found in Table B1. On average, uncertainty is 5.5cm or within 0.5-10% of each measured boulder. As grain size increases, error decreases. For boulders that are ≥2m, error is >2% (Figure C2f).

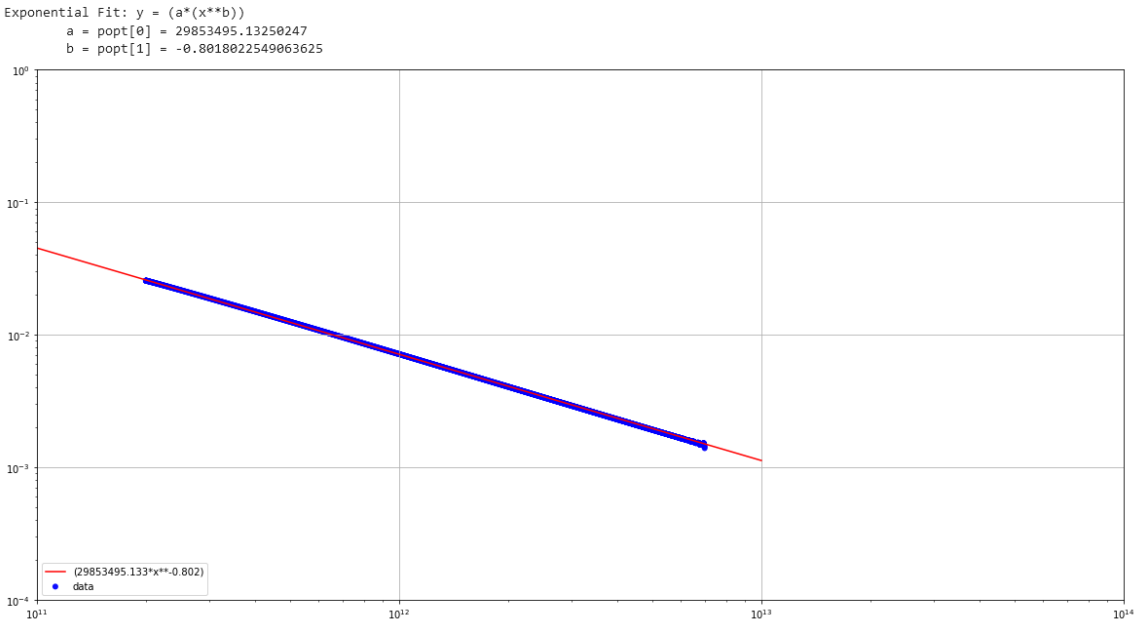

Figure C1. Slope vs. area plot for the initial equilibrium profile used in the model. The slope of this line represents the concavity of the equilibrium profile and is what we use as our reference concavity for calculating channel steepness in our results.

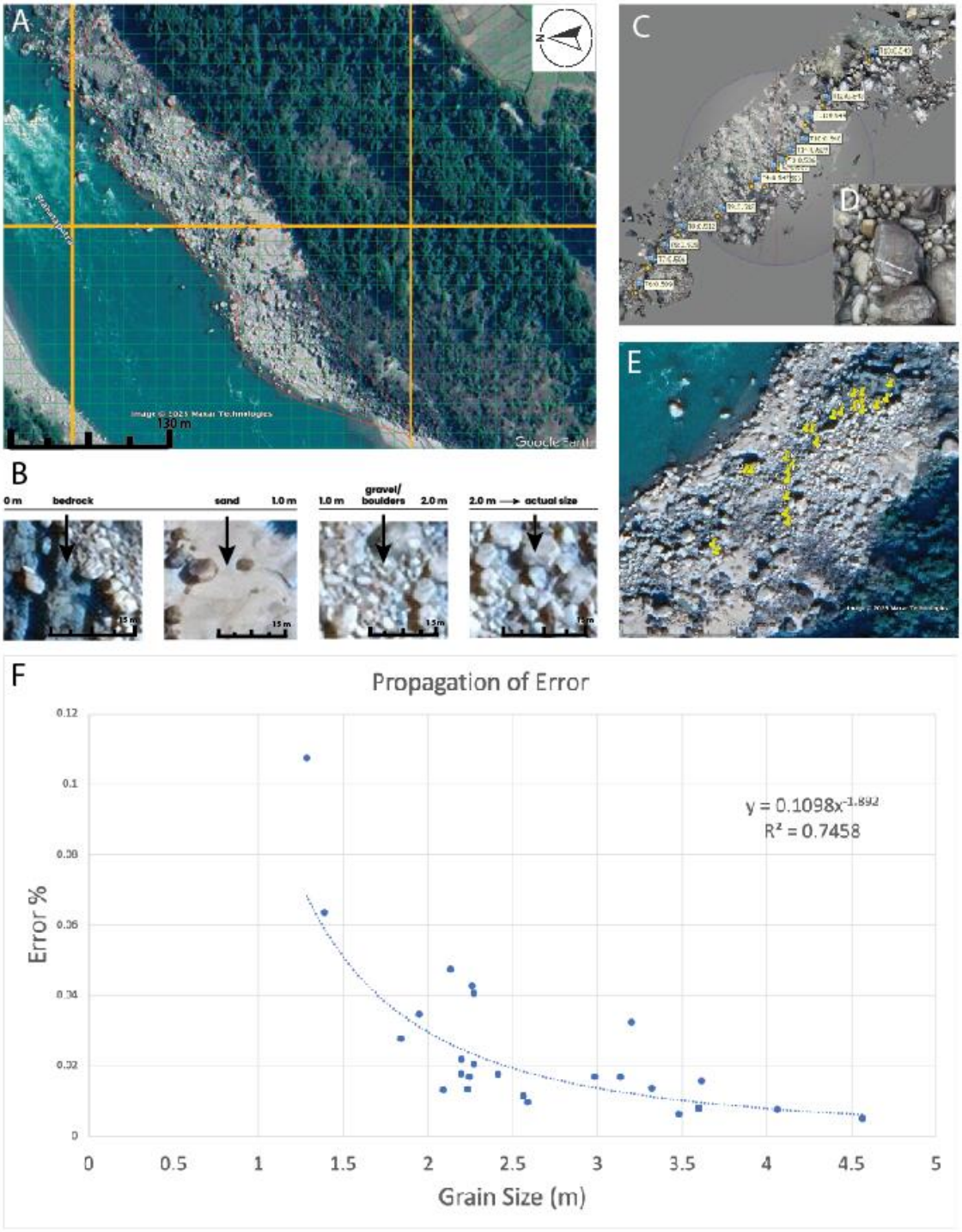

Figure C2. Boulder bar measurement methods a) An example of the grid used to determine measurement locations. This is Bar 77, which is located near Tuting and is shown in Figure 3.1b-f b) measurement classifications, which include bedrock, sand, gravel and small boulders, and all other boulders c & d) Images from the SfM model in (c) boulders measured in Table S1 have labels

e) The same boulders from (c), but measured in Google Earth f) Propagation of uncertainty between SfM model and Google Earth measurements plotted as percent error. Data plotted can be found in Table C1.

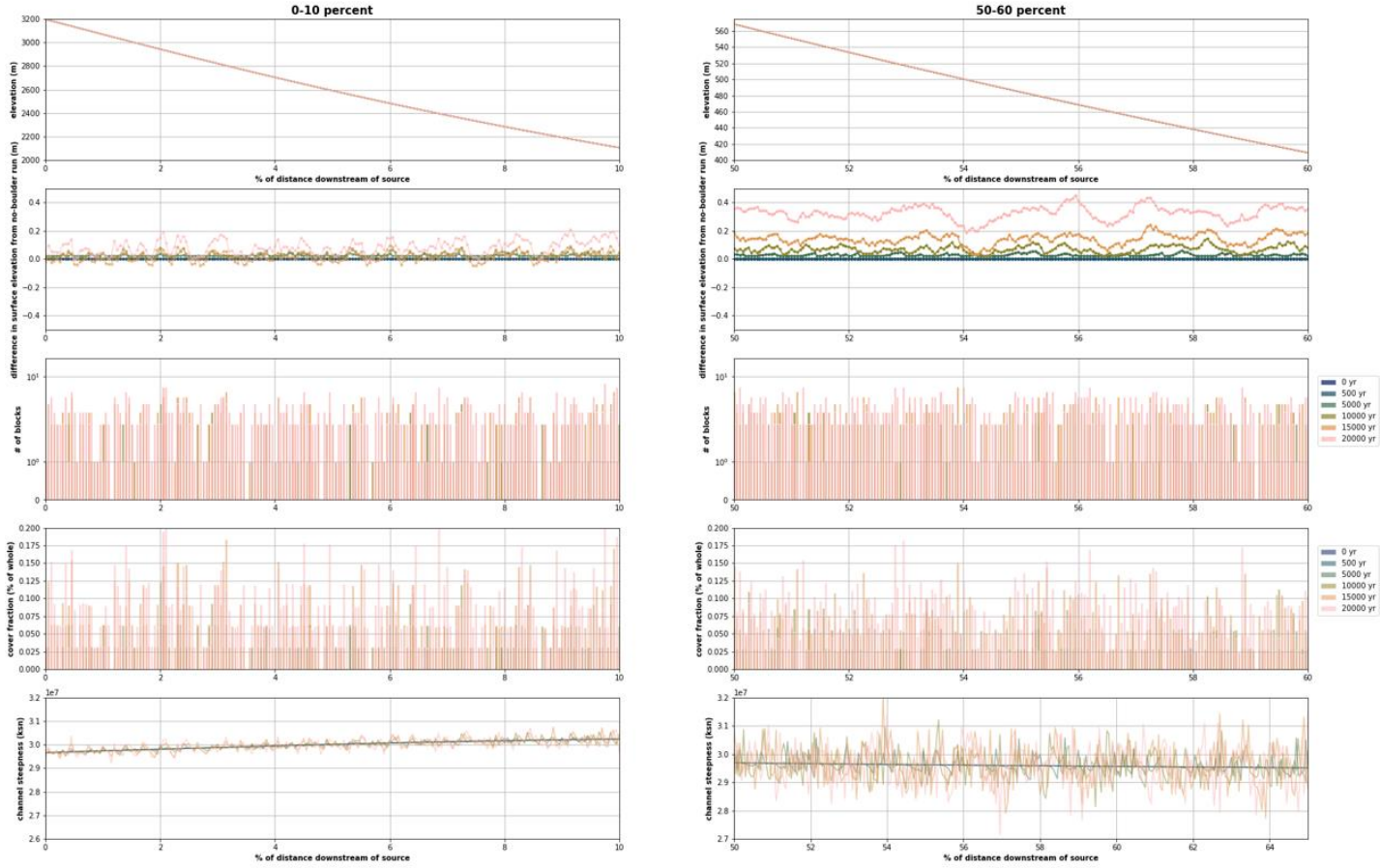

Figure C3. Model results of Experimental Run 2 (R2). This figure shows the same areas as in Figure 2: 0-10% of the long profile and 50-60% of the long profile. All plots show 0 years, 500 years, 5 kyrs, 10 kyrs, 15 kyrs, and 20 kyrs. Row 1 shows the river bed elevation in meters. Row 2 shows the difference in surface elevation in meters. Row 3 shows the number of blocks at each location. Row 4 shows the channel steepness (k_{sn}).

Table C1. Calibration data between Google Earth measurements and the SfM model measurements. Each boulder was measured 10 times in each data set and the average and error is shown for those measurements for each boulder. Detailed methods are described above.

Boulder number	Average Google Earth (m)	Average Ortho (m)	Error Google Earth (m)	Error Ortho (m)	Propagation of Uncertainty (m)
1	3.617	4.059	0.17732895	0.16853316	0.05725024
2	2.134	2.229	0.06292853	0.2258625	0.10103491
3	4.064	4.112	0.07647803	0.10352464	0.03106516
4	2.589	2.607	0.0395671	0.05317187	0.02531034
5	2.271	2.307	0.10418467	0.02532926	0.04643554
6	1.391	1.412	0.11901914	0.03853249	0.08847441
7	3.322	3.335	0.11998148	0.09413006	0.04565908
8	1.285	1.29	0.1249222	0.12729553	0.13798523
9	2.415	2.445	0.02718251	0.10228412	0.04279019
10	2.986	3.013	0.14758802	0.04026608	0.05074268
11	2.564	2.613	0.06719788	0.03810222	0.02942924
12	2.196	2.182	0.07647803	0.03722143	0.03902823
13	2.235	2.246	0.04377975	0.05166717	0.03006605
14	2.271	2.334	0.060452	0.21310848	0.09254006
15	2.245	2.305	0.07153088	0.05252099	0.03815169
16	2.197	2.209	0.1046741	0.01826723	0.04809375
17	1.84	1.881	0.09345231	0.02206068	0.05098965
18	3.481	3.517	0.03871549	0.0688723	0.02229012
19	4.566	4.581	0.09856752	0.04590883	0.02372212
20	3.6	3.656	0.0781736	0.07193937	0.02885513
21	3.137	3.238	0.16885563	0.03046708	0.05293887
22	2.258	2.177	0.10921945	0.17353955	0.09671164
23	1.95	1.972	0.13072448	0.02470529	0.06743792
24	2.092	2.116	0.0454117	0.03710487	0.02758864
25	3.203	3.152	0.06700746	0.31517029	0.10380852
				Overall Propagation of Uncertainty	0.05513598

Table C2. Measurements of boulders at the 106 boulder bars identified in Figure 3.1a. Each column is a different bar. “nan” refers to a measurement that was below 2m (i.e., bedrock, sand, or gravel/small boulders, see Figure C2 for examples).

VITA

EDUCATION

2023 Ph.D., Geology, University of Washington, Department of Earth & Space Sciences
"The lasting legacy of eastern Himalayan megafloods: from erosion to deposition"
Advisor: Dr. Katharine W. Huntington

2016 B.S., Geology, University of Texas at Austin, Jackson School of Geosciences
Cum laude with Honors and Special Honors.
"The Evolution of the Surveyor Fan and Channel System, Gulf of Alaska, based on Core-Log-Seismic Integration at IODP Site U1417"
Advisor: Dr. Sean Gulick

2016 B.A., Plan II Honors, University of Texas at Austin, College of Liberal Arts
selective multidisciplinary honors program with a focus on problem solving, critical thinking, and technical writing

PUBLICATIONS

* denotes undergraduate or high school advisee

Published

1. **Morey SM**, Huntington KW, Turzewski MD, Mangipudi M*, Montgomery DR (2022). *The erosional and depositional potential of Holocene Tibetan megafloods through the Yarlung Tsangpo Gorge, eastern Himalaya: Insights from 2D hydraulic simulations.* Journal of Geophysical Research: Earth Surface, 127, e2021JF006498. 10.1029/2021JF006498
2. Pfeiffer, A. M., **Morey, S**., Karlsson, H. M., Fordham, E. M., & Montgomery, D. R (2022). *Survival of the strong and dense: Field evidence for rapid, transport-dependent bed material abrasion of heterogeneous source lithology*. Journal of Geophysical Research: Earth Surface, 127, e2021JF006455. 10.1029/2021JF006455
3. Hoffman A, Holschuh N, Mueller M, Paden J, Muto A, Ariho G, Brigham C, Christian J, Davidge L, Heitmann E, Hills B, Horlings A, **Morey S**, O'Connor G, Fudge T, Steig E, Christianson K. *(2023). Scars of tectonism promote ice-sheet nucleation from Hercules Dome into West Antarctica.* Nature Geoscience.

In Review or Revision

4. **Morey SM**, Shobe CM, Huntington KW, Lang KA, Johnson AG*, Duvall AR. *The lasting legacy of megaflood boulder deposition in mountain rivers*. Geophysical Research Letters. Submitted Jun 2023.
5. Huntington KW, McQuarrie N, Hodges KV, Ghoshal S, **Morey SM**. *Thermochronologic constraints on the exhumation history of collisional orogens: Evaluating kinematic models of Miocene-Recent central Himalayan deformation.* Earth and Planetary Science Letters.

In Prep

6. **Morey SM**, Lang KA, Huntington KW, Shobe CM, Nath S, Loreen C. *Sedimentary evidence of Quaternary megaflood deposition in the Siyom River valley, eastern Himalaya.* In prep for submission to Geological Society of America Bulletin.

7. **Morey SM**, Gulick SPS, Walton ML, Swartz JM, Reece RS, Jaeger JM. *Pleistocene Climate Change in Southern Alaska Influencing Evolution of the Surveyor Fan and Channel System.* In prep for submission to Marine Geology.

GRADUATE SCHOOL HONORS & AWARDS

▲ awarded based on submitted research proposal, provided full quarter of research support
† cash award
◊ awarded based on academic merit, provided partial support for semester of undergraduate research

2023 **Julian D. Barksdale Distinguished Service Award**†, UW
awarded for exceptional contributions in support of the Department's mission
J. Dungan Smith Endowed Graduate Fellowship†, UW

2022 Dorothy Stephens Fellowship▲, UW
Inquisitive Graduate Student Support Fund†, UW
UW ESS Research Gala†, *Award for Best Geomorphology Talk*

2021 **Howard A. Coombs Endowed Fellowship for Excellence in Teaching▲**, UW
highest award for teaching as a graduate student
UW ESS Research Gala†, *Award for Best Geomorphology Talk*

2020 Jody Bourgeois Endowed Fellowship in Sedimentary Geology▲, UW

2019 Quaternary Research Center Grant Award†, UW
Kenneth C. Robins Graduate Fellowship▲, UW
Inquisitive Graduate Student Support Fund†, UW
NSF 2019 Graduate Research Fellowship Program*, Honorable Mention*

2018 UW ESS Research Gala†, *Award for Best Poster Figure*
UW ESS Research Gala†, *Award for Best Poster Pitch*

2017 **UW Program on Climate Change Fellowship▲, *Recipient***

TEACHING EXPERIENCE

Curriculum Development

2022 *ESS 311: Geomechanics*, development of online lab curriculum,
with J. DeGrande (2021) and P. Morgan (2022)

2020, 2021 *ESS 426: Fluvial Geomorphology*, development of online curriculum,
with B. Collins

2020 *ESS 400: Field Geology*, development of fluvial geomorphology module for online field course

Teaching

2020-2022 Teaching Assistant *in ESS 311: Geomechanics*
taught by D. Schmidt (2020, 2022), G. Bergantz (2021)

2020, 2021 Teaching Assistant in *ESS 426: Fluvial Geomorphology*
taught by B. Collins

2019, 2020 Teaching Assistant in *ESS 400: Field Geology*
taught by M. McGroder, A. Duvall, C. Condit

2018, 2019 Teaching Assistant in *ESS 101: Introduction To Geology And Societal Impacts*
taught by T. Swanson, UW

SERVICE LEADERSHIP, MENTORING, & OUTREACH

Service Leadership

2022-2023	**Earth Surface Process Faculty Search Committee**, Graduate Representative, ESS, UW
2021-2022	**Graduate Student Representative to the Faculty**, ESS, UW
2022	Brown Bag Seminar Planning Committee, ESS, UW
2020-2021	Curriculum Committee, Graduate Representative, ESS, UW
2020	ESS Graduate Student Justice, Equity, Diversity, & Inclusion (JEDI) Reading Group, Co-founder, UW
2019, 2020	Planning Committee Member, ESS Research Gala, UW
2018-2019	Curriculum Chair, UW ESS Outreach Program (Rockin' Out), WA
2017-2018	Graduate Climate Conference Planning Committee, Pack Forest, WA
2018, 2019	Planning Committee Member, ESS Open House, UW

Mentoring

* denotes co-author on publication

2022-2023	G. Johnson*, UW undergraduate
2022	S. Pol, UW undergraduate
2022	C. Loreen*, UW undergraduate
2020-2021	M. Mangipudi*, high school student, now at Stanford University *STEM Futures Fellow Research Program*
2019	M. Van Arnam, UW undergraduate,
2018-2019	M. Podhaisky, UW undergraduate,

Outreach

2020-2023	Leader: Discovery Park Geology Walks, Seattle, WA
2017-2020	Developer & Leader: Dam Break Response, Using the Augmented Reality Sandbox to understand flooding